Università degli Studi di Ferrara

DOCTORAL COURSE IN ENGINEERING SCIENCE

CYCLE XXXIV

COORDINATOR Prof. Stefano Trillo

An open-source framework for the numerical analysis of constant and variable thickness scroll compressors

Scientific/Disciplinary Sector (SDS) ING-IND/08

Candidate
Ettore Fadiga

Supervisor
Prof. Michele Pinelli

Year 2018/2021

Abstract

Numerical analyses are one of the most important tools to evaluate the performance of scroll compressors and expanders. *Zero-Dimensional (0-D)* models are an important solution to obtain fast and reliable information on the general performance of these machines, while *Computational Fluid Dynamics (CFD)* simulations give more accurate data on the transient behaviour of the compressors, especially during the suction and discharge process. Unfortunately, the availability of open-source tools for low-order and *CFD* simulations of positive displacement machines is still limited.

In this thesis, the author has performed both *0-D* and *CFD* analyses of scroll machines. The numerical tool selected for low-order simulations is a recently published open-source tool for the quasi-static analysis of positive displacement machines, PDSim. On the other hand, the well known *Open source Field Operation And Manipulation (OpenFOAM)* software has been adopted for *Three-Dimensional (3-D)* numerical analyses. Contributing to the expansion of the open-source modelling capabilities of scrolls, two sets of libraries for *OpenFOAM* have been developed. The first, CoolFOAM, is a wrapper that couples *OpenFOAM* with the thermophysical library CoolProp. The second, scrollFOAM, extends the software capabilities allowing to perform full *3-D* simulations of scrolls.

All the numerical tools employed in this thesis have been validated against experimental references and test cases retrieved in the literature. In particular, the results of PDSim and *OpenFOAM* simulations have been compared to each other and to a set of measurements taken from an industrial scroll compressor. The libraries have been employed for different analyses, including the investigation of real gas effects on *CFD* simulations of a scroll expander and a multi-component numerical investigation of a portion of an *Organic Rankine Cycle (ORC)*. From the compressor point of view, the behaviour in off-design conditions and a sensitivity analysis of gap widths have been objects of additional studies.

Lastly, both scrollFOAM and PDSim have been adapted to support a new geometrical formulation for variable thickness scroll geometries. The adoption of variable thickness wraps is theoretically associated with several advantages, including costs reduction and increased efficiencies.

Finally, PDSim and *OpenFOAM* have been coupled to form an open-source tool-chain for the design and optimization of constant and variable thickness scrolls. This tool-chain has been tested by performing a kriging optimization process of a variable thickness compressor working in under-compression. Starting from a constant thickness reference, the optimized geometry reached comparable performance with a consistent reduction of the manufacturing costs.

Keywords: Scroll, Compressor, Expander, CFD, OpenFOAM, Variable thickness, Optimization, Kriging, ORC, Refrigeration

Italian Abstract

Le simulazioni numeriche rappresentano uno degli strumenti più rilevanti per la valutazione delle performance di compressori ed espansori di tipo scroll. I modelli monodimensionali sono una soluzione importante per ottenere informazioni veloci ed affidabili sul funzionamento generale di queste macchine, mentre le analisi CFD forniscono dati più accurati sul loro comportamento transitorio, in particolare durante i processi di aspirazione e scarica. Sfortunatamente, la disponibilità di strumenti open-source per condurre analisi di basso ordine su macchine volumetriche è ancora limitata.

In questa tesi, l'autore ha realizzato sia analisi monodimensionali che simulazioni di fluidodinamica computazionale su macchine di tipo scroll. Il software scelto per le simulazioni a basso ordine è PDSim, un codice open-source rilasciato di recente e utilizzato per le analisi quasistatiche di macchine volumetriche. In alternativa, il ben noto software OpenFOAM è stato adottato per realizzare analisi tridimensionali. Contribuendo all'espansione delle possibilità di modellazione open-source di macchine scroll, sono stati realizzate due serie di librerie software per OpenFOAM. La prima, CoolFOAM, è un wrapper che connette OpenFOAM con la libreria termofisica CoolProp. La seconda, scrollFOAM, estende le possibilità del software permettendo di realizzare simulazioni di scroll totalmente tridimensionali.

Tutti gli strumenti numerici utilizzati in questa tesi sono stati validati utilizzando dati sperimentali e modelli recuperati in letteratura. In particolare, i risultati di PDSim e OpenFOAM sono stati confrontati tra di loro e con una serie di misurazioni effettuate su un compressore scroll di origine industriale. Le librerie sviluppate sono state impiegate nell'ambito di diverse analisi, tra cui uno studio degli effetti di gas reale sulle simulazioni CFD di un espansore scroll e un'analisi multi-componente di una porzione di un ciclo ORC. Dal punto di vista del compressore, è stato studiato il comportamento della macchina in condizioni fuori progetto. In aggiunta, è stata effettuata un'analisi di sensibilità sull'effetto dei trafilamenti all'interno della macchina.

In seguito, sia scrollFOAM che PDSim sono stati adattati per supportare una nuova formulazione geometrica per geometrie scroll a spessore variable. L'adozione di spirali a spessore variabile è teoricamente associata con diversi vantaggi, tra cui una riduzione dei costi e un aumento dei rendimenti.

Infine, PDSim e OpenFOAM sono stati accoppiati per formare una catena open-source per la progettazione e ottimizzazione di scroll a spessore costante e variabile. Questa catena è stata testata realizzando un'ottimizzazione di tipo kriging centrata su un compressore a spessore variabile operante in condizioni di under-compression. Partendo da un riferimento iniziale a spessore costante, la geometria ottimizzata ha dimostrato di raggiungere prestazioni comparabili associate a una consistente riduzione dei costi di produzione.

Contents

List of Figures

List of Tables

Nomenclature

Greek Symbols

α	Angle of the normal direction of a scroll point
$\boldsymbol{\rho}$	Curvature radius
δ	Reduced density
Γ	Diffusivity
$\hat{\mu}$	*Maximum Likelihood Estimation (MLE)* of the mean
$\hat{\theta}$	Kriging: *MLE* of the hyper-parameter θ
μ	Dynamic viscosity
ν	Molar volume
Ω	Acentric factor
ω	Revolution speed
Φ	Angle of the direction tangent to the scroll curve
Φ_0	Involute initial angle
Φ_A	Variable thickness starting angle
Φ_e	Involute ending angle
Φ_s	Involute starting angle
Φ_{Ai}	Variable thickness starting angle of the i-*th* increment region
Φ_{i0}	Inner involute initial angle
Φ_{is}	Inner involute starting angle
Φ_{o0}	Outer involute initial angle
Φ_{os}	Outer involute starting angle
Ψ	Kriging basis functions
ρ	Density
ρ_0	Curvature radius arbitrary constant

τ Reciprocal reduced temperature

θ Orbting angle

ζ General tensorial property

Letters

$\dot{m}$ Mass flow rate

$\dot{Q}$ Exchanged heat

$\dot{W}$ Boundary work

$\hat{p}$ Kriging: *MLE* of the hyper-parameter p

$\hat{s}^2$ Kriging error

$\mathbf{n}$ Outward pointing unit normal vector

$\mathbf{o}$ Vector describing the orbiting motion

$\mathbf{P}$ Position vector

$\mathbf{u_S}$ Velocity of the boundary surface.

$\mathbf{u}$ Fluid velocity

$\mathbf{x_0^{II}}$ VT integration term - increment #2

$\mathbf{x_0^{I}}$ VT integration term - increment #1

$\mathbf{x_0^{r_b}}$ VT integration term - basic radius

$\mathbf{x_0}$ Position vector of a point on the reference spiral (VT)

$\mathbf{x_i}$ Position vector of a point on the inner side of the orbiting spiral (VT)

$\mathbf{x_o}$ Position vector of a point on the outer side of the orbiting spiral (VT)

$\mathbf{y_i}$ Position vector of a point on the inner side of the fixed spiral (VT)

$\mathbf{y_o}$ Position vector of a point on the outer side of the fixed spiral (VT)

C_p Specific heat at constant pressure

c_v Specific heat capacity at constant volume

$cx, 1$ Compression chamber #x (1 is the outermost chamber), flow path number 1

$cx, 2$ Compression chamber #x (2 is the outermost chamber), flow path number 2

$d1$ Side discharge chamber, flow path number 1

$d2$ Side discharge chamber, flow path number 2

dd Central discharge chamber, no pressure equilibrium

ddd	Central discharge chamber, pressure equilibrium
h	Variable thickness increment
h_i	i-th variable thickness increment
k	Thermal conductivity
m	Mass
p	Pressure
P_C	Critical pressure
q_ζ	Volume source of a general tensorial property
R	Mass specific gas constant
r_b	Involute basic radius
R_g	Generating radius
r_o	Orbit radius
R_s	Swing radius
S	Surface bounding a control volume
$s1$	Suction chamber, flow path number 1
$s2$	Suction chamber, flow path number 2
s_p	Scroll pitch
sa	Region between the shell and the wraps
T	Temperature
t	Time
t	Wrap thickness
T_C	Critical temperature
U	Internal energy
V	Volume
w	Width (or height) of the scroll wraps
Z	Compressibility factor

Acronyms

0-D Zero-Dimensional

3-D Three-Dimensional

A/C Air/Conditioning

ACMI Arbitrarily Coupled Mesh Interface

ACMIs Arbitrarily Coupled Mesh Interfaces

ARI Air-Conditioning and Refrigeration Institute

BiCGSTAB BiConjugate Gradient Stabilized

CFD Computational Fluid Dynamics

CFL Courant-Friedrichs-Lewy

COP Coefficient Of Performance

COPs Coefficients Of Performance

DOE Design of Experiments

ECS Extended Corresponding States

EI Expected Improvement

EOS Equations Of State

FSI Fluid Structure Interaction

GA Genetic Algorithm

HEOS Helmoltz Equation Of State

I/O Input/Output

IDVs Intermediate Discharge Valves

LES Large Eddy Simulation

LHS Latin Hypercube Sampling

MFR Mass Flow Rate

MLE Maximum Likelihood Estimation

OpenFOAM Open source Field Operation And Manipulation

ORC Organic Rankine Cycle

ORCs Organic Rankine Cycles

PDMs Positive Displacement Machines

PR Pressure Ratio

PSO Particle Swarm Optimization

RSM Response Surface Method

RSMs Response Surface Methods

SCL Space Conservation Law

STL STereo Lithography interface format

TROVA Test Rig for Organic VApors

TTSE Tabular Taylor Series Extrapolation

VFM Volumetric Flow Matching Ratio

VLE Vapor-Liquid Equilibrium

VT Variable Thickness

WHR Waste Heat Recovery

Chapter 1

Introduction

1.1 Background

Among *Positive Displacement Machines (PDMs)*, the scroll compressor is a device largely employed in refrigeration systems and air conditioners since the 1980s. These machines have become one of the most commonly adopted compressors in such sectors, especially because of their compactness, smooth operation and low level of noise and vibrations. Furthermore, scroll compressors have fewer moving parts with respect to other *PDMs*.

Scroll compressors are constituted by two identical wraps with a spiral shape: the fixed scroll is bonded to the compressor shell, while the moving scroll follows an orbiting path. The two spirals are always in contact with one another, creating pockets that reduce their volumes going from the outermost part of the machine toward the centre, where the shaft is located. The refrigerant fluid, trapped in the outermost chamber of the compressor, is moved through increasingly smaller pockets, reaching the discharge area in the middle. Consequently, the fluid is compressed reaching the resulting temperature and pressure before leaving the machine.

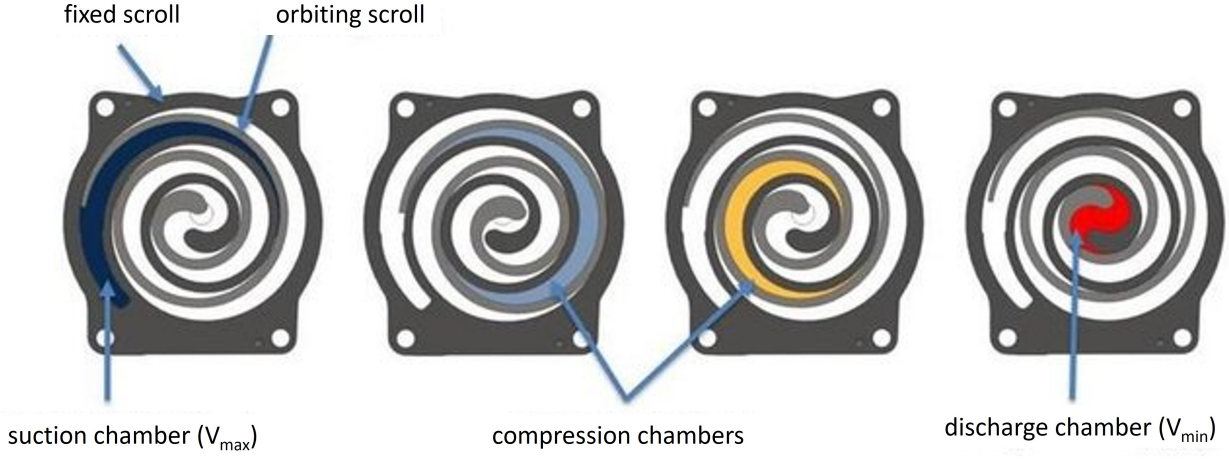

Figure 1.1: Scheme of the working principle of a scroll compressor. [164]

In the last decade, scroll compressors and other *PDMs* (e.g., piston, screw, and vane machines) have been operated as expanders in *Organic Rankine Cycles (ORCs)* to generate power from waste heat and renewable energies [96]. Compared to its alternatives, the scroll expander is generally characterized by higher efficiency and by lower flow rates and rotational speeds [53]. For this reason, this kind of expander is commonly employed in micro-*ORCs* with power outputs up to 2 kW. On the other hand, one of the major drawbacks of this technology is the maximum working temperature (maximum temperature of 250 °C reported by Seher et al. [142]): higher temperatures would increase excessively the thermal expansion of scroll spirals, leading to significant increments of internal leakages [102].

The impact of the refrigeration and air-conditioning fields on global warming and climate change, as well as the importance of recovering waste energy and exploiting renewable energy, are well-known topics in the energy universe. For this reason, any contribution to the improvement of the performance of fundamental components like scroll machines is a valuable contribution to both academic and industrial development. The most common strategies to analyze scroll compressors are experimental campaigns [15, 16, 130, 134], aided by theoretical studies [13, 72, 131, 144, 172], semi-empirical modelling [46, 163] and thermodynamic analyses [123, 160].

In this thesis, a *0-D* model has been utilized by the author to run low-order simulations of scroll geometries and evaluate their performance. This model is based on a quasi-steady simulation tool for the performance evaluation of *PDMs*, named PDSim and published by Bell, Ziviani et al. [21, 185]. Since the majority of the works presented in the literature are semi-empirical models, it has to be underlined that PDSim is not a semi-empirical model, but it is based on the resolution of conservation equations in the domain created discretizing the scroll geometry. As mentioned by Bell et al. [21], one of the reasons for the lack of articles focused on this kind of models in the literature is that "*they are highly specific, generally having been developed for a particular type of machine (scroll, reciprocating, etc.) and are typically structured in a way that makes the simulations very difficult to modify. Also, many of the simulation codes that have been developed are highly proprietary, which means that there is a large amount of simulation code development that is duplicative amongst industrial entities and academic researchers.*". For this reason, in the author's opinion, the recent publication of an open-source tool like PDSim represents an important milestone in the field of scroll machines numerical models. The availability of the source code of an object-oriented software like PDSim encourages the researchers to develop new features, including their code in the main project to increase the overall modelling capabilities.

1.2 Motivation

Low order models are very useful tools to obtain fast and accurate indications to evaluate the overall performance of compressors and expanders. However, a different tool like *CFD* can be employed to evaluate the three-dimensional behaviour of the machines, solving the Navier-Stokes equations in the *3-D* computational domain originated from the scroll complex geometry. The level of accuracy of *CFD* software is inherently superior to the low order models: *CFD* results can be exploited to validate and fine-tune the physical sub-models included in software like PDSim. Currently, the field of *CFD* analyses of scroll machines is almost completely related to industrial research and commercial software. A limited number of software, such as SimericsMP+ [146] and TwinMesh [37], offer a mesh generation service. The resulting mesh is transferred and used in commercial *CFD* codes to solve the flow field. This approach has been adopted by several academic and industrial researchers [36, 67, 75, 127, 128], but the development of new features and tools is delegated to the software developers because no source code is publicly available.

For these reasons, a relevant portion of this thesis has been dedicated to the development of a set of libraries for the open-source *CFD* software *OpenFOAM* [174]. The developed tools have been validated against experimental measurements collected by Picavet et al. [130] of Danfoss Compressors. These *OpenFOAM* custom libraries, grouped under the name scrollFOAM, allow to generate structured meshes of the scroll domain and to move them dynamically to accommodate the machine dynamics during the simulation. Several applications of these tools are presented, including simulations of both compressors and expanders. Hopefully, scrollFOAM will represent a useful contribution to the world of open-source *CFD* software, allowing researchers and industries to have access to free, shareable and extendable tools for the numerical simulation of scroll machines.

Moreover, a section of the manuscript contains the presentation of the implementation of an additional *OpenFOAM* library, CoolFOAM, which is a wrapper between *OpenFOAM* and the thermophysical properties library CoolProp [19]. CoolFOAM has been validated for compressible and incompressible flows and applied to determine the thermophysical properties during the *CFD* analysis of a scroll expander.

Lastly, an important concept presented in this thesis is the construction of an open-source tool-chain for the design and optimization of scrolls. The author has extended the PDSim capabilities to include a new geometrical section for variable thickness scroll geometries, which have the theoretical advantages of reducing costs and, in some cases, leakage losses. Similarly, scrollFOAM has been designed to include the possibility of generating meshes of variable and constant thickness scrolls, starting from the design parameters. These two tools allow performing numerical analyses of scroll geometries starting from the design variables, obtaining results with different levels of accuracy and computational efforts. The flexibility of

this open-source tool-chain has been assessed by performing a kriging optimization procedure to determine the advantages of variable thickness geometries in terms of cost reduction.

Following the considerations included in the current section, the expected contributions of this doctoral thesis can be synthesized as follows:

- Develop a set of *OpenFOAM* libraries to simulate scroll machines in an open-source environment, validating the code against experimental findings.
- Compare the performance of *0-D* and *3-D* modelling to evaluate the fluid dynamics and thermodynamics behaviour of scroll compressors.
- Enhance the thermophysical properties capabilities of *OpenFOAM* by creating a C++ wrapper with the open-source library CoolProp.
- Present a series of practical applications to analyze off-design operations, different working fluids and three dimensional flow features in scroll compressors and expanders.
- Include modelling options for variable thickness scroll geometries in both *OpenFOAM* and PDSim.
- Connect all the tools developed to create an open-source toolchain for the design and optimization of scroll machines.

1.3 Outline

Chapter 2 contains a literature review that starts from a first section focused on general features of scroll compressors, including a historical overview and a collection of geometrical, experimental and modelling studies. Three more specific sections are focused on scroll expanders, *CFD* simulations of scroll machines and variable thickness geometries. The geometrical characterization of scrolls is then analyzed in chapter 3, which includes theoretical formulations for constant and variable thickness machines.

The main numerical developments performed by the author are collected in chapter 4. The first section includes a description of the quasi-static code PDSim and the original implementation of a variable thickness geometrical module. The other three sections are focused on the *CFD* software *OpenFOAM*. The main contributions in this framework are the **CoolFOAM** wrapper for the evaluation of real gas properties and the **scrollFOAM** libraries for the simulation of scroll machines.

Chapters 5 and 6 include the validation and different applications of the numerical tools. The analyses of real gas effects and expander operation constitute chapter 5, while a scroll compressor test case has been employed to validate and compare the scroll-related tools (chapter 6).

Lastly, an open-source tool-chain for the design and optimization of scroll machines is presented in chapter 7. In particular, the numerical tools developed have been integrated to optimize the introduction of variable thickness geometries in the scope of reducing the manufacturing costs of a scroll compressor.

1.4 Publications

Some of the contents presented in this thesis have leaded to the publication of scientific papers in international journals and conferences. Sections or extracts of these articles are included in the chapters of the current work. A list of these publications is provided below.
Journals:

- Fadiga, E.; Casari, N.; Suman, A.; Pinelli, M. **CoolFOAM: The CoolProp wrapper for OpenFOAM.** Computer Physics Communications, Volume 250, 2020, 107047.
- Fadiga, E.; Casari, N.; Suman, A.; Pinelli, M. **Structured Mesh Generation and Numerical Analysis of a Scroll Expander in an Open-Source Environment.** Energies 2020, 13, 666.

Conferences:

- Fadiga, E.; Casari, N.; Suman, A.; Pinelli, M. **Fluid thermophysical properties modelling in an opensource platform: CoolFOAM.** ECOS 2020 - Proceedings of the 33rd International Conference on Efficiency, Cost, Optimization, Simulation and Environmental Impact of Energy Systems.
- Fadiga, E.; Casari, N.; Suman, A.; Pinelli, M.; Ziviani, D. **Multi-component numerical investigation of a micro Organic Rankine Cycle.** 2020 IIR Rankine International Conference on Advances in Cooling, Heating and Power Generation, Rankine 2020.
- Fadiga, E.; Casari, N.; Suman, A.; Pinelli, M.; Montomoli F. **Design considerations and numerical simulations of variable thickness scroll geometries.** ECOS 2021 - Proceedings of the 34th International Conference on Efficiency, Cost, Optimization, Simulation and Environmental Impact of Energy Systems.
- Fadiga, E.; Casari, N.; Angel, B.; Picavet, A. **Flow computation inside a scroll compressor based on open-source code.** IOP Conf. Ser.: Mater. Sci. Eng. 1180 012015, 2021.

Chapter 2

Literature review

2.1 Scroll compressors

Scroll compressors have been extensively employed in air conditioning and refrigeration since the 1980s. Their success is mostly related to a low level of noise and vibrations, together with a small number of moving parts and a compact design. The architecture of the scroll geometry is the cornerstone of the design and optimization of the whole machine. The inventor of this technology, Léon Creux, has introduced in 1905 a scroll profile based on the involute of a circle, which is still the most spread solution [42]. However, various alternative profile shapes have been developed during the XX century [74, 113, 180].

From the last decade of the 20th century, scroll compressors occupy a reference position in the fields of air conditioning and refrigeration. For this reason, research institutions, universities and private companies have dedicated time and resources in the geometrical definition, thermodynamic analysis and numerical modelling of such machines.

One of the first geometrical models of a scroll compressor has been developed by Morishita et al. [115, 116], who investigated both the geometrical and dynamic aspects of the machine. From the geometrical point of view, they developed an analytical definition of a generic scroll compression chamber as follows:

$$V_i(\theta) = \pi s_p(s_p - 2t)w\left[(2i-1) - \frac{\theta}{\pi}\right] \tag{2.1}$$

Where the scroll pitch s_p is given by $s_p = 2\pi r_b$, i is an integer that depends on the discharge angle, and w is the width (or height) of the scroll wraps. Following the work of Morishita et al., Yanagisawa et al. [178] built a more complete geometrical model including the evaluation of the volume of the suction and discharge chambers.

The research path indicated by Morishita et al. and Yanagisawa et al. has been further expanded by Chen et al. [38, 39], who integrated the previous geometrical studies with

specific models for the leakages, the heat transfer and energy balances.

Wang et al. [170] detected manufacturing issues due to the absence of flexibility in the choice of the starting angle of the involute. Consequently, they carried out an analytical study for the description of the scroll chamber with arbitrary initial angles, including a geometrical model for the leakage areas. Finally, Bell's doctoral dissertation [17] includes an exhaustive section including all the aspects of geometrical modelling of scroll machines. The models presented by Bell are described in chapter 3, and they have been taken as a reference for the elaboration of the numerical tools presented in this thesis. Furthermore, Bell's work has been used as the starting point for the realization of the open-source code PDSim [21, 185], which is used for the quasi-static modelling of positive displacement machines. PDSim is one of the most important numerical tools employed in this work, and it is described in chapter 4.

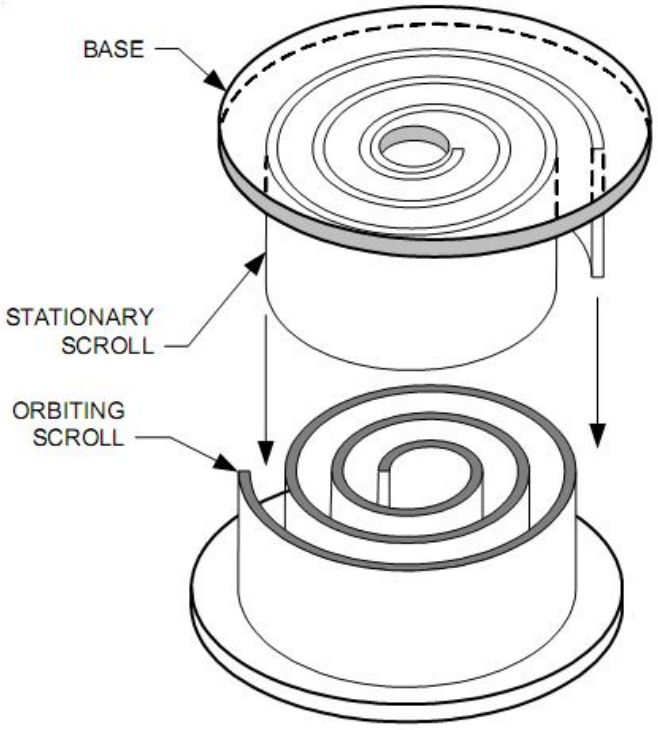

Figure 2.1: Scheme of the components of a scroll compressor.

2.1.1 Scroll tip geometry

The shape of the scroll tip has a significant influence on the final performance of the compressor. Both the volume ratio and the flow behaviour during the discharge process, with the introduction of blockage phenomena, can be modified by the choices of the designer. Three varieties of tip geometries are usually adopted: single arc, two arcs and arc-line-arc. These shapes are represented in figure 3.5 and extensively treated in section 3.1.1.

Analytical models for the evaluation of the volume of the discharge chamber in presence of single arc and two arcs tip geometries can be retrieved from the work of Blunier et al. [27]. On the other hand, Lee et al. [99] and Bell [17] have also analyzed the arc-line-arc configuration. The influence of the tip shape on the performance of the compressor has been studied by several researchers during the last decade. Shaffer and Groll [144] compared the three shapes and concluded that the arc-line-arc profile allows to reach higher volume ratios and to improve the compression process. Bell et al. [14] pointed out the possible lack of robustness, from the mechanical point of view, for certain single arc geometries. In general, the arc-line-arc is recognized as the most performance-oriented tip shape, but the two arcs geometry improves the smoothness of the discharge (in case of scroll compressors) and suction (in case of scroll expanders) processes.

2.1.2 Experimental studies and numerical models

During the last two decades, several researchers have conducted experimental studies and developed numerical models of scroll compressors employed in the refrigeration and air-conditioning fields. Winandy et al. [175, 176] published two of the first experimental studies of hermetic scroll compressors. In particular, they analyzed the effect of the suction temperature rise due to the heat transfer with the solid bodies of the compressor. Subsequently, the effects of vapour injection and liquid injection on the performance were investigated, detecting a slight increase in the cooling capacity due to the vapour injection. On the other hand, a strong decrease in the discharge temperature of the compressor was the main consequence of the liquid injection process. In both the studies, Winandy et al. used the experimental data to validate a simplified physical model based on an adiabatic compression process that substituted the actual scroll compressor operation. Cuevas et al. extended the work of Winandy et al. with the analysis of the operation of variable speed scroll compressors [43], adding a characterization of the operation of the machine under extended operating conditions [44]. The employment of variable speed compressors allows reducing noise and vibrations and reaching higher *Coefficients Of Performance (COPs)* than standard machines. However, the efficiency of the inverter integrated into the control system is one of the drawbacks of this solution, as well as the possible increase of leakages mass flow rate. Cuevas et al. measured a decrease of the *Coefficient Of Performance (COP)* ranging from 2 % to 5 %, due to the inverter efficiency. Degradation of the performance has been observed at low speeds (due to the internal leakages) and at high speeds (due to electro-mechanical losses). The authors developed a semi-empirical model validated using the experimental data but drew no conclusion on the convenience in the adoption of variable speed machines. An additional analysis on variable speed compressors is the one published by Park et al. [123], who showed that an increase in the frequency of the machine produces a compression process

that is closer to adiabatic compression. In the second article [44], Cuevas et al. presented a deep characterization of the compressor operation under extended conditions. They tested the refrigerant R134a at condensing pressures varying from 8.6 to 40.4 bar and evaporating pressure from 1.6 to 17.8 bar. One of the most interesting analyses of their work regards the connection between the pressure ratio and the efficiency of the compressor when the latter is forced to work in under-compression conditions.

In the last decade, one of the most active research groups in the scroll compressors field operates at the Department of Mechanical Engineering of Purdue University. Bell et al. [12] tested an air-conditioning oil-flooded compressor, measuring a general increase in the refrigerant R410a mass flow rate and overall isentropic efficiency, as a result of the oil injection. As already stated by Winandy et al. [175], they have also highlighted a decrease in the compressor discharge temperature as an additional effect of the oil injection. Research activities on a quasi-isothermal compression obtained injecting oil have been carried on by Ramaraj et al. [134], who performed an experimental campaign on a scroll compressor working with R410a. The oil was injected into the suction chamber, obtaining once again an increase in refrigerant mass flow rate and a decrease in compressor discharge temperature. In this case, an optimal value of oil fraction was found at the maximum of the isentropic efficiency, as a consequence of the trade-off between the increase of pressure drops and the decrease of the leakage effects. Lastly, in 2016, James et al. [83] developed a semi-empirical model for a scroll compressor with oil-flooding via liquid injection. The model, able to cope with a wide variety of working fluids, has been integrated into a vapour-compression system model, allowing for a rapid evaluation of the compressor losses.

Recently, Navarro, Tello-Oquendo et al. [47, 121, 162, 163] have focused on vapour injection and two-stage scroll machines. Navarro et al. [121] conducted a wide series of experimental tests on a vapour-injected scroll compressor, comparing it with an analogous machine working with no injection. The results indicated a lower efficiency of the machine but showed different advantages such as a higher *COP* of the thermodynamic cycle and a lower discharge temperature. Tello-Oquendo et al. [162] carried out a similar analysis, comparing a vapour-injected scroll compressor with a two-stage scroll compressor and a two-stage reciprocating compressor. They concluded that the vapour-injected machine is less flexible when the conditions deviate from the design point, but easier to employ from the machining point of view. Additionally, they observed a higher efficiency and *COP* of the two-stage compressor when working with pressure-ratios higher than 5. In general, the two-stage reciprocating machine has been identified as the worst alternative, being less efficient than the scroll compressors over the whole range of the analyzed pressure ratios. The experimental findings were compared to the results of a semi-empirical model presented by the same authors [163].

A different research line is the one proposed by Luo [107] and by Xu et al. [177], who analyzed the feasibility of systems employing R32 as the working fluid. The main issue of this fluid is related to the discharge temperature, which can heavily limit the operating range of the compressor. Xu et al. [177] conducted an experimental campaign on the employment of a mixture of R1234yf and R32 in vapour-injected heat pumps, while Luo [107] suggested the adoption of an oil-flooded compression cycle with regenerator to limit the discharge temperature.

The role of the industrial environment in the research and development of scroll compressors is also an important factor. The experimental campaign performed by Picavet et al. [130] from *Danfoss Compressors* has been adopted as the experimental reference for the validation of the numerical tools presented in this thesis. Similarly, *Emerson* collaborated in the development and validation of a reliable semi-empirical model of a scroll compressor for vapour compression systems [46].

The development of semi-empirical models has been particularly popular in several papers presented in this section. An innovative modelling option was introduced in the recent work of Zendehboudi et al. [182], who employed AI models such as ANN and ANFIS to estimate the performance parameters of the scroll. On the other hand, Diniz et al. [51] used more traditional models based on thermodynamic relations to analyze the temperature distribution along the scroll wraps.

2.2 Scroll expanders

The importance of *ORCs* in *Waste Heat Recovery (WHR)* and renewable energies exploitation has been widely treated in the literature during the last decades [108, 132]. The two main advantages of this technology are related to the simplicity of the system and to the availability of the components. At the state of the art, design and optimization of *ORCs* are based on thermodynamic models and experimental studies. As an example, Kang has designed and analyzed an *ORC* using experimental studies [88]. Leal et al. have focused their work on the design of a micro-*ORC* adapted to a solar domestic hot water system [97], while Kennich et al. have presented an optimal design of *ORC* systems with a low-temperature heat source [89]. Experimental studies are reported in several previous works: Bianchi et. al.[24], Dickes et al. [49] and Peris et. al. [125] have conducted analyses on micro-*ORC* systems performance. Different types of volumetric expanders have been compared and tested in a small-scale *ORC* by Dumont et al. [52], while Ziviani et al. [186] have investigated the effects of the working fluid charge. A scheme of the most common *ORC* expanders is reported in figure 2.2, which classifies the components according to their power range and field of application.

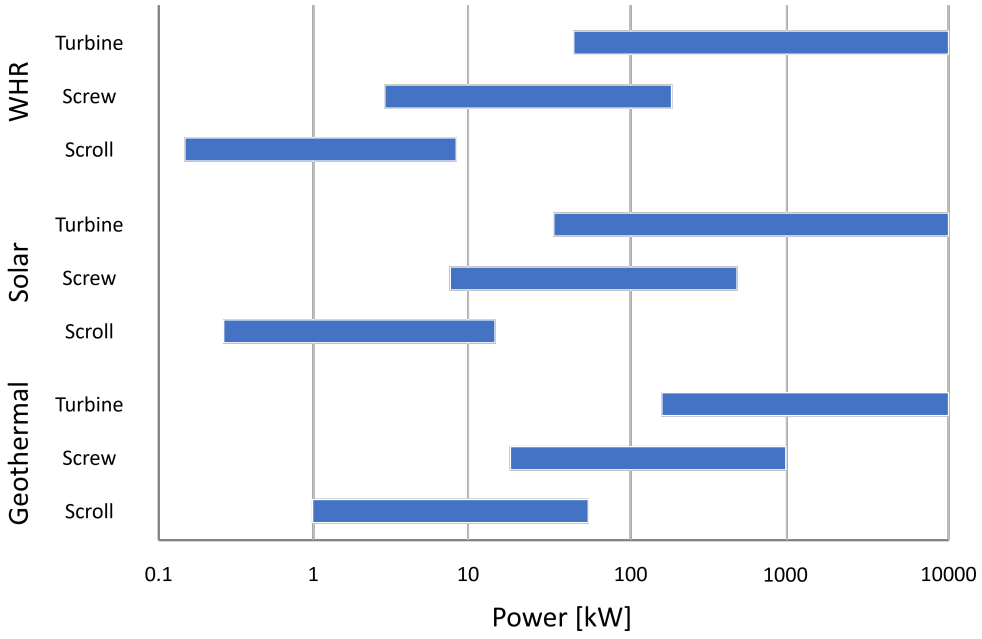

Figure 2.2: Classification of ORC expanders.

Scroll expanders are frequently adopted in micro-*ORCs* with power outputs up to 2 kW, as described in different literature works reporting experimental tests. Wang et al. [171] have tested a scroll expander with R134a over a wide range of rotational speeds, reaching a shaft work output close to 1 kW.

More recent fields of applications of scroll expanders are the recovery of expansion power in vapour compression systems [119] and the small-scale compressed air energy storage [183]. The first one is a method to improve the energy efficiency of refrigeration systems, while the second employs a scroll machine for charging and discharging the compressed air storage.

At the state of the art, scroll expanders are difficult to purchase on the market, since the development of industrial machines is still at an early stage [149]. For this reason, the most common solution adopted by researchers is running scroll compressors in reverse. As a consequence, different types of scroll compressors have been adapted to work as expanders [149]: semi-hermetic and open-drive automotive compressors for air-conditioning, hermetic refrigeration scroll compressors and open-drive air compressors.

Several researchers have investigated the performance of hermetic scroll compressors operated as expanders: among them, Mathias et al. [109] measured a maximum isentropic efficiency of 83 %, while Bracco et al. [29] reached a value of 75 % analyzing a machine working with R245fa. Ayachi et al. [7] reached a lower efficiency in their analysis of a hermetic scroll expander installed in a Brayton cycle fed with R245fa.

Semi-hermetic scroll compressors are lighter and more compact machines, frequently installed in automotive *Air/Conditioning (A/C)* units. Hoque et al. [78] and Jradi et al. [85] investigated experimentally these machines operated as expanders, reaching efficiencies

comparable to the ones reported for hermetic compressors. More recently, Kutlu et al. [95] focused on the accurate characterization of leakages and friction in a semi-empirical model of a semi-hermetic expander. In particular, the leakage areas and the friction coefficient have been varied as functions of the pressure ratio and rotational speed, respectively.

Open-drive automotive scroll compressors are one of the typologies that have been converted the most into expanders. One of the first experimental investigations of these machines is the one performed by Saitoh et al. [141], who reached a maximum isentropic efficiency of 63 % with an expander employed in a solar *ORC*. Similar values of efficiency were obtained by Mendoza et al. [110], who measured a maximum overall isentropic efficiency of 61 % corresponding to a net mechanical power of 958 W for an *ORC* working with ammonia. In the last years, Muye et al. [120] developed and validated a generalized semi-empirical model, characterized by a reduced computational time and accuracy comparable with "non-generalized" semi-empirical models.

An open-drive scroll air compressor has been investigated as expander in 2009 by Lemort et al. [103], obtaining a maximum output power of 1.8 kW with an isentropic efficiency of 68 %. In particular, they observed how over-expansion plays an important role in reducing the expander efficiency. In 2013, Zhou et al. [184] conducted a similar experimental investigation employing the same fluid as Lemort et al., the refrigerant R123. Lastly, in 2018, Ziviani et al. [187] tested a prototype working with R245fa and underlined the importance of mechanical losses (up to 19 %) during the operation of the expander.

2.3 CFD simulations of scrolls

Recently, industries and researchers have begun to include *CFD* analyses in scroll machine designs and optimizations [68, 129, 150, 157, 159, 173]. The flow inside positive displacement machines has a complex three-dimensional nature, especially in correspondence of suction and discharge regions. Unfortunately, such flow features are either impossible or extremely costly to determine experimentally. Hence, *CFD* represents a suitable method to perform a complete analysis of the dynamic behaviour of positive displacement machines. This tool allows to retrieve information about leakage flows nature, temperature distribution, and three-dimensional behaviour of the flow inside the expander/compressor. Moreover, *CFD* could be employed to tune analytical and thermodynamic models as low-cost alternatives to experimental campaigns. One of the most challenging aspects of computational analyses of scroll machines (and positive displacement machines in general) is the grid generation process.

The nature of the problem imposes to adopt a dynamic mesh approach in order to correctly model the moving parts of the machine. Casari et al. [33] have reviewed different

approaches for the dynamic mesh treatment in screw machines numerical analyses, including immersed boundary, adaptive remeshing, and key-frame remeshing. Most of the techniques presented in their work are suitable also for scroll expanders and compressors, but the most popular approach is certainly the custom predefined mesh generation [135]. This technique is based on the realization of a user-defined number of grids per rotor pitch. Each grid represents a set of control points (coordinates) through which the mesh nodes have to pass during the simulation. Several examples of this approach can be found in the literature, including applications to screw machines [10, 92, 93, 136], root machines [31, 147], and scroll machines [50, 68, 75, 159]. This sound method allows obtaining good accuracy reducing conservation errors, as extensively described in section 4.4.1. However, a number of works have been performed with re-meshing techniques [54, 114, 148] or cartesian cut-cells methods [22, 126, 139].

The analyses based on pre-defined mesh generation available in the literature, are mainly realized using commercial *CFD* software and mesh generators focused on positive displacement machines. In particular, the mesh generator *Twin Mesh* [37] has been used by Hesse et al. [75] to simulate a scroll vacuum pump considering thermal deformation with ANSYS CFX. The same computational workflow has been applied by Picavet et al. [127, 128] to simulate the same compressor analyzed in chapter 6 of this thesis, respectively with and without *Intermediate Discharge Valves (IDVs)*.

The mesh generator and *CFD* software *SimericsMP+* [146] has been used by Cavazzini et al. [36] to perform a *CFD*-based optimization and uncertainty quantification of a scroll compressor. Gao et al. [67], the developers of the *SimericsMP+* software, have presented an interesting solution for the treatment of tip seals. The same code has been employed by [158], who performed a numerical analysis focused on the suction process.

The *CFD* results presented in this thesis, based on the framework developed by the author [58], have been experimentally validated using the data obtained by Picavet et al. [130]. Chapter 4 includes a description of the set of C++ libraries for the generation of structured body-fitted meshes of scroll compressors and expanders. Starting from the scroll profiles and main dimensions, the mesh is generated by means of an elliptic grid generation algorithm. These libraries have been realized in accordance with the coding standards of the open-source *CFD* software *OpenFOAM*. *OpenFOAM* [174] is a widely used open-source C++ toolbox for the numerical simulation of a wide series of *CFD* problems. This package contains several libraries and applications to pre-process, solve and post-process cases from different fields of application (e.g, incompressible flow, compressible flow, multiphase flow and conjugate heat transfer problems). The structure of *OpenFOAM* enables the user to modify existing solvers and libraries or to create new applications with a reasonable effort. As a consequence, a great number of personalized solvers and libraries have been developed by

the scientific community. The exponential growth of this open-source software's capabilities in modelling real-world problems is recognizable in several fields. The range of applications varies from incompressible flows with heat transfer [45] to density-based solvers for low and high Mach numbers [145]. Moreover, wall modelling in *Large Eddy Simulation (LES)* simulations [118] and mass transfer in solid oxide fuel cells [122] have been recently treated in literature works. The simulations presented in [58], [57], [55] and [60] (a simulation including the cycle integration of a scroll expander), represents a series of open-source studies that have been carried out by the author. To the author's knowledge, these are the only *CFD* simulations of scroll machines performed with open-source software. The results represent proof of the reliability that open-source software have gained over the last years.

2.3.1 Leakages and sealing

There are two different types of leakages that reduce the performance of scroll compressors and expanders, as represented in figure 2.3.

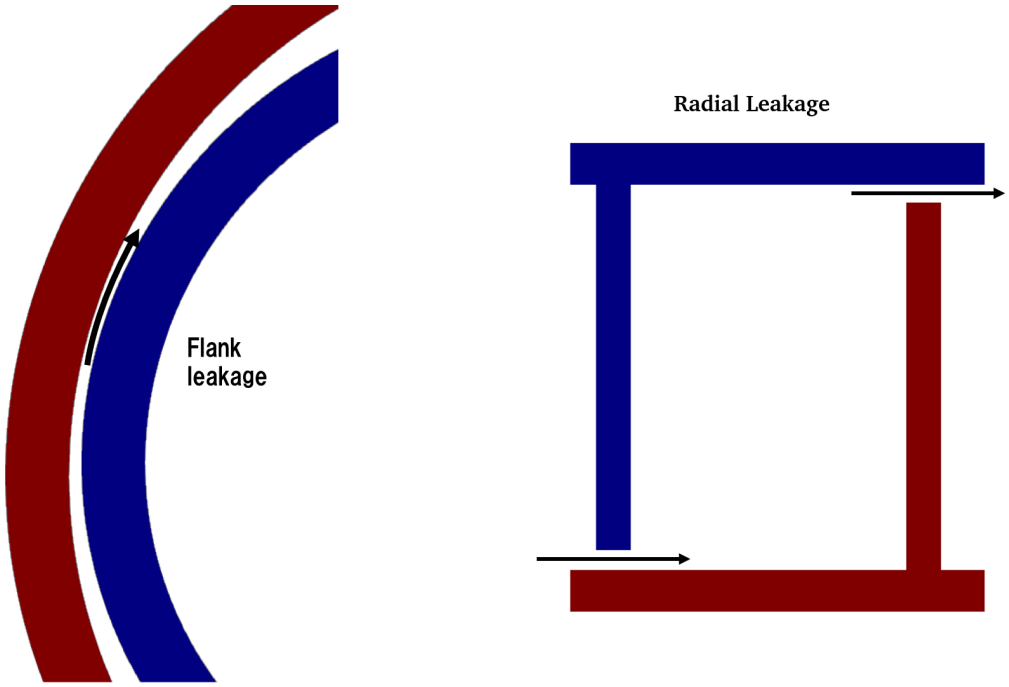

Figure 2.3: Scroll leakages.

The first leakage is the one between the scroll plate and the scroll wraps, through the axial clearance, and it is called radial leakage. The other one flows through the flank gap, which is given by the clearance between the orbiting and the fixed wrap.

The volumetric efficiency is defined by the ratio between the mass flow rate that actually leaves the scroll and the theoretical mass flow rate given by the displacement of the machine. As a consequence of these leakages, the volumetric efficiency is generally reduced. However, in the case of scroll compressors working in over-compression and scroll expanders, the

volumetric efficiency may be increased by the presence of the leakages. Anyway, this increase is only a numerical increase of a performance indicator, because the machine is actually wasting useful power. In the case of the compressor working in over-compression, too much power is used to increase the pressure of the fluid, resulting in a leakage that goes from the compression chamber to the discharge port. For the expander, the flow through the gaps is in the same direction of the main flow of the machine, but it is not producing useful power.

The radial leakages can be reduced by using tip seals, while the flank gap can be reduced only increasing the quality of the machining process. In general, the injection of oil has a sealing effect that contributes increasing the volumetric efficiency of the scroll. Li et al. [105] have presented an interesting experimental analysis on the influencing factors of axial clearances of scroll compressors, concluding that the revolution speed has more influence on the axial clearance than the temperature. Increasing the speed, the axial clearance is gradually reduced. Similarly, they recorded a slight decrease in the gap width as a consequence of a temperature rise. In addition to that, the overturning moment has been identified as an additional important factor.

An overview of the sizes of the gap widths adopted by the authors of several scroll models, obtained from Bell et al. [17] and Song et al. [149], is reported in table 2.1.

Authors	**Flank gap [µm]**	**Radial gap [µm]**
Yuan et al. [181]	10	10
Suefuji et al. [156]	5-15	5-15
Ishii et al. [82]	10	20
Cho et al. [40]	37-52	10-30
Lee et al. [98]	15	10
Kang et al. [87]	10	15
Kim et al. [90]	64	40
Lemort et al. [104]	10	40
Yang et al. [179]	49-75	49-75
Bell et al. [18]	5-25	5-25

Table 2.1: Review of gap sizes in literature works.

Pereira and Deschamps [124] have developed correlations of leakages flow rates in scroll compressors based on *CFD* simulations of a portion of scroll chambers, using the ideal gas flow approximation. However, the modelling approach of leakage flows is probably the most challenging aspect of *CFD* simulations of scroll machines, especially when a complete geometry is moving. It must be considered that the geometry of the scroll wraps is slightly modified by heating and cooling phenomena linked to the compression process, as well as mechanical loading. Considering that the gap sizes are usually below 100 µm, even small

variations can produce non-negligible effects on the volumetric efficiency of the compressors. An additional aspect to be considered is the presence of tip sealing components, which reduce radial leakages. The sealing capacity of tip seals is not constant, since friction and wear influence the mass flow rate of refrigerant. The importance of tip sealing is treated in the work dedicated to leakages in scroll expanders realized by Rossi Fanti et al. [61].

Modelling all these aspects would require a wide range of complex computational methodologies, ranging from *Fluid Structure Interaction (FSI)* to special treatments for thermal deformation and tip seals efficiency. Moreover, in the case of oil-flooded machines, a multiphase simulation would be necessary to estimate oil sealing effects. However, it is possible to reach good levels of accuracy by setting a constant gap size, which can be tuned with the help of experimental data. It should be noticed that gap modelling in the case of structured grids is naturally included as the mesh is squeezed with little quality degradation. The same would not be that smooth with other moving mesh techniques. Cut-cell methods, for example, are less accurate in the computation of the leakage flow. For example, in the analysis reported in [126], the authors justify the mismatch in the indicator diagram with an under-resolution of the leakage flow. The difference is greater as the rotational speed of the scroll increases. An improvement of the results can be achieved with an increased mesh resolution but at the expense of the computational speed. Non-conservative methods are typically applied for modelling the gap behaviour, e.g. sinks of momentum [139].

2.3.2 Real gas properties

The evaluation of thermophysical properties of working fluids is a fundamental step in *CFD* simulations. For example, it is quite common to operate with compressible fluids that exhibit real gas behaviour: in this case, cubic *Equations Of State (EOS)* are frequently used to predict fluids properties in both single-phase and two-phase regions. These *EOS* represent a good compromise between the simplicity of the formulation and the uncertainty in the determination of such quantities. Cubic *EOS* are frequently adopted to characterize phase equilibrium. Moreover, for this kind of equations, different approaches to model mixtures exist [81]. Nevertheless, the critical region is an area characterized by significant deviations from experimental data, because the cubic models do not account for critical phenomena. Furthermore, these models lack accuracy in the calculation of thermodynamic properties, in particular at dense homogeneous states [69]. This kind of inaccuracy sources can be relevant during the numerical simulation of systems operating in different fields, such as refrigeration (e.g., vapor compression cycles), cogeneration (e.g., *ORC*) and energy production (e.g., supercritical CO_2 cycles) [6, 8, 9, 32, 34, 77].

Recently, more accurate models for the thermodynamic properties calculation have been developed: modern equations are often formulated in terms of the reduced Helmholtz energy,

which is split up into one ideal gas part and a second residual part. The first one defines the nature of the hypothetical ideal gas at given values of temperature and density, while the second one characterizes the residual behaviour of the real fluid. The resulting equation of state is explicit in temperature and density normalized by the fluid's critical values. [153]. Multi-parameter equations of state can characterize experimental measurements in Helmholtz-explicit relations. Using these equations of state, thermodynamic properties can be then calculated using thermodynamic relationships, through the differentiation of the equations. The range of applicability of these models includes the liquid phase, differently from the cubic equations, and the behaviour in the critical region is represented with a reasonable error [70].

There are various libraries and databases that have implemented Helmholtz-explicit equations of state for different fluids [19, 91, 101, 169]. In addition to thermodynamic models, high accuracy formulations for transport properties are included in these utilities. The state of the art of transport properties modelling is less mature than the thermodynamic properties one: one of the causes is that an accurate formulation of thermodynamic properties is needed to develop a high-accuracy transport properties model. For this reason, a natural delay between the publication of an equation of state and the related transport properties model occurs [19]. The CoolProp library represents the most used library in the open-source scenario for the evaluation of thermo-physical properties [19]. The code is written in C++, and several high-level and low-level interfaces have been developed to couple CoolProp with different software (e.g. Labview, Microsoft Excel, MATLAB).

In addition to the scroll machines related libraries, the author has developed a wrapper of CoolProp for *OpenFOAM*. The CoolFOAM wrapper intends to fill a gap in the OpenFOAM capabilities of modelling the thermophysical properties. Similar tools have already been developed in the field of commercial *CFD* software (e.g., the link between ANSYS fluent and REFPROP [101]). Section 4.3 of this thesis extends the applicability of one of the most widespread open-source *CFD* software, eliminating this gap.

2.4 Variable thickness scrolls

The *Variable Thickness (VT)* in scroll geometries is a characteristic that has been introduced in order to speed up the compression process, thus reducing the spiral length. Indeed, *VT* reflects in a non-constant-radius circle involute that generates the spiral. This leads to a non-uniform compression rate in the compression chamber operation, showing beneficial results in terms of leakage prevention and potential improvements in heat transfer mechanisms. Other applications may regard the increase of the pressure ratio keeping the same compactness of the machine, or the design of expanders/compressors with shorter spirals reducing the

machining costs. The benefits summarized above could justify the adoption of this solution at an industrial level. However, the literature for VT scrolls is quite limited and mainly focused on theoretical works, and the research and development are still at an early stage.

The possibility of designing VT scroll compressors have been introduced by researchers in the last decade of the 20th century [30, 66, 72, 106]. The work published by Bush et al. [30] in 2002 is one of the first examples of scroll geometries with non-constant thickness. They developed a geometric formulation that allows generating conjugate scroll profiles of almost any form. Gagne et al. [66] presented a geometrical software based on the same generalized conjugate equations. Their formulation is based on the definition of a swing radius and a generating radius, which determine the position of a point on a pitch line. The pitch line is identified by a series of contact points between the inner surface of one wrap and the outer surface of the other wrap. The position vector, in complex polar form, is given by:

$$\mathbf{P} = R_s(\alpha)e^{j\alpha} + R_g(\alpha)e^{j(\alpha+0.5\pi)} \tag{2.2}$$

The definition of the swing radius R_s and the generating radius R_g is illustrated in figure 2.4. The combination of the two radii define the pitch line.

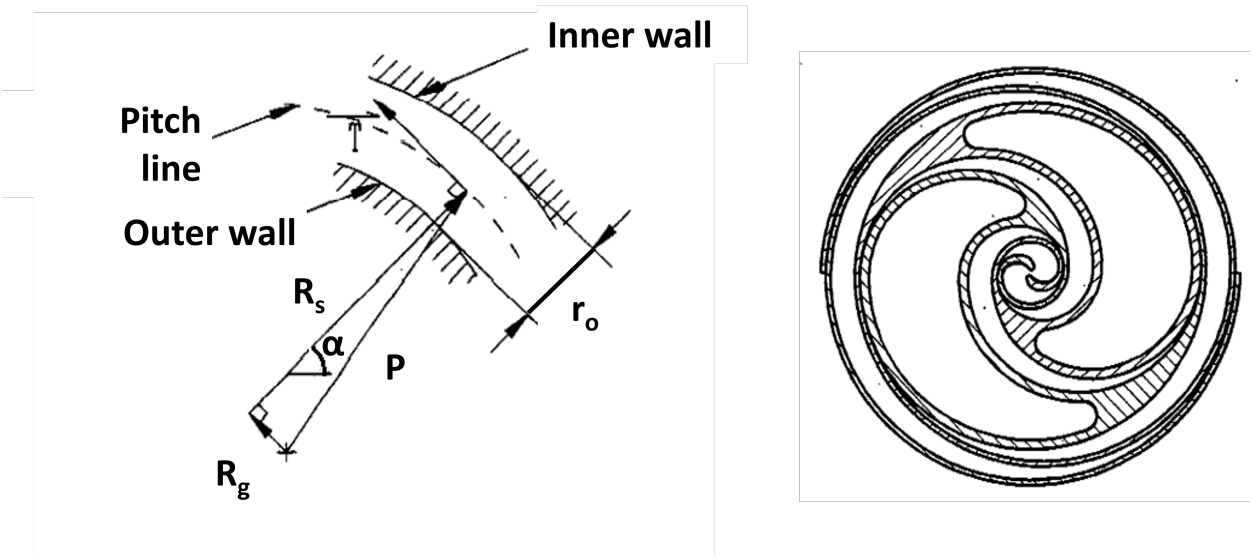

Figure 2.4: Geometrical definition of scroll compressors according to Bush et al., figure adapted from [30].

The swing radius equations available in the code developed by Gagne et al. are the following:

$$R_s = C_0 + C_1\alpha + C_2\alpha^2 + C_3\alpha^3 \tag{2.3}$$

$$R_s = C_0 + C_1 cos(\alpha + C_2) \tag{2.4}$$

$$R_s = C_0 + C_1(\alpha + C_2) \tag{2.5}$$

With the generating radius given by:

$$R_g = \frac{dR_s}{d\alpha} \tag{2.6}$$

The employment of different equations for R_s and different constants (C_0, C_1, C_2, C_3) allows producing traditional scrolls, but also VT geometries such as the one reported on the right side of figure 2.4.

Lindsay et al. [106] proposed a VT formulation based on an arbitrary path of the scroll wraps, named *milling tool path*. Their work is characterized by interesting geometries, but the mathematical basis employed are not reported with sufficient clarity.

In 2001, Gravesen and Henriksen [72] have formalized an interesting mathematical generalization of scroll compressor geometries. The introduction of VT wraps in their framework has been basically executed by altering the derivative of the curvature radius of the spiral curve, and it is further described in section 3.2, since their formulation has inspired the one used in this thesis.

More recently, Shaffer et al. [144] started from the formulation of Gravesen and Henriksen, using a third-order polynomial with the tangent direction as the independent variable to describe the curvature radius of the spiral. Furthermore, they adapted the arc-line-arc formulation for the tip region to the VT formulation, obtaining more advanced geometries.

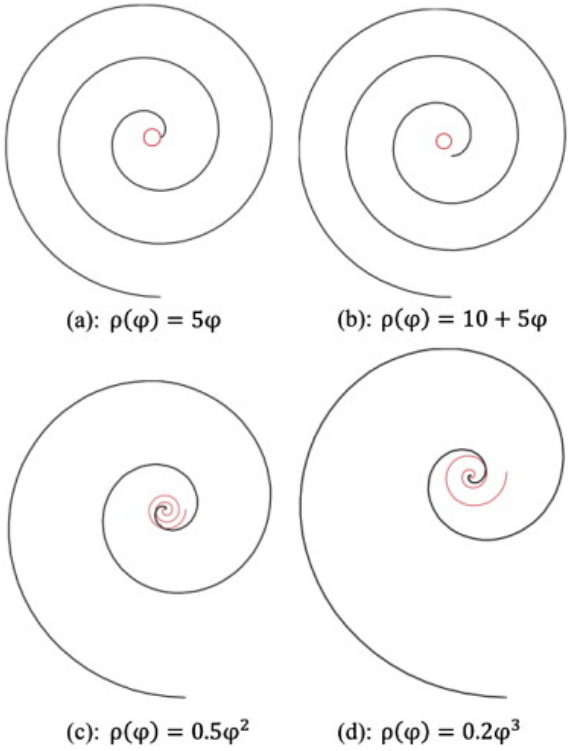

Figure 2.5: Scroll curves determined with the formulation published by Shaffer et al., figure adapted from [144].

The equation for the evaluation of the curvature radius is the following:

$$\boldsymbol{\rho}(\Phi) = a + b\Phi + c\Phi^2 + d\Phi^3 \tag{2.7}$$

Where $\boldsymbol{\rho}$ is the curvature radius, Φ is the tangent angle, and a, b, c, d are arbitrary constants. Some examples of resulting curves are represented in figure 2.5

In 2017, Bin et al. published two papers [25, 26] including a piece-wise representation of the scroll curves. They developed a model based on a series of different curves, where R_g and R_s are analogous to the ones of figure 2.4:

Base-line equation

$$\begin{aligned} x(\Phi) &= R_g \cos\Phi + R_s \sin\Phi \\ y(\Phi) &= R_g \sin\Phi - R_s \cos\Phi \end{aligned} \tag{2.8}$$

High order curve

$$R_s = C_0 + C_1(\Phi - 0.5\pi) + C_2(\Phi - 0.5\pi)^2 + C_3(\Phi - 0.5\Phi)^3 \tag{2.9}$$

$$R_g = C_1 + 2C_2(\Phi - 0.5\pi) + 3C_3(\Phi - 0.5\Phi)^2 \tag{2.10}$$

Circle involute

$$R_s = a\Phi \tag{2.11}$$

$$R_g = a \tag{2.12}$$

Non-working arc

$$x(\Phi) = k\cos\Phi + j \tag{2.13}$$

$$y(\Phi) = k\sin\Phi \tag{2.14}$$

Twin-circular arcs modification profile

$$x(\Phi) = e_i\cos\Phi + d_i \tag{2.15}$$

$$y(\Phi) = e_i\sin\Phi + c_i \tag{2.16}$$

Where C_0, C_1, C_2, C_3, e_i, d_i, c_i, k, j, a are different constants. These curves have been ordered as follow, starting from the outermost curve of the outer wall of the spiral:

- Non-working arc (Outer wall)
- High order curve (Outer wall)

- Circle involute (Outer wall)
- Twin-circular arc (Tip of the wrap)
- Twin-circular arc (Inner wall)
- Circle involute (Inner wall)
- High order curve (Inner wall)

Bin et al. performed an interesting and detailed analysis of both the geometry and the operation of the compressor, including a dynamic model of the machine. However, this type of compressor has some disadvantages related to flexibility and complexity of the formulation. Several figures of the resulting geometries are included in the original document [25].

Numerical analyses of *VT* geometries have been performed very rarely according to the literature. One of the examples is the *CFD* simulation of a single chamber of a *VT* scroll compressor built starting from the formulation of Bush et al. [30]. This analysis has been performed by Rak et al. [133], who performed a comparison between the *VT* geometry represented in figure 2.4 and a constant thickness reference scroll. The wall heat transfer coefficient of the *VT* scroll, characterized by a faster compression process, resulted larger than the analogous of the reference geometry. These preliminary results suggest that this kind of *VT* compressors may have an increased efficiency due to a compression process that is closer to an isothermal process.

An additional contribution including a *CFD* analysis of a *VT* expander is included in the publication of Emhardt et al. [54]. They used commercial software to generate an unstructured mesh and apply the unconventional technique of dynamic re-meshing to perform the simulation. The gap sizes employed, from 75 µm to 200 µm, are quite large, probably because the number of cells of an unstructured grid would rise exponentially with more realistic gap widths. The gap widths highly influenced the results obtained by Emhardt et al., who reached a maximum isentropic efficiency of 53.9 %. No comparison with constant thickness geometries was included in the publication.

Chapter 3

Scroll compressor geometry

In this chapter, the geometrical models of the scroll machines employed in this thesis are presented. Bell [17] has treated extensively the geometrical modeling of constant thickness scrolls in his PhD thesis. His model, which is described in section 3.1, has been expanded to include variable thickness geometries, following the work of Gravesen and Henriksen [72] as the main reference. The variable thickness model implemented by the author is reported in section 3.2.

3.1 Constant thickness

The geometry of scroll compressors is constructed on the geometrical concept of an involute unwrapping from a circular evolute (the locus of all the centres of curvature). The position of one point on this involute is the result of the sum of two vectors. The first one is directed from the origin to a point on the evolute, while the second one from the evolute to the final point on the involute.

This representation is synthesized in Figure 3.1, and it is important to notice how the second vector mentioned above always corresponds to the curvature radius $\boldsymbol{\rho}$ of the analyzed point. In fact, one of the most important properties of this type of spirals is the proportionality between the curvature radius and the value of the angle tangent to the curve (Φ).

If the origin of the reference system is placed in correspondence of the centre of the evolute, the position of a point on the involute is given by:

$$\begin{aligned} x(\Phi) &= r_b(\cos\Phi + (\Phi - \Phi_0)\sin\Phi) \\ y(\Phi) &= r_b(\sin\Phi - (\Phi - \Phi_0)\cos\Phi) \end{aligned} \tag{3.1}$$

The starting angle of an involute is set as Φ_s, while the end of the curve is placed at Φ_e.

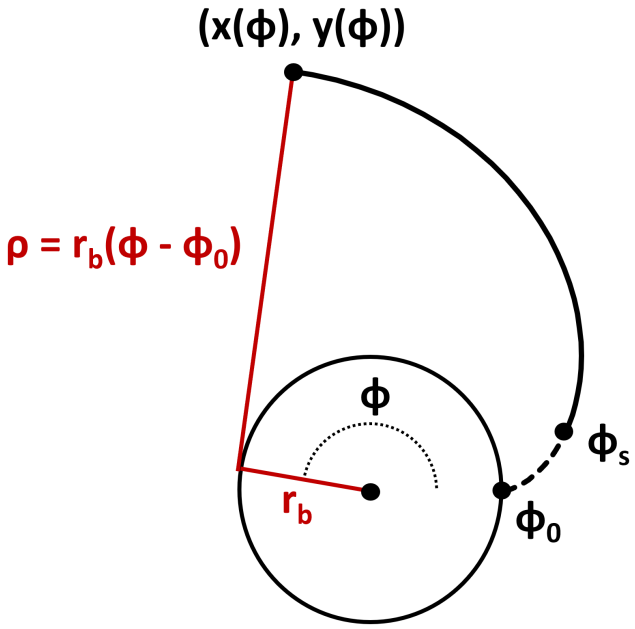

Figure 3.1: Scroll compressors involute representation.

The part of the curve from Φ_0, the initial angle of the involute, and Φ_s is represented as a dotted line in figure 3.1. Actually, in a real compressor that section is replaced by a series of arcs and lines to build the tip geometry.

The same involute can start from different values of Φ_0: two of these curves represent the inner and outer surfaces of a wrap of the scroll. Consequently, the thickness of the scroll wrap can directly be connected with the difference between the initial angles of the two involutes characterizing that wrap. This relation is reported in equation 3.2

$$t = r_b(\Phi_{i0} - \Phi_{o0}) \tag{3.2}$$

The coupling of the inner and outer surface of the scroll wrap and a scheme of the angle defined in the first part of this section are reported in figure 3.2. The first subscript, i or o, refers to the inner and outer curve, while the second one is consistent with the angles notation presented above.

The orbiting wrap is then created by reflecting the fixed scroll through the origin of the coordinate system. Following the reflection, an offset is placed between the orbiting scroll and the centre of the base circle of the fixed scroll. This offset is the orbiting radius, and the centre of the base circle of the fixed scroll is the orbiting centre of the moving wrap.

The calculation of the orbiting radius is based on the conjugacy between the two wraps. In particular, the relation derived by Bell [17] is reported in equation 3.3:

$$r_o = r_b\pi - t = r_b(\pi - \Phi_{i0} + \Phi_{o0}) \tag{3.3}$$

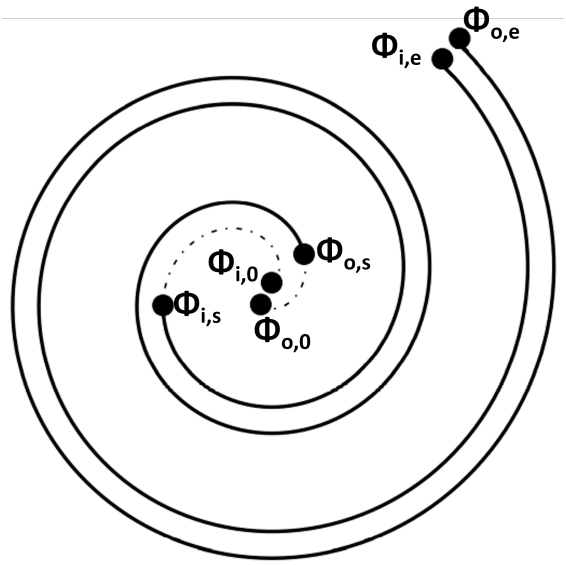

Figure 3.2: Scroll wrap and fundamental angles.

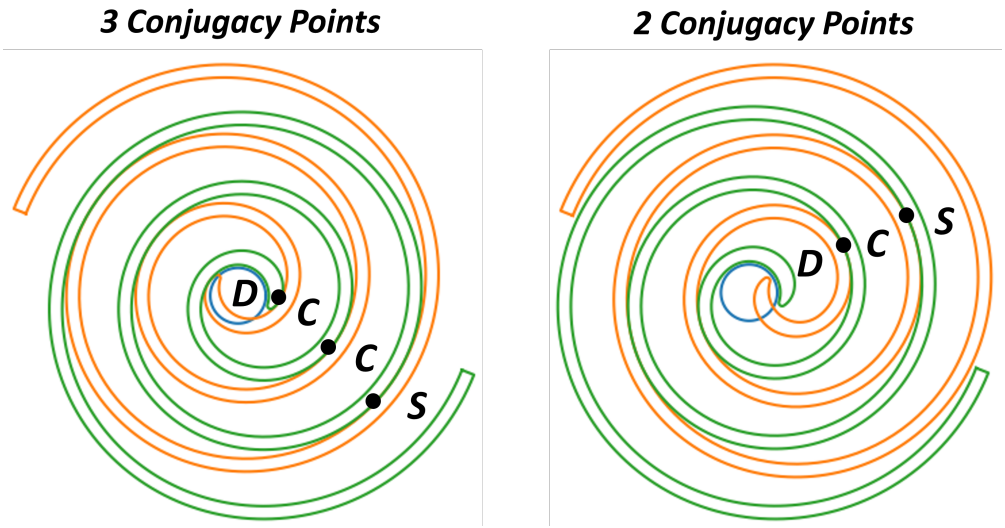

Figure 3.3: Scroll compressor conjugacy points. (S = Suction chamber, C = Compression chamber, D = Discharge chamber)

The two scrolls must be in perfect contact during the whole orbiting process, sharing a number of tangent points related to the number of compression chambers that work together at the same time.

As reported in figure 3.3, the orbiting position characterized by 3 conjugacy points has a suction chamber, two active compression chambers and a small discharge chamber in the centre. On the contrary, 2 conjugacy points correspond to a single compression chamber and a definitely bigger discharge chamber. The suction chamber, in this case, is close to being sealed becoming the new outermost compression chamber.

The notation for the definition of the compressor chambers is reported in figure 3.4. In this thesis, only symmetrical compressors have been considered. For this reason, it is possible

to individuate couples of identical chambers in the machine. The two compression paths are identified by indexes 1 and 2, where the value 1 refers to the path with the fixed scroll as the outer surface. Moreover, there is a common volume in the suction region, which is placed between the wraps and the shell of the machine. This particular region is connected to both the compression paths and it is named **sa**.

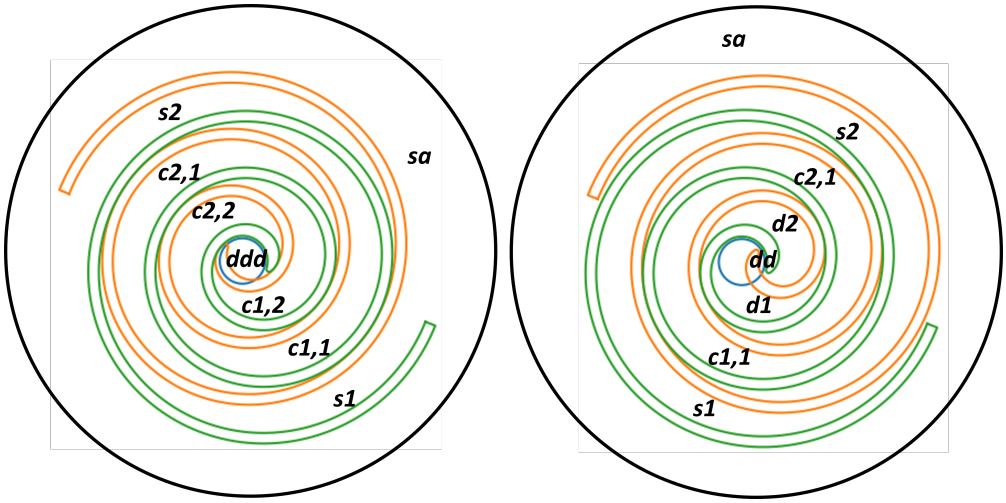

Figure 3.4: Scroll compressor chambers.

The suction chamber of the first path is named **s1**. Similarly, the compression chamber **c1,1** is the outermost compression chamber of the first path. The second index of the compression chambers is increased going in the direction of the centre of the machine. The discharge region is defined in two different ways: right after the discharge angle, the old innermost compression chambers (**c1,2** and **c2,2**) become **d1** and **d2**, while the central region is called **dd**. This situation is shown on the right side of figure 3.4. When the pressure of the three portions of the discharge chamber is equalized, this volume is considered a single discharge chamber called **ddd**.

3.1.1 Discharge geometry

Usually, the boundaries of the compression or suction chambers are constituted of involutes. However, in the discharge region, the main volume can be broken into three smaller parts, called d1, d2, and dd. d1 and d2 are the continuations of the concept of the compression chambers after the discharge angle. Differently, dd is the pocket that is directly linked to the discharge port.

The starting points of the outer and of the inner involute of a scroll wrap, placed at Φ_{is} and Φ_{os} must be connected by different types of curves. The conditions that must be respected during this connection are the following:

- The curve adjacent to the inner involute must be tangent to the involute itself at Φ_{is}.

- The curve adjacent to the outer involute must be tangent to the involute itself at Φ_{os}.
- The contact between the two wraps must be avoided during the whole orbiting process.

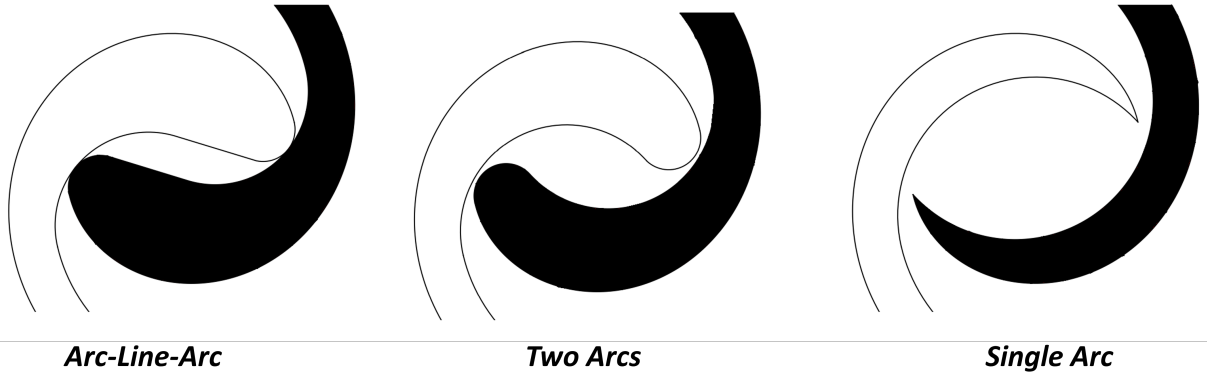

Figure 3.5: Scroll compressor discharge geometries.

The most common discharge curves adopted in the industry are reported in figure 3.5. The two arcs geometry is characterized by two arcs that are tangents to the two involutes and among each other. The single arc is a special case of the two arc solution where one of the two arcs degenerates to a point. Lastly, the arc-line-arc geometry contains two arcs that are tangents to the two involutes and are connected with a line tangent to both the arcs.

3.2 Variable thickness

Following the work of Gravesen and Henriksen [72], the derivative of the radius of curvature of the reference spiral has been defined as a piece-wise function to influence the thickness of the scroll wrap:

$$\frac{d\boldsymbol{\rho}}{d\Phi} = \begin{cases} r_b & \Phi \in [\Phi_s, \Phi_e] \setminus [\Phi_A, \Phi_A + 2\pi] \\ r_b + \frac{h}{\pi} & \Phi \in [\Phi_A, \Phi_A + 2\pi] \end{cases} \tag{3.4}$$

The basic radius r_b is calculated using the equation $r_b = (r_o + t)/\pi$, where t is the initial thickness of the scroll wraps and r_o is the orbit radius. The term h is an arbitrary increment applied to the derivative of the curvature radius. Although negative increments produce technically feasible geometries in some cases, it is important to check the validity of the geometries according to [72]. The angle Φ_A represents the start of the area with altered thickness, while Φ_s and Φ_e are respectively the starting and the ending angle of the reference spiral.

Consequently, the curvature radius $\boldsymbol{\rho}$ and the position of the points $\mathbf{x_0}$ on the reference spiral as functions of the tangent direction Φ are given by:

$$\boldsymbol{\rho}(\Phi) = \rho_0 + \int_0^{\Phi} \frac{d\boldsymbol{\rho}}{d\Phi} d\Phi, \tag{3.5}$$

$$\mathbf{x_0}(\Phi) = (r_b, 0.0) + \int_0^{\Phi} \boldsymbol{\rho}(\cos\Phi, \sin\Phi)d\Phi, \tag{3.6}$$

where ρ_0 is a constant value to be defined in accordance with the geometrical transformations that have to be applied to $\mathbf{x_0}$ to retrieve the inner and outer walls of the scroll wraps. The notation (x, y) indicates a two-dimensional vector with x and y coordinates, and bold variables represent vectors themselves. The position of the inner wall of the fixed spiral of the compressor is obtained by translating $\mathbf{x_0}$ in a circular orbit of radius r_o. The equation for the inner and outer curves of the fixed ($\mathbf{y}$) and mobile ($\mathbf{x}$) spiral, which derive from the reference spiral $\mathbf{x_0}$, are synthesized respectively in equations 3.7 and 3.8:

$$\mathbf{y_i}(\Phi) = \mathbf{x_0}(\Phi) - r_o(-\sin\Phi, \cos\Phi), \quad \mathbf{y_o}(\Phi) = -\mathbf{x_o}(\Phi) \tag{3.7}$$

$$\mathbf{x_i}(\Phi) = -\mathbf{y_i}(\Phi) + \mathbf{o}, \quad \mathbf{x_o}(\Phi) = \mathbf{x_0}(\Phi + \pi) + \mathbf{o}, \tag{3.8}$$

where $\mathbf{o} = r_o(\cos\theta, \sin\theta)$ is the vector that defines the orbiting motion. Such equations derive from the reflection with respect to the origin of the inner wall of the fixed spiral and of the outer wall of the orbiting spiral. The constant ρ_0 has to assume the value of $-r_o$ to obtain the correct results from the reflection operation.

3.2.1 Numerical evaluation of the scroll curves

The equations (3.5) and (3.6) can be solved analytically for general increments h_i and respective starting angles Φ_{Ai}. The derivative of the curvature radius can be thought of as the sum of a fixed and a variable contribute:

$$\frac{d\boldsymbol{\rho}}{d\Phi} = r_b + \begin{cases} \frac{h_1}{\pi} = 0.0 & \Phi \in [\Phi_s, \Phi_{A1}] \\ \ldots & \\ \frac{h_i}{\pi} & \Phi \in [\Phi_{Ai}, \Phi_{Ai} + 2\pi] \\ \ldots & \\ \frac{h_N}{\pi} & \Phi \in [\Phi_{An}, \Phi_e] \end{cases} \tag{3.9}$$

As a consequence, it is possible to set up a fast numerical evaluation of the position of the spirals, without knowing the increments features a priori. Setting the first increment to a value of 0.0 allows using canonical methods, developed for scrolls with constant thickness, for the definition of the discharge region. The resulting general equations for the evaluation of the coordinates of a point of the reference spiral $\mathbf{x_0}$ are given by:

$$\mathbf{x_0}(\Phi) = (r_b, 0.0) + \rho_0(\sin\Phi, -\cos\Phi) + \mathbf{x_0^{r_b}}(\Phi) + \mathbf{x_0^{I}}(\Phi_{Ai}) + \mathbf{x_0^{II}}(\Phi_{Ai}, \Phi), \tag{3.10}$$

where $\mathbf{x_0^{r_b}}(\Phi)$ is a term related to the basic radius, while $\mathbf{x_0^{I}}(\Phi_A)$ and $\mathbf{x_0^{II}}(\Phi_{Ai}, \Phi)$ are exclusively based on the increments. The complete version of equation (3.10) is reported in Appendix A. However, it is interesting to notice that, from the coding point of view, $\mathbf{x_0^{I}}(\Phi_A)$ can be fully evaluated before performing any kind of calculation to reduce the computational effort. The example of different variable thickness geometries with increasing h is reported in figure 3.6, starting from a constant thickness set-up.

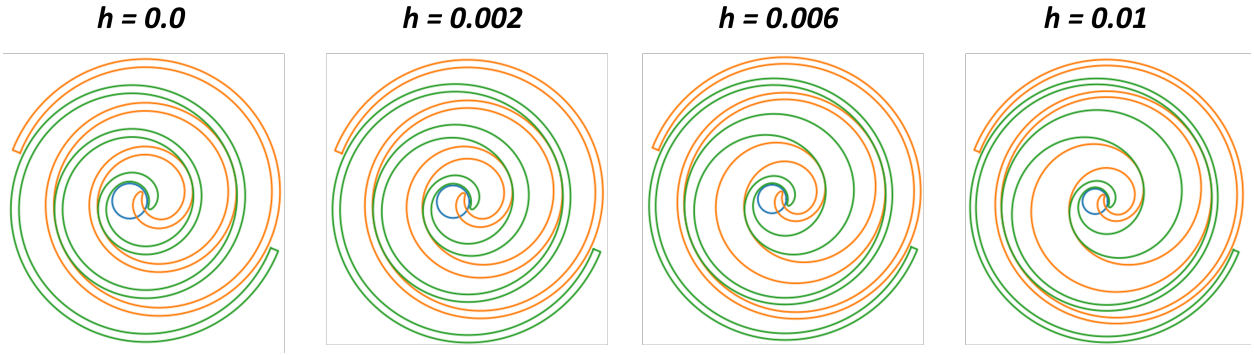

Figure 3.6: Scroll variable thickness geometries.

By re-arranging this formulation in order to match with the PDSim reference of frame, the architecture of the simulation software can be fully exploited. The volumes of the scroll chambers can be evaluated via numerical integration at the start of the simulation, filling arrays of volumes as functions of the orbiting angle. When later needed, the volumes linked to specific orbiting angles can be interpolated to speed-up the calculation. As a consequence, it is not needed to reach a closed-form analytical solution of the volumes of the chambers and this method can be further extended to any kind of variable thickness geometry. The accuracy of the calculation of the volumes, which depends on the size of the arrays mentioned above, has been assessed by comparison with the analytical relations for constant thickness scrolls proposed by Bell et al. [17], showing discrepancies that can safely be considered negligible ($\approx 10^{-5}\%$).

Chapter 4

Numerical tools

The main numerical tools used or developed by the author are presented in this chapter. The first section contains the description of the PDSim code for quasi-static analyses of positive displacement machines. One of the original contributions included in this thesis regards the construction of a variable thickness geometrical module for PDSim. In the remaining parts of the chapter, OpenFOAM and its related novel implementations are treated. In particular, scrollFOAM is employed to simulate scroll compressors, while CoolFOAM is a wrapper used to retrieve the thermophysical properties using the CoolProp library.

4.1 PDSim

PDSim is an open-source set of Python libraries for the quasi-static simulation of positive displacement machines. The code is based on a *0-D* model (or chamber model) constituted by control volumes, flow functions and loss functions. The thermophysical properties needed during the simulations are calculated by means of direct calls to the open-source thermophysical library CoolProp [20]. The main structure of PDSim is illustrated in the first part of this section, followed by the description of the original implementation performed by the author to include variable thickness scroll geometries.

Positive displacement machines are schematized using control volumes connected by flow functions. The scheme of a control volume is represented in figure 4.1.

A control volume represents a region of the geometry of the machine that may experience a volume contraction or expansion. A non-zero value of the derivative of the volume of a working chamber produces a compression or expansion process. The flow models connect the control volumes allowing a mass flow according to the pressure difference between the two regions. There are a number of assumptions associated with the definition of control volume in PDSim:

- Gravitational effects and kinetic energy changes are neglected.

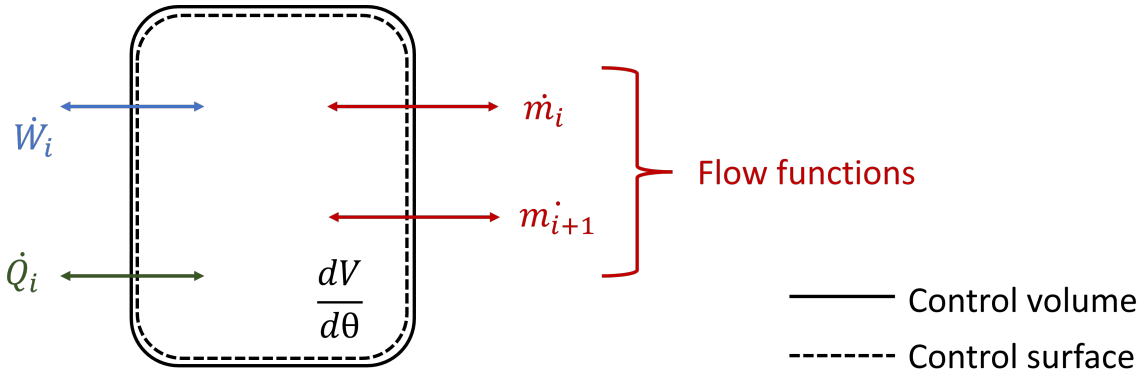

Figure 4.1: PDSim control volume.

- Pressure and temperature are considered uniform throughout a control volume.
- Control volumes can exchange heat and mass flow between each other.

Since the independent variables of the Helmholtz energy formulation included in CoolProp are temperature and density, the same variables are taken as independent in PDSim. The code is based on two *0-D* conservation equations: the conservation of mass and the conservation of energy.

The conservation of mass can be expressed both in the time domain and in the crank-angle domain, as reported in equations 4.1 and 4.2, respectively.

$$\frac{dm}{dt} = \sum_i \dot{m}_i \tag{4.1}$$

$$\frac{dm}{d\theta} = \frac{1}{\omega} \sum_i \dot{m}_i \tag{4.2}$$

Similarly, the conservation of energy is given by:

$$\frac{dU}{dt} = \dot{Q} + \dot{W} + \sum_i \dot{m}_i h_i \tag{4.3}$$

Where $\dot{W}$ is the boundary work term, $\dot{Q}$ is the heat flowing into the control volume and $\sum_i \dot{m}_i h_i$ is the sum of the enthalpy flow terms. Equation 4.3 can be expanded to consider the temperature as the independent variable in the crank-angle domain:

$$\frac{dT}{d\theta} = \frac{-T\frac{\partial p}{\partial T} + \left[\frac{dV}{d\theta} - \frac{1}{\rho}\frac{dm}{d\theta}\right] - h\frac{dm}{d\theta} + \frac{\dot{Q}}{\omega} + \frac{1}{\omega}\sum_i \dot{m}_i h_i}{mc_v} \tag{4.4}$$

The system is closed using direct calls to CoolProp, which provides different equations of state for real and ideal fluids. The CoolProp theoretical formulation are extensively treated in section 4.3.

In case of multi-phase flow, where $x_{l,f}$ is the oil mass fraction of the flow path f, a third conservation equation is added to the system. Moreover, the energy conservation equation is extended to consider the oil mass fraction. The resulting system, where $(u_l - u_g)$ is the specific internal energy variation, is reported below:

$$\frac{dm}{d\theta} = \frac{1}{\omega}\sum_i \dot{m}_i \tag{4.5}$$

$$\frac{dx_l}{d\theta} = \frac{1}{m}\left[\frac{1}{\omega}\sum_f \dot{m}x_{l,f} - x_l\frac{dm}{d\theta}\right] \tag{4.6}$$

$$\frac{dT}{d\theta} = \frac{-T\frac{\partial p}{\partial T} + \left[\frac{dV}{d\theta} - \frac{1}{\rho}\frac{dm}{d\theta}\right] - m(u_l - u_g)\frac{dx_l}{d\theta} - h\frac{dm}{d\theta} + \frac{\dot{Q}}{\omega} + \frac{1}{\omega}\sum_i \dot{m}_i h_i}{mc_v} \tag{4.7}$$

The volume terms depend directly on the specific geometry of the machine to analyze. Usually, for scroll geometries, the volumes of the working chambers are determined using analytic relations derived from the equations of the spirals. The leakage flows are calculated in PDSim using the flow model proposed by Bell et al. [18], which considers a compressible flow with frictional effects. Other flow paths, such as the connection between the discharge chamber and the outlet pipe, are treated as compressible isentropic nozzles. More information on the flow models, heat transfer correlations and mechanical losses can be retrieved from [21].

The result of the discretization of the scroll chambers in control volumes is a set of differential equations containing the independent variables and their derivatives. Therefore, a numerical integrator is needed to solve this system of equations:

- The simplest integrator implemented in PDSim is an **Euler integrator**, which calculates the variables at a new time-step according to a linear extrapolation of the derivative at the last calculated time-step. The Euler integrator is characterized by a first-order accuracy.

- The **Heun's integrator** is a predictor-corrector method that predicts the new variables in the same way of the Euler method, but then performs an average of the old and new values increasing the accuracy to the second order.

- Lastly, the **adaptive Runge-Kutta integrator** is an adaptive method able to better solve stiff systems of differential equations [35]. This method is more suitable for complex systems such as scroll compressors. The adaptive nature of this solver allows to find a balance between the error-per-step and the computational effort.

A real machine is subdivided into control volumes, tubes, valves and flow models, building a set of differential equations that are solved for an entire revolution until the convergence is

reached. The first convergence criteria is based on the difference between the solution of the last cycle and the previous one. In addition to that, a system of lumped masses is built to represent the thermal inertia of the system: a steady-state energy balance has to be enforced on this system of lumped masses. Lastly, the eventual presence of reverse flow produces the need of evaluating iteratively the discharge temperature according to a global energy balance including the reverse flow contribute, which depends on the discharge temperature.

4.1.1 Variable thickness scroll modelling in PDSim

It has not been necessary to modify the main structure of PDSim to enable the simulation of variable thickness geometry. Exploiting the object-oriented nature of the code, a new geometrical package, specific to variable thickness scroll compressors, has been created starting from the one developed for constant thickness machines. Mainly, all the operations based on the analytical calculation of volume or spiral points positions has been removed and substituted by numerical integration according to the considerations included in [60].

The built-in constant thickness geometrical package included in PDSim is constituted by a set of Cython [11] modules that are coordinated by a core file that is connected with the other packages of the software. Cython allows to obtain C-like performance writing code with a python structure. The key of the implementation presented in this work is the modification of the **geoVals** class, included in the common_scroll Cython module. An object of the **geoVals** class is instantiated at the beginning of a new simulation, providing the values of chamber volumes and surfaces throughout the whole simulation process. Originally, this class calculates the required property by calling a series of sub-routines based on analytical formulations, which are easy to derive for constant thickness geometries [17].

The current implementation is based on the replacement of the analytical methods with a spline-interpolation system, as schematized in figure 4.2.

The numerical integration for the evaluation of forces and volumes is performed only once in the initialization stage. The obtained data are used to create a spline interpolator that is stored in a C++ map (using Cython). During the simulation the interpolator provides the required properties to the solver until a satisfying convergence is reached. This approach allows major computational time saving with respect to on-the-fly calculation and the error due to interpolation has proven to be negligible.

Some of the operations that require the employment of this interpolation structure are summarized below:

- **Volumes of the scroll chambers:** The volumes of the scroll chambers are calculated before the actual simulation for a pre-defined number of orbiting positions. Spline interpolation is then employed to calculate the required volume and its derivative at the required orbiting angle.

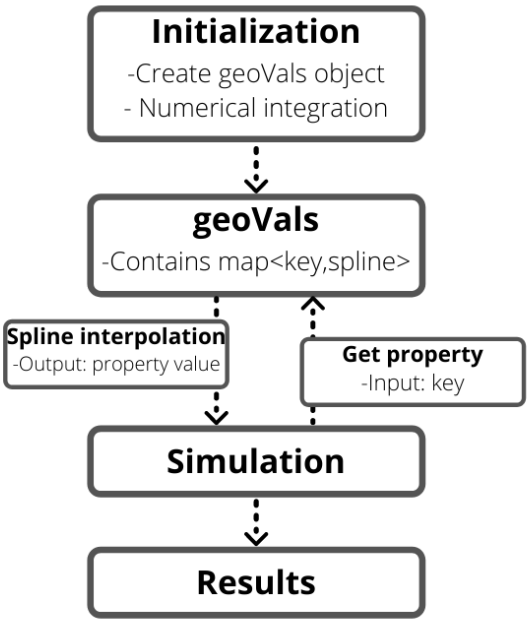

Figure 4.2: Flowchart of the interpolation process.

- **Forces of the scroll chambers:** The forces acting on the walls of the working chambers can be evaluated if the area of these boundaries is known. Consequently, numerical integration of the arc length of the spiral is performed before the simulation. The value of the arc length corresponding to the chamber boundary is then interpolated and multiplied by the corresponding scroll width to retrieve the surface area and, consequently, the force.
- **Scroll thickness:** The thickness of the scroll wraps has to be determined to perform heat transfer calculation and to evaluate the length of the paths of the radial leakages.

4.2 OpenFOAM

OpenFOAM is the most widely used *CFD* open-source software for continuum mechanics problems. Naturally, it is a free license code, and the extensive use worldwide is a guarantee for the reliability and the accuracy of the results. This C++ toolbox is constantly improved by several developers according to the open-source mentality. Furthermore, if a user has the ability to do so, he can develop new software features autonomously through additional coding. In this section, OpenFOAM is described briefly to allow the reader to better understand the original libraries developed in this thesis. The basics of *CFD* theory are not included in this manuscript for the sake of brevity, but a complete description of the theoretical basis can be retrieved from [63, 76, 117].

4.2.1 History

OpenFOAM was released as an open-source code in 2004, after the attempt by Henry Weller and Hrvoje Jasak to commercialize the original software FOAM in the late 90's, early 00's [174]. Subsequently, a society called OpenCFD Ltd was founded by Henry Weller, Chris Greenshields and Mattijs Janssens to address the activities of development and release of OpenFOAM. Simultaneously, Hrvoje Jasak started Wikki Ltd [3], a consulting company, and maintained a variant of OpenFOAM named foam-extend.

In 2012 OpenCFD Ltd was acquired by ESI group, but in 2014 Weller and Greenshields left OpenCFD and founded CFD Direct Ltd to handle the maintenance of a new variant of the software: OpenFOAM Foundation Ltd.

The chronological and common development of the main three variants of *OpenFOAM* software is summarized below:

- The *OpenFOAM* variant mainly developed and maintained by OpenCFD Ltd. (a company held by ESI Group since 2012) with a date-of-release identifier (e.g. v1906) (from 2004).
- The FOAM-Extend Project variant has been mainly maintained by Wikki Ltd. (from 2009).
- The OpenFOAM-Foundation variant has been mainly maintained by CFD Direct Ltd. sequence based identifier (e.g. 6.0) (from 2011).

The majority of the developments presented in this thesis derive from the *OpenFOAM* variant [2], which has been deeply employed by major private companies and research institutions. Some examples are Audi, Volkswagen, Man, Imperial College London, Chalmers University and many others.

4.2.2 User effort and software limitations

Performing a *CFD* analysis with *OpenFOAM* involves different challenges, starting from the case setup: the lack of an interface for pre-processing operations requires many user skills. Despite some graphical interfaces for pre-processing have been developed, such as the open-source HELYX [1], the operation of directly editing the dictionaries is necessary to fully exploit the software capabilities. The consequence of this need is a steep learning curve: the training time is consistently higher than commercial software's one. A description of the basic features of the *OpenFOAM* framework has been included in Appendix A.

Realizing a good mesh is one of the milestones of the work, and it is not trivial to configure the built-in mesh generators. It is strongly advised to verify the quality of the mesh with

the **checkMesh** utility before proceeding with further operations. Working with this code, it is absolutely essential to have a wide knowledge of the physics of the problem.

Apart from the difficulties inherent to almost every *OpenFOAM* case, the determination of thermophysical properties is particularly important when dealing with real gases. The built-in modelling options are the following:

- **Equations of state**: density can be calculated using the Peng-Robinson equation or with a polynomial model, determined with constant pressure and the temperature as the independent variable. Peng-Robinson is quite accurate in various conditions but for saturated liquids and conditions close to the critical point the error increase [168]. The polynomial models inherently suffer high-pressure differences and phase change, as well as density trends difficult to shape.

- **Thermodynamic properties**: the specific heat, from which other properties are derived, is calculated as a temperature function for real gases. It is possible to adopt a model with user defined polynomials or based on the JANAF tables of thermodynamics. Both these model can incur into the same difficulties described above for the density.

- **Transport properties**: for the transport properties (viscosity, thermal conductivity and thermal diffusivity), polynomial models and the Sutherland model are available. These models share the drawbacks with the interpolating methods described in the previous points.

CoolFOAM, a new wrapper between the CoolProp library for the determination of thermophysical properties and *OpenFOAM* is described in section 4.3. This implementation has been performed to enhance the accuracy and the user-friendliness of the process of calculation of thermophysical properties in *OpenFOAM* simulations.

4.3 CoolFOAM

The need for an extension of the *OpenFOAM* capabilities in modelling the thermophysical properties has been satisfied with the possibility of obtaining directly the required values from the CoolProp library. A C++ shared library has been written, starting from the *OpenFOAM* templates. The library has been developed to facilitate its use in a similar fashion with two of the *OpenFOAM* solvers, **rhoPimpleFoam** and **rhoSimpleFoam**, which are one transient and one steady-state solver for compressible flow cases, respectively. Alternatively, other solvers within *OpenFOAM* have to be slightly modified to adapt them to the new thermophysical properties package. The conformity of the library to the *OpenFOAM* coding standards allows easy adoption of the new features in a wide series of cases. Once the new

library and applications are compiled, the user only needs to add the correct textual inputs in a configuration file to use the CoolProp library.

4.3.1 Theory

OpenFOAM thermophysical models

The computation of thermophysical properties in an *OpenFOAM* simulation is based on a pressure-temperature system. These variables are the independent variables, from which other properties are determined. Frequently, the user has to evaluate thermophysical properties in applications where the ideal gas approximation is not usable with reasonable accuracy. In such cases, the most accurate model available for the evaluation of the fluid density is the Peng-Robinson equation of state:

$$p = \frac{RT}{\nu - b} - \frac{a_c \alpha(T_{red}, \Omega)}{\nu(\nu + b) + b(\nu - b)} \tag{4.8}$$

with the parameters:

$$a_c = 0.45724 \left(\frac{R^2 T_C^2}{P_C} \right)$$

$$b = 0.07780 \left(\frac{RT_C}{P_C} \right)$$

$$\alpha(T_{red}, \Omega) = \left[1 + m(\Omega) \left(1 - \sqrt{T_{red}} \right) \right]^2$$

$$m(\Omega) = 0.37464 + 1.54226\Omega - 0.26992\Omega^2$$

where ν is the molar volume, T_{red} is the reduced temperature, Ω is the acentric factor, R is the gas constant, and T_C and P_C are the critical values of temperature and pressure, respectively. Peng-Robinson is quite accurate in different conditions, but for saturated liquid densities, conditions close to the critical point and caloric properties in the homogeneous region the error increases [94, 167]. Nevertheless, PR and other cubic equations of state are frequently adopted for the evaluation of vapour pressures and equilibrium-phase compositions of mixtures. In such cases, these equations of state need less computational resources than multiparameter equations of state [69], yielding relatively accurate results. In CFD analysis, the computational overhead has to be taken into account, evaluating different fluid property models on a case-by-case basis. Cubic EOS may represent an effective trade-off between accuracy and computational load, as pointed out by Abdelli et al. [4].

It is also possible to adopt a polynomial model, where the density trend is fitted with constant pressure and the temperature as the independent variable. Polynomial functions inherently lack accuracy in the presence of wide pressure ranges and phase change, as well as density trends difficult to shape. Polynomials can be adoptped also for the specific heat

and transport properties (viscosity, thermal conductivity and thermal diffusivity). Thermodynamic properties, which are derived from the specific heat, can be also evaluated from the JANAF tables of thermodynamics [5]. In addition to that, the Sutherland model for the transport properties calculation is available. Again, wide pressure ranges and complex trends of the variables can be significant sources of inaccuracy.

CoolProp thermophysical models

The determination of thermodynamic properties of all the fluids included in the CoolProp library is based on equations of state explicit in the Helmholtz energy. This formulation is a common denominator for all the high-accuracy equations of state currently available in the literature. In this formulation the sum of a residual part (α^r) and of an ideal gas part (α^0) gives the expression for the nondimensionalized Helmholtz-energy:

$$\alpha = \alpha^0 + \alpha^r \tag{4.9}$$

The most fascinating aspect of this model is the fact that all the other thermodynamic properties can be found through analytic derivatives of the two just mentioned terms. As an example, the equation for the pressure is:

$$Z = \frac{p}{\rho RT} = 1 + \delta \left(\frac{\partial \alpha^r}{\partial \delta} \right)_\tau \tag{4.10}$$

where Z is the compressibility factor, p is the pressure, R is the mass-specific gas constant, ρ is the density, T is the temperature, δ is the reduced density given by $\delta = \rho/\rho_{red}$ and the reciprocal reduced temperature is $\tau = T_{red}/T$. Generally, the reducing variables ρ_{red} and T_{red} correspond to the critical values. For some fluids, such as R134a, these reducing parameters have to be determined during the fitting process. The pressure example is followed by several other derivatives, which can be found in scientific articles of authors like Thorade and Sadat [165], Span [151] and Lemmon [100]. The independent variables of the Helmholtz-energy equations are temperature and density. If there is the availability of different state variables, it is necessary to use numerical solvers in order to calculate the independent variables. Various state variables inputs are analyzed in Span [152], and a solver for enthalpy/entropy is included in Coolprop.

For the transport properties, the state of the art is more confused. There is a higher quantity of methods available in the literature for the determination of these properties. It is possible to find high-accuracy methodologies for some fluids, but for others the possibilities are definitely scarce. The viscosity is usually divided into two terms: the first considers the viscosity in relation to temperature in the condition of dilute-gas, while the second includes

the temperature and density-dependent residual viscosity:

$$\eta = \eta^{(0)}(\tau) + \eta^{(r)}(\tau, \delta) \tag{4.11}$$

The critical enhancement of viscosity represents a divergence of transport properties of fluids close to the critical point [143]. Usually, this phenomenon is not taken into account, but for a small number of fluids it is considerable. This is possible if enough information about viscosity in the critical region is provided. In CoolProp the only fluids having this phenomenon modelled are water [80] and carbon dioxide [28]. On the contrary, for the thermal conductivity the critical enhancement term is not negligible in areas distant from the critical point. For this reason, three terms are considered for the thermal conductivity:

$$\lambda = \lambda^{(0)}(\tau) + \lambda^{(r)}(\tau, \delta) + +\lambda^{(c)}(\tau, \delta) \tag{4.12}$$

Some of the fluids included in CoolProp do not have high-accuracy correlations for the transport properties. For these less-studied fluids, it is necessary to find a method that can substitute these correlations: one of the most used choices is the *Extended Corresponding States (ECS)* methodology. It allows for the obtainment of the properties for the fluid of interest starting from a well-known reference fluid: this reference should have a similar p-v-T surface and an accurate estimation of transport properties. The *ECS* method proposed in CoolProp follows the work proposed by Huber et al. [79], which has already been implemented in REFPROP[101].

4.3.2 The CoolProp-OpenFOAM wrapper

OpenFOAM thermophysical classes

OpenFOAM has two main thermophysical model classes for fixed composition fluids: the first is based on density, *rhoThermo*, and the other on compressibility, *psiThermo*. Every solver that needs thermophysical properties constructs an object of one of these classes.

The rhoThermo class is constituted by two source files, *rhoThermo.C* and *rhoThermos.C*, and one header file, *rhoThermo.H*. The header file is included in the related *OpenFOAM* solvers in order to have access to the functions needed to determine the thermodynamic properties. Three main objects are created in this class: the density *rho*, the compressibility *psi* and the dynamic viscosity *mu*. This model calculates the basic thermodynamic properties in relation to the density variation of the fluid. It is applied particularly to heat transfer cases, where changes in temperature imply variations of density. The psiThermo class has basically the same structure as the one described above (*psiThermo.C*, *psiThermos.C* and *psiThermo.H*). The main difference is related to the density definition: this model is based

on compressibility, which gives the density if multiplied by pressure. Moreover, there is a *fluidThermo* model which makes it possible to choose the thermophysical models at runtime. The objects of this class are currently constructed only by the **rhoSimpleFoam** and **rhoPimpleFoam** solvers.

The CoolProp library

More than one hundred equations of state and transport properties correlations for pure and pseudo-pure fluids are stored in the C++ CoolProp library. Moreover, this library implements mixtures, incompressible fluids and brines properties, high accuracy psychrometric routines and cubic equations of state. The code is based on an abstract base class (*AbstractState*) which delineates a protocol that must be implemented by the property backends. It is possible to have access to the fluid properties through two different interfaces of CoolProp:

- The high-level interface allows for the obtainment of the required fluid property with a simple call to the **PropsSI** function. As an example, the line of code for specific heat at constant pressure ("C") of R134a at temperature ("T") and pressure ("P") of respectively 273.15 K and 2 MPa is:

```
Cp = PropsSI('C','T',273.15,'P',2e06,'R134a')
```

- The low-level interface provides access to deeper levels of the CoolProp code. This solution is definitely faster: actually, the low-level interface is always internally called by the high-level one. The low-level interface operates with enumerated values and floating-point numbers, avoiding the usage of strings. This obviously increases the efficiency and speeds up the execution. In order to maximize the efficiency of the low-level interface, it is necessary to instantiate an instance of the backend for each fluid, calling then methods within the instance. Calling the constructor for the backend instance is not computationally insignificant, so it is better to only do it one time.

The CoolFOAM library

The main contribution of this work is a new C++ shared library for the determination of thermophysical properties in OpenFOAM: **libCoolPropThermophysical.so**. It contains two new thermophysical model classes for fixed composition fluids, *psiThermoCool* and *rhoThermoCool*. These new classes are very similar to the OpenFOAM's original ones, described in section 4.2. The main difference is the inclusion of three new classes, the first containing the new equation of state, the second for the thermodynamic properties and the last one for the transport properties.

The *rhoCoolProp* class allows the evaluation of the fluid density directly from the CoolProp library: firstly, a shared pointer *rhoFluid* to a new-allocated instance of one of the

AbstractState backends is instantiated. The density value is returned by an appropriate member function, which updates initially the pressure and the temperature of the instance, and then calculates the requested property.

Thermodynamic and transport properties are evaluated respectively as objects of the *hCoolProp* and *CoolPropTransport* classes. The basic principle of these classes is the same as the *rhoCoolProp* class, described above.

For what concerns the numerical simulations of two-phase flows, *OpenFOAM* handles the thermophysical properties of the two phases separately. For this reason, the calculation of such properties inside the saturation dome has not been implemented in the CoolFOAM library.

4.3.3 Compiling and using the library

The compilation of the CoolFOAM library does not require additional operations than the ones required for *OpenFOAM* standard libraries. The only action required is to build the CoolProp database as a shared library, in order to be able to link it with *OpenFOAM*. In order to correctly perform the compilation, it is necessary to include the CoolProp shared library and all the directories related to it. Detailed instructions for the installation of the product of this work are included in a text file attached to the library itself, which is available upon request. The first version of the present work has been developed for OpenFOAM 6, but it is constantly adapted to the most recent versions of the software.

In order to use the wrapper, the new thermophysical models have to be added to *OpenFOAM* solvers. It is necessary to compile the new applications including the new library, with opportune and simple modifications to some files. More precisely, it is necessary to replace the references to the original classes (e.g., *rhoThermo*, *psiThermo*) with the references to the new ones (*rhoThermoCool* and *psiThermoCool*). Only the solvers with the generalized *fluidThermo* class (**rhoPimpleFoam** and **rhoSimpleFoam**) can work as they are. In this case, it is only necessary to include the correct thermophysical library in the *controlDict*, a setup file required in every *OpenFOAM* case.

The CoolFOAM library definitely enhances the user-friendliness of *OpenFOAM* during the set-up of the thermophysical models. The only action needed is the specification of the fluid name and of the equation of state, checking the CoolProp database to select between the different possibilities, according to the library terminology. A small portion of the thermophysicalProperties dictionary, which is the setup file for thermophysical properties in an *OpenFOAM* case, is reported in listing 1.

The original *OpenFOAM* models, such as the polynomials or the Peng-Robinson equation, require several coefficients that have to be fitted from curves or sourced in the literature, and then inserted in the dictionary. Furthermore, the PR equation implemented in Open-

Listing 1 thermophysicalProperties

```
thermoType
{
type                                    hePsiThermo;
mixture                                 pureMixture;
transport                               CoolProp;
thermo                                  hCoolProp;
equationOfState                         rhoCoolProp;
specie                                  specie;
energy                                  sensibleEnthalpy;
}

mixture
{
    equationOfState
    {
        Fluid                           "R134a";
        EOS                             "HEOS";
    }

    specie
    {
        nMoles                          1;
        molWeight                       102.03;
    }

    thermodynamics
    {
        Fluid                           "R134a";
        EOS                             "HEOS";
        Hf                              0;
        Sf                              0;
    }

    equationOfState
    {
        Fluid                           "R134a";
        EOS                             "HEOS";
    }
}
```

FOAM is not able to calculate the density for liquids.

4.3.4 CoolFOAM performance analysis

Tabular interpolation

A single call to the CoolProp library for the evaluation of density requires a time approximately twenty times bigger than the Peng-Robinson native implementation. The polynomial models calculate the density values five times faster if compared to Peng-Robinson. When running simulations, the physical duration of a computational time step using the CoolFOAM library is increased from 500% to 1500% with respect to polynomial models. The variability of the duration is related to the solver employed. The results presented in this section are relative to the low-level interface of CoolProp. Tests with the high-level interface have shown a computational effort 10-30 times higher. Therefore, the first approach has been implemented in CoolFOAM.

Additionally, the wrapper has been structured to ensure the compatibility of CoolFOAM with the CoolProp tabular interpolation feature. The author has implemented the wrapper to include the possibility of evaluating thermophysical properties by means of the lookup tables implemented in CoolProp. As a result, the user can benefit from a much faster calculation of the properties if compared to the direct calls to the library. The tabular interpolation can be performed by means of two methods: the *Tabular Taylor Series Extrapolation (TTSE)* and the bicubic interpolation.

The *TTSE* consists of a two-dimensional Taylor Series expansion around a selected data point. It can be expressed as follows:

$$z = z_{ij} + \Delta x \left(\frac{\partial z}{\partial x}\right)_{y,ij} + \Delta y \left(\frac{\partial z}{\partial y}\right)_{x,ij} + (\Delta x)^2 \left(\frac{\partial^2 z}{\partial^2 x}\right)_{y,ij} + \\ +(\Delta y)^2 \left(\frac{\partial^2 z}{\partial^2 y}\right)_{x,ij} + \frac{1}{2}\Delta x \Delta y \left(\frac{\partial^2 z}{\partial x \partial y}\right)_{ij} \tag{4.13}$$

Where z is the property of interest, x and y are the independent variables, $\Delta x = x - x_i$ and $\Delta y = y - y_i$. The interval bisection is used to find the nearest node to the set of inputs given, being faster than a direct lookup. The bisection is faster when the inputs are spaced logarithmically: there is a computational overhead related to the use of transcendental functions. If the interval bisection finds a node inside the two-phase region, this node is translated back to the single-phase area.

The *TTSE* causes some discontinuities in the output values, which can be avoided by using the bicubic interpolation (Eq. (4.14)), which produces a smoother surface over the considered range.

$$z = \sum_{i=0}^{3} \sum_{j=0}^{3} a_{ij} x_n^i y_n^j \tag{4.14}$$

The a_ij in the equation (4.14) stand for the coefficients, which are determined when the table is initialized. x_n and y_n represent the normalized variables for the grid cell. Generally, this method is approximately 10% slower than *TTSE*.

Accuracy and computational effort

Methodology This section contains a comparison of accuracy and computational time related to the density evaluation of R1234yf, which is one of the most indicated replacements for the refrigerant R134a [161]. The analysis has been carried out in a pressure range from 1 bar to 20 bar and in a temperature range from 220 K to 440 K. For each pair of PT inputs, a single calculation of the density has been carried out with four different thermophysical models. The result has been compared with the one obtained with the reference *EOS*, which is the Helmholtz energy formulation included in CoolProp. The four alternatives tested are the Bicubic interpolation, the *TTSE* interpolation, the Peng-Robinson *EOS* implemented in *OpenFOAM* and the ideal gas model. The accuracy difference has been evaluated as follows:

$$Error\ in\ density = \left| \frac{\rho_{model}}{\rho_{HEOS}} - 1 \right| \tag{4.15}$$

Where ρ is the density and $HEOS$ stands for Helmholtz Equation Of State. Similarly, the computational time difference has been evaluated as reported in equation 4.16:

$$Computational\ time\ difference = \frac{Time_{HEOS}}{Time_{model}} - 1 \tag{4.16}$$

The results have been plotted on a pressure-enthalpy diagram in order to visualize the most critical areas.

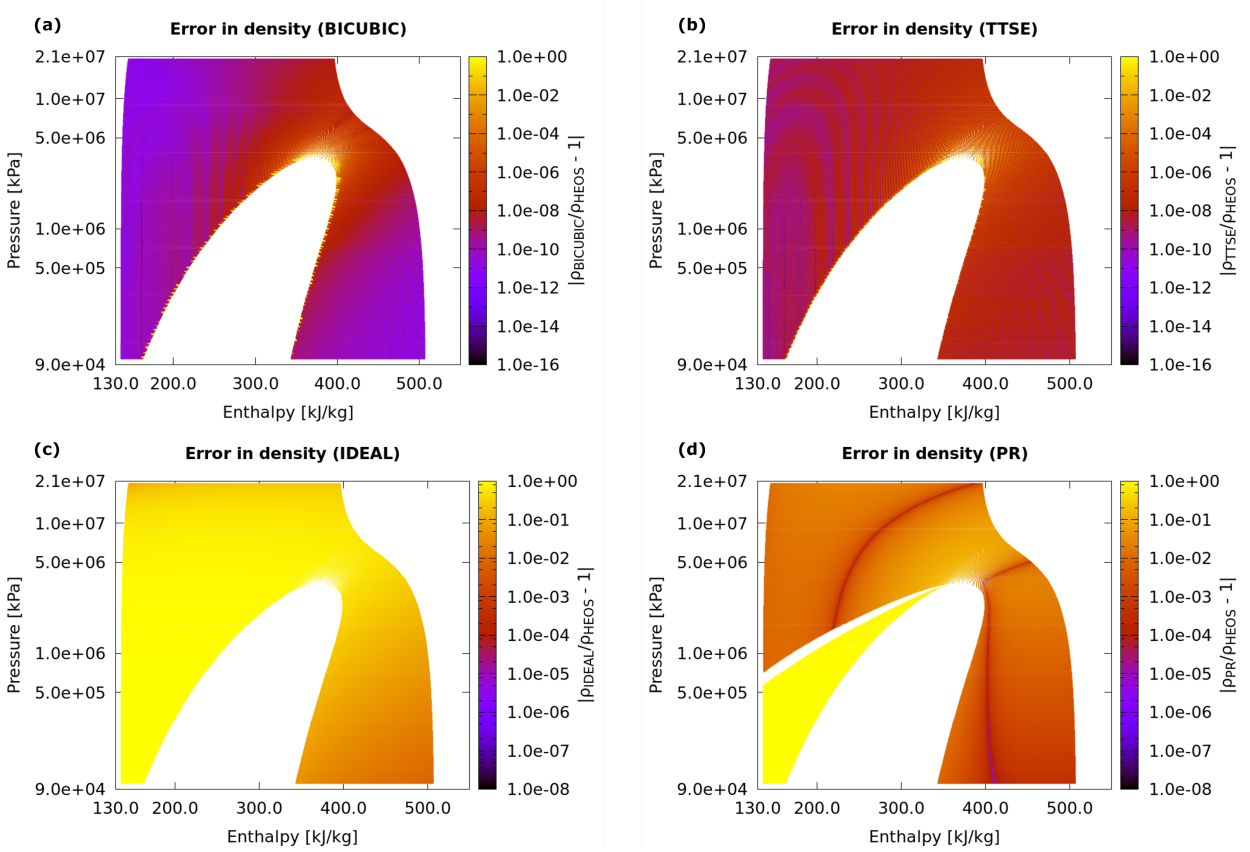

Figure 4.3: CoolFOAM: accuracy difference for R1234yf

Results The accuracy of the two interpolation methods implemented in CoolProp is represented in Figures 4.3(a) and 4.3(b). It can be noticed that the bicubic interpolation yields a better representation of the liquid region and of the ideal gas region if compared to the *TTSE* method. The error in the critical region is comparable between the two interpolation methods. However, the bicubic interpolation appears to be worst when the inputs are close to the saturation line, as a consequence of interpolation errors. The general level of accuracy of these two methodologies is definitely acceptable, but the critical region and the zones close to the saturation line require special attention: it could be necessary to use the direct calls to the *Helmoltz Equation Of State (HEOS)* to have satisfactory results. For what concerns the computational time (Figure 4.4(a) and 4.4(b)), a single call to the interpolation methods ranges from 5 times to 25 times faster than a *HEOS* direct call. In particular, the super-critical area is particularly detrimental for computational efficiency. However, it can be observed that the interpolation tables maintain good performance in that region.

The ideal gas model (Figure 4.3(c) and 4.4(c)) is extremely faster than the *HEOS*, but the accuracy results for the majority of the pressure-enthalpy inputs are not satisfactory. It is strongly advised to adopt other models, with the exception of the bottom-right area of the diagram, where the relative error in density is still around 0.05.

The Peng-Robinson *EOS* (Figure 4.3(d) and 4.4(d)) is approximately two times faster

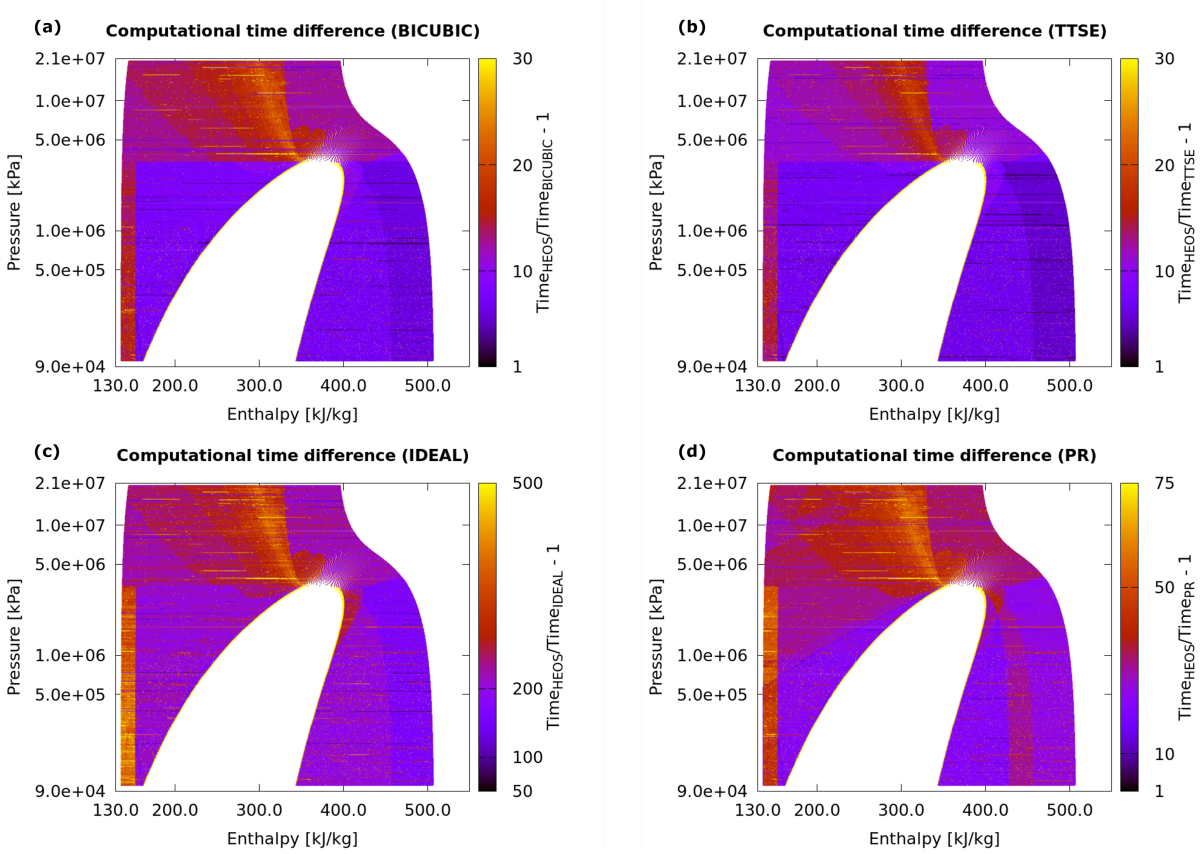

Figure 4.4: CoolFOAM: computational time difference for R1234yf

than the tabular interpolation proposed in the CoolFOAM library. However, it can be noticed that the average relative error is close to 0.01, which is at least 1000 times larger than the interpolation table one. Furthermore, the OpenFOAM implementation of Peng-Robinson shows some limitations in the liquid region: there is an area at low pressures with completely wrong values. Additionally, the white region outside the saturation dome represents a set of inputs that the model is not able to process, leading to a fatal error.

4.4 ScrollFOAM

In this thesis, all the *CFD* simulations related to scroll machines have been performed within the OpenFOAM-v2006 framework. The numerical analysis of scroll machines has been possible thanks to the availability of a compressible flow solver (**rhoPimpleFOAM**), accompanied by built-in implementations of *Arbitrarily Coupled Mesh Interfaces (ACMIs)* [62] and dynamic mesh treatment.

The author [58], as already mentioned in the introduction, has extended the capabilities of the software developing a series of new libraries. Mainly, the first library allows to generate structured meshes for scroll-type machines, while the second supports moving mesh simulations based on user-defined nodal displacements. These methodologies, combined with

the native OpenFOAM mesh generator *snappyHexMesh*, have been consistently employed in this work to create, manipulate and move the computational mesh. The *OpenFOAM* solver adopted by the author is *rhoPimpleFoam*, a pressure-based segregated solver for transient compressible flows.

4.4.1 Deforming geometry and mesh motion

The orbital movement of the rotor leads to a change of the solution domain due to the displacement of the solid boundaries. Consequently, the grid nodes have to move to accommodate such displacement, resulting in the introduction of the relative velocity in the convection terms of the Navier-Stokes equations. As an example, this modification is reported for the integral form governing equation of a general tensorial property, ζ:

$$\frac{d}{dt}\int_V \rho\zeta \, dV + \int_S \rho\zeta(\mathbf{u} - \mathbf{u}_S)\cdot\mathbf{n} \, dS - \int_S \Gamma\nabla\zeta\cdot\mathbf{n} \, dS = \int_V q_\zeta \, dV \tag{4.17}$$

where V is an arbitrary moving volume, S is the surface bounding V, ρ is the density, $\mathbf{n}$ is the outward pointing unit normal vector, $\mathbf{u}$ is the fluid velocity, $\mathbf{u}_S$ is the velocity of the boundary surface, Γ is the diffusivity and q_ζ is the volume source of ζ. Demirdžić and Perić [48] suggested that in order the mesh deformation to respect continuity, the *Space Conservation Law (SCL)*, which describes the conservation of space in case of moving or deforming cells, should be strictly respected. This law is based on the principle that the sum of volume fluxes through cell faces must correspond to the volume rate of change:

$$\frac{d}{dt}\int_V dV + \int_S \mathbf{u}_S\cdot\mathbf{n} \, dS = 0 \tag{4.18}$$

Ferziger and Perić [63] illustrated one of the most common methods to satisfy the *SCL* and ensure mass conservation, which is also implemented in *OpenFOAM*. This method is based on the calculation of the volumes swept by each cell face over a single time step, which are employed to evaluate the volume fluxes avoiding to explicitly define the grid lines velocities (using these last quantities can easily lead to errors).

In this thesis, the orbiting motion of the mobile scroll is handled using a user-defined nodal displacement technique. This method is based on the generation of a set of structured grids corresponding to a number of angular positions predefined by the user. The nodal positions are stored and serve as guidelines for the mesh nodes during the scroll revolution, with the option of linearly interpolate between successive grids to adopt arbitrary time steps, which are constrained in accordance with a user-defined threshold of *Courant-Friedrichs-Lewy (CFL)* number calculated at the end of every time step.

On the other hand, the key-frame re-meshing method includes a mesh replacement for each time step, leading to possible infringements of the *SCL*, as reported by Rane et al. [137].

Another method that does not involve motion of the mesh, but is suitable for the correct replication of the scroll operation is the Cut-Cell method, as presented in [126]. Such an approach involves the generation of a background Cartesian grid in which the geometry to be investigated is contained. In correspondence of the walls, the mesh is adapted to represent the boundary, and the cells falling into the "solid" part of the scroll are discarded. In the framework of the cut-cell method, the space conservation law is not automatically respected, as reported in [22]. A non-trivial treatment is required to enforce the mass conservation that follows from such volume mismatch.

4.4.2 Meshing strategy

At first, a C++ library compliant with the *OpenFOAM* coding standard has been created to apply the custom predefined mesh generation method to scroll machines. The first step in this method is the realization of a body-fitted structured grid starting from the scroll geometry. This kind of grid is characterized by elements of good quality and well-defined connectivity rules.

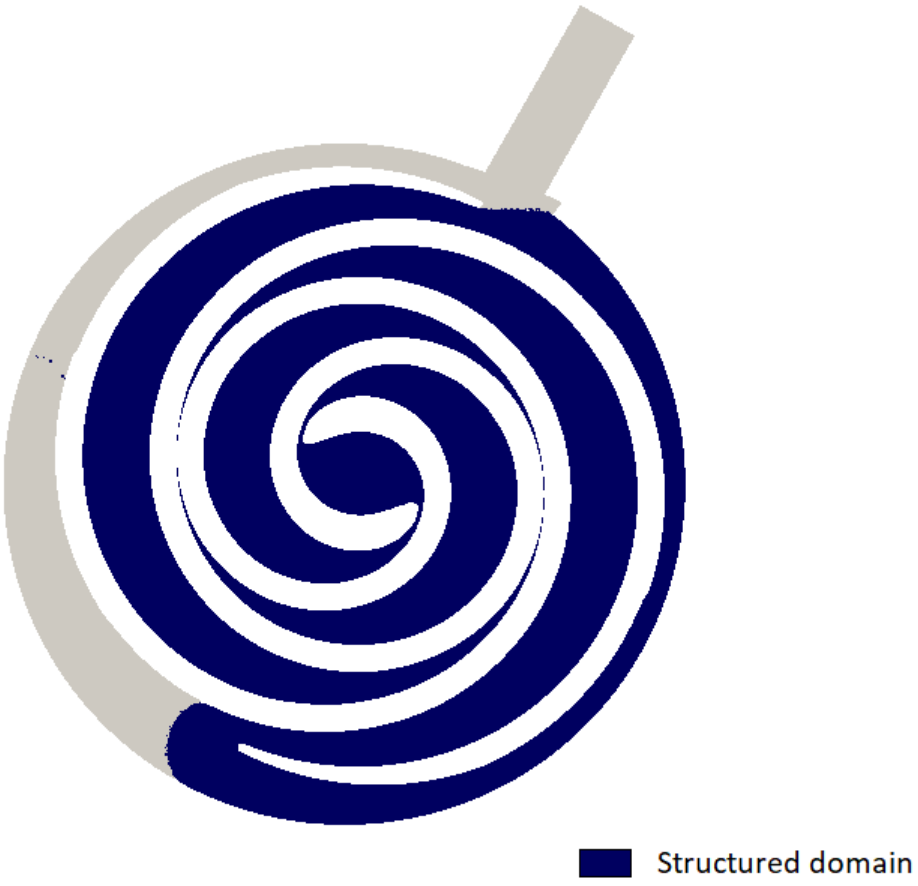

Figure 4.5: Structured domain of the scroll compressor [58]

The generation of a structured mesh of the static parts of the scroll is a task that cannot

be standardized because the geometry of the suction and discharge regions depends on the application and on the constructor choices. Consequently, it has been decided to isolate a portion of the machine that encloses the mobile scroll, as represented in Figure 4.5. Commonly, it is possible to identify a region with such shape in all the scroll machines available on the market. This region has been discretized by means of a structured strategy, while the other parts can be meshed with unstructured algorithms. Then, the connection between the two regions must be performed with one of the interface strategies implemented in *OpenFOAM*.

When the path of the moving parts is known, a set of structured meshes can be generated in advance to describe chronologically sequential positions of the moving bodies. In this case, an increment in time corresponds to an increment of the crank angle, so the user is able to define a number of angular positions of the mobile spiral that have to be meshed. When the actual simulation is executed, the nodes of these predefined grids become control points for the mesh nodes to maintain good element quality. The mesh nodes pass through the control points, but the connectivity remains the same. In this way, both re-meshing and interpolations are avoided during the analysis. One of the advantages of this strategy is that it is respectful of the space conservation law. Moreover, mass and energy imbalances derived from interpolation procedures are not a concern in this case because no interpolation is performed.

Body-Fitted Structured Grid

The generation of the structured grid is performed by the **scrollMesh** utility. The design parameters of the scroll machine are taken as inputs for **scrollMesh**. The portion including the orbiting spiral is subdivided into three blocks: *spiralByAngle*, *symmNose* and *squeezeBox*. The spiralByAngle block is referred to a portion of the domain placed between the orbiting and fixed spiral: it is characterized by a regular path and includes the flank gaps of the machine. On the other hand, the *symmNose* block is placed in the central area of the compressor, where the process of placing the boundary points of the structured grid is more challenging. Finally, the *squeezeBox* block is placed at the end of the orbiting spiral and it is used to connect two different *spiralByAngle* blocks, closing the domain. Alternatively, a rounded geometry can be used connecting directly two *spiralByAngle* blocks (see section 5.2.5).

Considering the mesh as a whole, the first task of the structured mesh generation process is the definition of the nodes at the boundaries and of the nodes connecting the different blocks, followed by the elliptic internal mesh generation. The positioning of the boundary nodes depends on the different meshing strategies characterizing the three blocks strategies and are treated more in detail in section 4.4.4. The elliptic internal mesh generation is

described in the next paragraph.

Elliptic Internal Mesh Generation

The second step is an elliptic mesh generation, characterized by a control map that imposes the orthogonality of the grid at the boundary. This method has been developed according to the work presented by Spekreijse [154]. This meshing strategy is characterized by a transformation from a computational space (ξ,η) to the cartesian domain (x,y), passing through a parameter space (s,t), as represented in Figure 4.6.

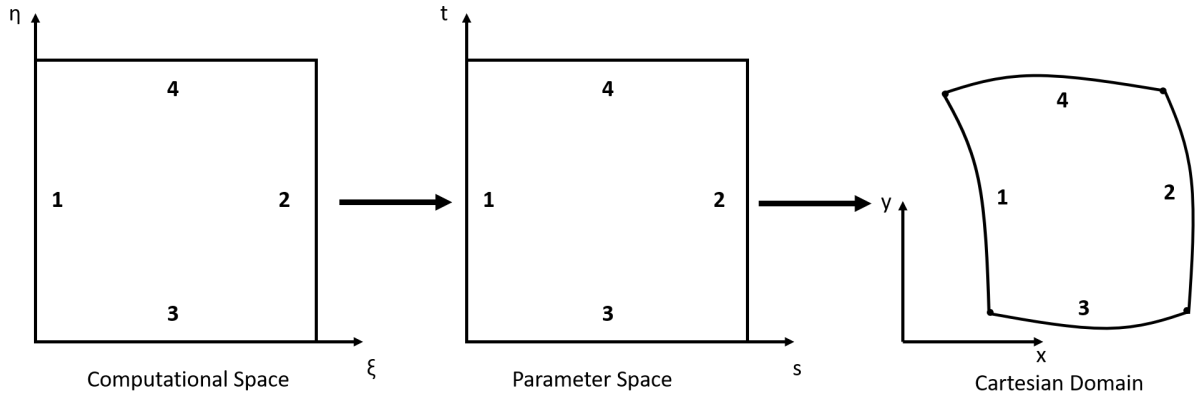

Figure 4.6: Transformation from computational space to cartesian domain. Adapted from [154].

The Picard iteration method with a finite difference discretization has been applied for the solution of a system of nonlinear elliptic equations, reported below:

$$P^{k-1}x^k_{\xi\xi} + 2Q^{k-1}x^k_{\xi\eta} + R^{k-1}x^k_{\eta\eta} + S^{k-1}x^k_{\xi} + T^{k-1}x^k_{\eta} = 0$$

Where x represents the position vector and the subscripts ξ and η represent a derivative in function of the variables of the computational space. The apexes k and *k-1* refer to the current and previous iteration of the Picard method, respectively. In this system of equations, the coefficients P, Q, and R can be calculated using the derivatives of the position vectors at the previous iteration in the function of the computational space variables. On the contrary, in order to evaluate S and T, the derivative of the position vectors relative to the parameter space variables are needed. The variables of the parameter space are calculated by means of the following Laplace equations:

$$\Delta s(\xi, \eta) = 0$$

$$\Delta t(\xi, \eta) = 0$$

where s and t represent the unknowns of the systems while the orthogonality at the boundary is reached by imposing a Neumann boundary condition at the boundaries of interest. The

Laplace equations have been discretized by means of the finite volume strategy, and the resulting systems have been solved using a *BiConjugate Gradient Stabilized (BiCGSTAB)* method.

The structured mesh is generated in two dimensions and then extruded in order to create a three-dimensional computational grid. During the extrusion process, the axial lengths of the cells are reduced in correspondence of the wall to correctly represent the flow features in the near-wall region. These cells are represented in figure 4.7, where the grading function applied to the edges of the cells in the axial direction can be also observed.

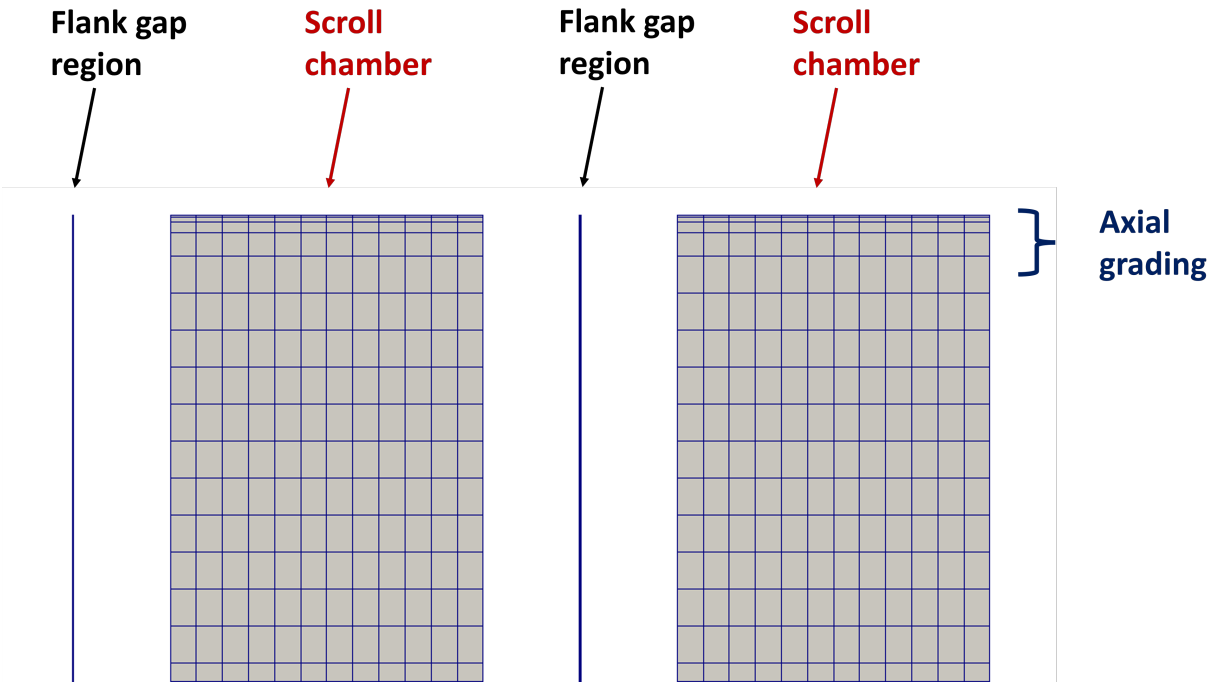

Figure 4.7: ScrollMesh: edge grading in the axial direction.

Moving the Mesh

The first structured mesh is generated for an initial position of the scroll machine. Later, the user has to define a number of grids per revolution that the software must generate, writing the list of control points for the mesh nodes in specific files. A dynamic motion solver, which has been added to the set available in *OpenFOAM*, updates the nodal positions for any user-defined time step, keeping the control points files as reference. In order to evaluate the location of a mesh node for the ith time step, the following equation is solved:

$$x_{i,final} = \alpha * x_{i,AG} + (1 - \alpha) * x_{i,NG}$$

where the subscript AG represents the actual grid file and NG is the next grid file. AG and NG are the files including the nodal positions at the time steps we are interpolating among.

The library that has been developed in this work is, therefore, comprehensive of two

steps: mesh generation (including the actual mesh and the nodal position for a user-defined number of angular steps) and the mesh motion part, which takes care of the evolution of the geometry as the operation of the machine proceeds. The sum of the two goes under the name of the *ScrollFOAM* library and is the only addition to be provided to *OpenFOAM* to enable the simulations of scroll machines (either in compression or expansion configuration) with the above-described approach. The library, as developed, can be fully integrated into *OpenFOAM* and can be employed with native or user-defined libraries (e.g., the CoolFOAM wrapper, section 4.3).

ACMI Interfaces

The structured moving mesh created with *scrollFOAM* has to be associated with the grids of the fixed regions of the machine. Figure 4.8 represents three exploded views of a standard computational domain created using *scrollFOAM* and the *OpenFOAM* built-in meshing utilities (e.g. snappyHexMesh, cfMesh). *ACMIs* [62] are usually employed to connect the fixed and moving regions of the compressor. In particular, these interfaces have been highlighted using different colors in figure 4.8.

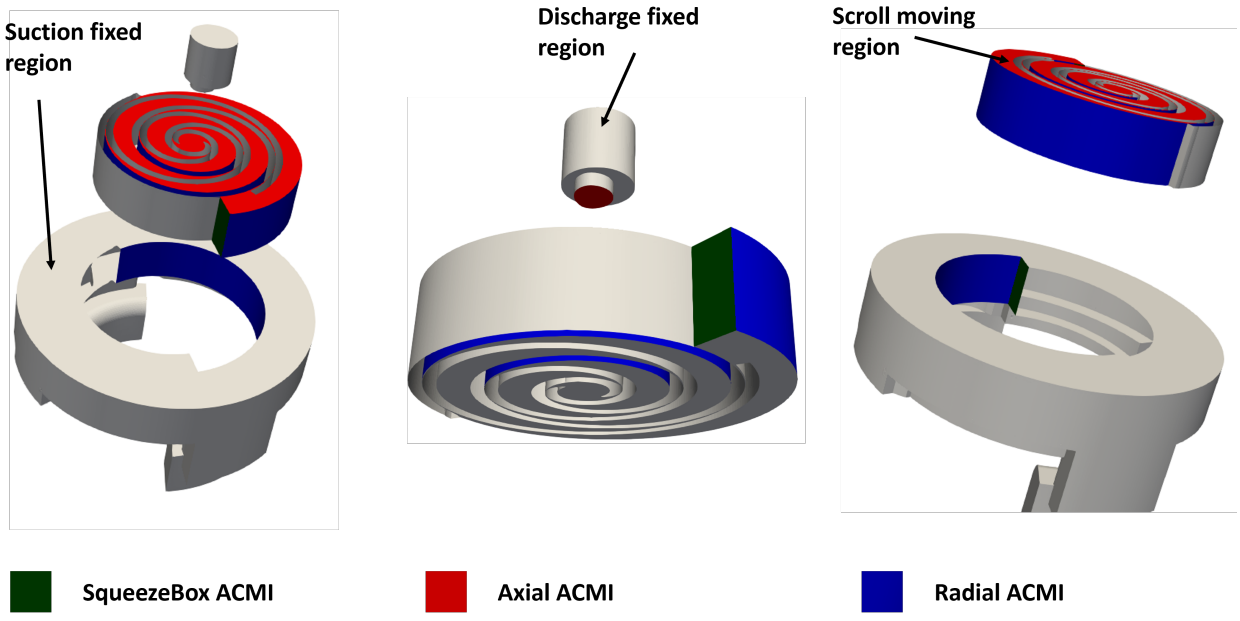

Figure 4.8: scrollFOAM: exploded views of the domain.

4.4.3 Performance indicators

The evaluation of the performance of scroll compressors using *CFD* simulations has been performed focusing on two different indicators.

Retrieving the volumetric efficiency in *OpenFOAM* is quite simple: the actual mass flow rate elaborated by the compressor can be evaluated averaging the mass flow rate at the

inlet/outlet. The average is performed over a complete revolution of the scroll. The resulting value is divided by the theoretical mass flow rate elaborated by the machine, given by the product between the displacement and the inlet density:

$$\eta_v = \frac{\dot{m}_{actual}}{\rho_{inlet} V_{displacement}} \tag{4.19}$$

The pV efficiency, named η_{forces} in this work, is the one calculated from the pressure-volume diagram. In a *CFD* simulation, the power evaluated using the pV diagram corresponds to the one calculated by summing the forces acting on the surfaces of the orbiting scroll. The resultant of these forces in the plane with the axial direction as normal direction is cross-multiplied by the vector representing the orbiting motion. The result, multiplied by the rotational speed, represents the instantaneous power, which is averaged over a revolution to obtain an average value. The isentropic power, which is the product between the theoretical mass flow rate and the isentropic enthalpic jump between inlet and outlet conditions, is divided by the average pV power to obtain the efficiency.

$$\eta_{forces} = \frac{\dot{m}_{theoretical}(h_1 - h_{2s})}{\dot{W}_{forces}} \tag{4.20}$$

4.4.4 The scrollMesh utility

The **scrollMesh** utility is used to create a structured mesh of the scroll domain. The resulting mesh must be coupled with the grids of the static regions (e.g. suction and discharge), which can be realized with standard *OpenFOAM* tools, such as **snappyHexMesh** or **cfMesh**.

scrollMesh can be simply executed from the command line to generate the structured grid. Furthermore, it can be included in auto-run scripts that build the simulation case from scratch. The main input file related to **scrollMesh** is the *scrollDict* dictionary in the *system* directory.

scrollDict

The *scrollDict* dictionary is mainly divided in two sections: the first one contains the geometrical information and the second one includes the meshing parameters. The geometrical section is reported in figure 4.9.

The geometrical section includes the following parameters:

- **zCoordinates**: axial coordinates defining the width of the scroll. *(zMin zMax)* indicate respectively the minimum and maximum value of the scroll domain in the axial direction, which is assumed to be z.

```
// GEOMETRY//
zCoordinates (0 0.016637034857898695);
orbitRadius 0.0035;
clockWise true;

mobileScroll
(
    spiralPW 22.89 3.14 0.0 (0.0 0.0 0.0) 0.0027 (0.0 0.0091 0.0) (0.0 13.47 19.75) 0.0035 2 3e-05
    mobileExtArc 1.573654 -0.496757 0.00846639 0.00347 (-0.00268144 0.00003365 0.0)
    mobileExtArc -3.638349 -1.178442 0.00030029 0.00347 (0.00502564 -0.00414435 0.0)
    spiralPW 0.449 22.89 -1.84 (0.0 0.0 0.0) 0.0027 (0.0 0.0091 0.0) (0.0 13.47 19.75) 0.0035 3 3e-05
);

fixedScroll
(
    spiralPW 20.26 0.449 -1.84 (0.0 0.0 0.0) 0.0027 (0.0 0.0091 0.0) (0.0 13.47 19.75) 0.0035 1 3e-05
    fixedExtArc -1.178442 -3.638349 0.00030029 (0.00502564 -0.00414435 0.0)
    fixedExtArc -0.496757 1.573654 0.00846639 (-0.00268144 0.00003365 0.0)
    spiralPW 3.14 22.89 0.0 (0.0 0.0 0.0) 0.0027 (0.0 0.0091 0.0) (0.0 13.47 19.75) 0.0035 0 3e-05
    fixedExtArc 1.570165 2.199853 0.03 (-0.06468738 0.01742217 0.0)
    fixedSpiral 23.05 26.55 0.0 0.004 (0.0 0.0 0.0)
);
```

Figure 4.9: scrollDict: geometrical section

- **orbitRadius**: the radius of the orbit.
- **clockWise**: indicates the desired direction of revolution. It is used to decide between expander and compression operation.
- **mobileScroll** and **fixedScroll**: list of curves that constitute the two spirals. In particular, the fixed spiral curves start from the outermost curve of the outer wrap and end at the outermost curve of the inner wrap. The mobile spiral curves start from the outermost curve of the inner wrap and end at the outermost curve of the outer wrap.

The type of curves supported by **scrollMesh** are the following:

- **spiralPW** ϕ_s ϕ_e ϕ_0 $(x_{or} y_{or} z_{or})$ r_b $(VT_{increments})$ $(VT_{startAngles})$ r_o *Idx flankGap*

  SpiralPW is a spiral piece-wise curve that includes VT scrolls. A constant thickness geometry can be creating setting all the VT increments to 0.

  Where:

  - ϕ_s is the starting angle (rad).
  - ϕ_e is the ending angle (rad).
  - ϕ_0 is the general involute initial angle (rad).
  - $(x_{or} y_{or} z_{or})$ are the origin coordinates (meters).
  - $(VT_{increments})$ is a list of the desired variable thickness increments.
  - $(VT_{startAngles})$ is a list of the starting angles of the variable thickness sections (rad).

  - r_o is the orbiting radius in meters.
  - *Idx* is the index of the spiralPW (piecewise) curve. In particular:
    * 0: fixed spiral inner wall.
    * 1: fixed spiral outer wall.
    * 2: mobile spiral inner wall.
    * 3: mobile spiral outer wall.
  - *flankGap* is the flank gap size in meters.

- **fixedExtArc** ϕ_s ϕ_e r $(x_c y_c z_c)$

  fixedExtArc is a fixed circular arc. Where:

  - ϕ_s is the starting angle (rad).
  - ϕ_e is the ending angle (rad).
  - r is the arc radius in meters.
  - $(x_c y_c z_c)$ are the centre coordinates (meters).

- **mobileExtArc** ϕ_s ϕ_e r r_o $(x_c y_c z_c)$

  mobileExtArc is a fixed circular arc. Where:

  - ϕ_s is the starting angle (rad).
  - ϕ_e is the ending angle (rad).
  - r is the arc radius in meters.
  - r is the orbit radius in meters.
  - $(x_c y_c z_c)$ are the centre coordinates (meters).

The meshing parameters section is reported in figure 4.10 and contains the following entries:

- **jDiv**: indicates the number of divisions of the structured mesh in the radial direction, which is perpendicular to the flank gap direction (figure 4.11)
- **zDiv**: indicates the number of divisions of the structured mesh in the axial direction.
- **spiralAngleRatio**: determines how much the tangential angle is relevant in the spiral block discretization:
  - spiralAngleRatio = 1 means that the spiral is fully discretized according to the tangent angle development.

```
//MESHING PARAMETERS//


jDiv 12;
zDiv 26;

//SPIRAL
spiralAngleRatio 0.75;
iDivSpiral 950;

//NOSE
noseAngleRatio 0.3;
fixCenterIndexes (2 2 2 2);
fixCenterAngles (0.05 0.6 0.6 0.15);
mobCenterIndexes (1 1 1 1);
mobCenterAngles (0.05 0.6 0.6 0.15);

//SQUEEZEBOX
phiSqueeze 0.001;

scrollMethods
(
    spiralByAngle ($iDivSpiral 12 20) (1 0) (0 0) (22.89 0.8) (false true) 0.75 true
    symmNose (0 1 1 1 1 0) (10 15 40 40 15 10) (0 3) (0.8 0.8) (1 1 2 2) (-1.2 -2.1 -2.1 -1.2)
    spiralByAngle ($iDivSpiral 12 20) (1 1) (3 3) (0.8 22.89) (true true) 0.75 false
    squeezeBox (12 8 30) 0 20.26 5 26.55 0 22.89 3 22.89
);



startAngle 0;
nAngle 360;

function simulation;
```

Figure 4.10: scrollDict: meshing parameters section.

  - spiralAngleRatio = 0 means that the spiral is fully discretized according to the spiral length.

- **iDivSpiral**: indicates the number of divisions of the structured mesh in the tangential direction, which is parallel to the flank gap direction (see figure 4.11). It refers to the main spiral block, which is described below.

- **noseAngleRatio**: analogous to spiralAngleRatio but refers to the nose block.

- **fixCenterIndexes and fixCenterAngles**: these parameters are described in section 4.4.4. The angles are given in radiants, and the indexes refer to the curves list in figure 4.9 starting the count from 0 (0 is the first curve of the fixedScroll list, 1 is the second and so on).

- **mobCenterIndexes and mobCenterAngles**: these parameters are described in section 4.4.4. The angles are given in radiants, and the indexes refer to the curves list in figure 4.9.

- **phiSqueeze**: angular width in rad of the first element of the *squeezeBox* block, see section 4.4.4.

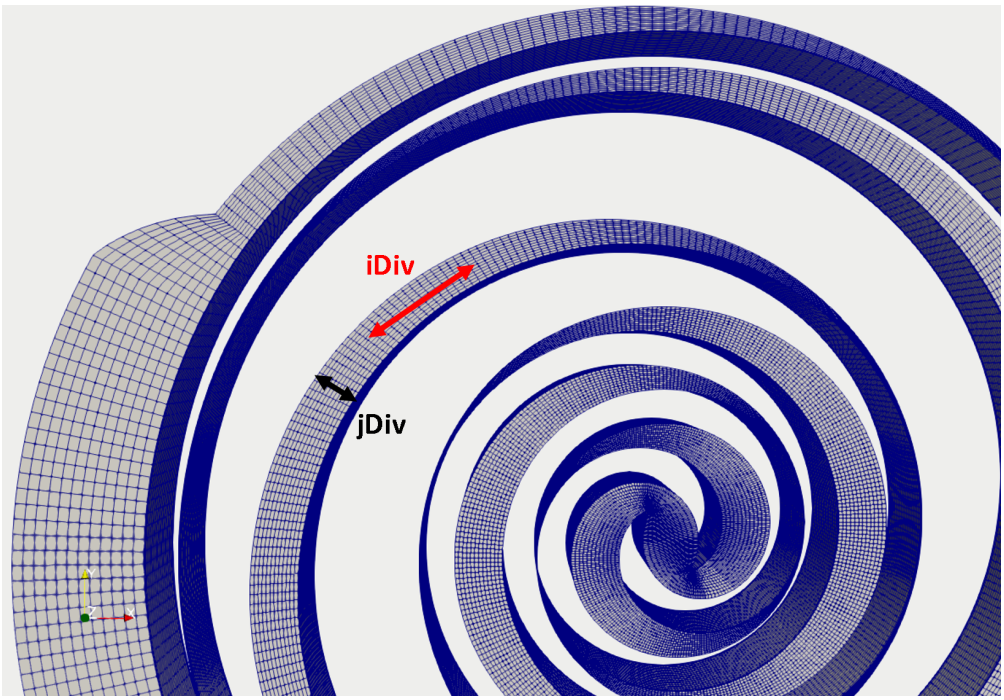

Figure 4.11: scrollDict: mesh divisions

- **scrollMethods**: list of the block meshing methods that constitute the structured mesh. In the example, there is a spiral block, followed by the nose section, another spiral block and at the end the *squeezeBox*. It is important to always have a *spiralByAngle* block as the first element on the list and a *squeezeBox* as the last element (or a *spiralByAngle* if the *squeezeBox* block is not used).
- **startAngle**: orbiting angle in degrees corresponding to the first position that is generated by the utility.
- **nAngle**: number of grids per revolution.
- **function**: test (creates only one grid) or simulation (creates all the grids for the different orbiting angles).

scrollMethods

This section describes the three main block meshing methods implemented in **scrollMesh**.

spiralByAngle This meshing method has been created to discretize a typical spiral-to-spiral block. The user must specify the number of tangential divisions (iDiv), which allow to subdivide the reference spiral (the user has to decide between mobile and fixed reference). The slave spiral is discretized according to lines that connect the points on the reference spiral with the centre of curvature of the reference spiral in that point. These lines can be clearly visualized in figure 4.11 and correspond to the jDiv direction. The points of the

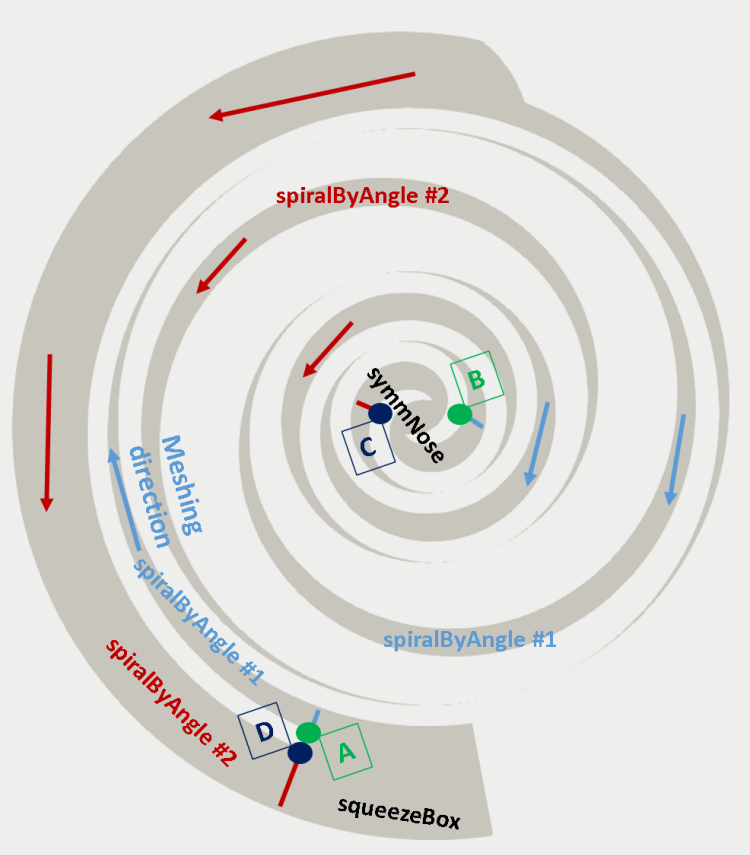

Figure 4.12: scrollMethods: spiralByAngle.

reference spiral are placed according to the **spiralAngleRatio** parameter of the *scrollDict*, which determines a weighting between equally spaced points and equal tangential angle increments between points. Figure 4.12 reports a schematics of this meshing strategy for a case with two *spiralByAngle* blocks connected by a *symmNose* block. The whole structure is closed by a *squeezeBox* block and it is the graphical representation of the *scrollMethods* list included in the dictionary of figure 4.10.

The arrows indicate the meshing direction starting from the first *spiralByAngle* block. Points are indicated by circles and labels, and light blue and red lines indicate the beginning and the end of a *spiralByAngle* block. The *spiralByAngle* block entry in the *scrollMethods* list is:

spiralByAngle $(iDiv\ jDiv\ zDiv)\ (ref_{\mathbf{A}}\ ref_{\mathbf{B}})\ (i_{\mathbf{A}}\ i_{\mathbf{B}})\ (a_{\mathbf{A}}\ a_{\mathbf{B}})\ (isI_{\mathbf{A}} isI_{\mathbf{B}})\ SAR\ fR$

Where:

- $(iDiv\ jDiv\ zDiv)$ are the mesh divisions in tangential, radial and axial directions respectively.
- $(ref_{\mathbf{A}}\ ref_{\mathbf{B}})$ indicates if the points A and B (reference points) are on fixed or mobile spiral (1 = mobile spiral, 0 = fixed spiral).

- $(i_{\mathbf{A}}\ i_{\mathbf{B}})$ are the curve indexes of the points A and B.
- $(a_{\mathbf{A}}\ a_{\mathbf{B}})$ are the curve tangential angles of the points A and B.
- $(isI_{\mathbf{A}} isI_{\mathbf{B}})$ are true if the reference point is internal with respect to the point to which will be connected. In figure 4.12 the A point is external with respect to the opposite point of the first *spiralByAngle* block. On the other hand, the B point is internal.
- SAR is the *spiralAngleRatio*.
- fR is true if the reference spiral is fixed. The radial lines will be drawn with respect to the centres of curvature of the points on the reference spiral. For example, in figure 4.12 the reference spiral for the *spiralByAngle* #1 block is the fixed one.

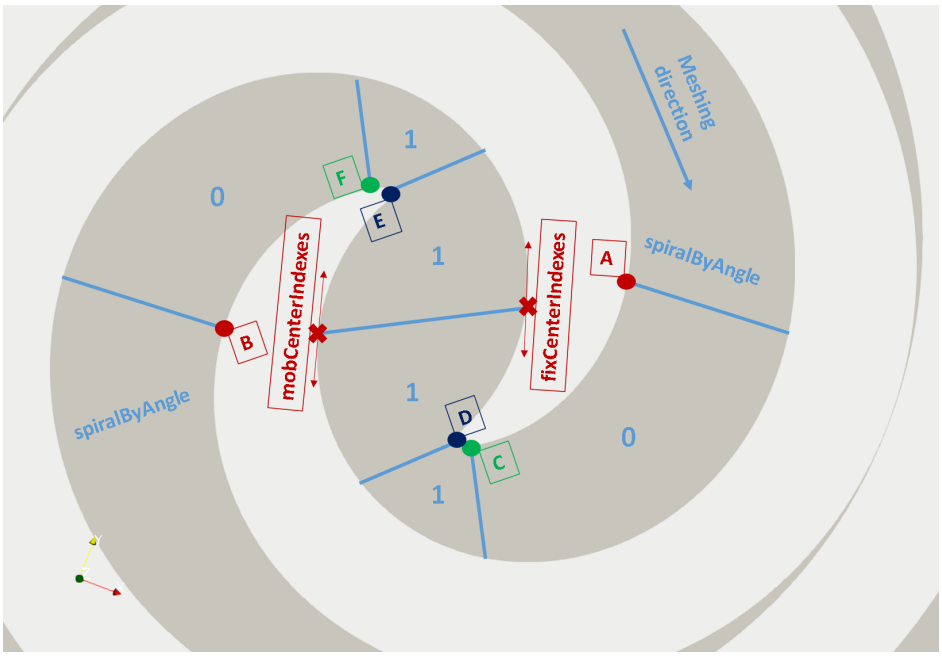

Figure 4.13: scrollMethods: symmNose.

symmNose The arrows indicate the meshing direction starting from the first *spiralByAngle* block. Points are indicated by circles and labels, and light blue lines indicate the beginning and the end of each *symmNose* sub-block. These sub-blocks have a label that indicates the discretization strategy (0 = *spiralByAngle* strategy, 1 = uniform strategy). The uniform strategy consists of the division of edge pieces according to the angular length and/or arc length according to the *noseAngleRatio* parameter. The other vertices of the sub-blocks (opposite to the points A,B,C,D,E,F in figure 4.13) are found using the same method of *spiralByAngle* based on the curvature centre of the reference spiral. In the first half of *symmNose* the reference spiral is the fixed one, while in the second half the reference is the mobile spiral.

The *(fix/mob)Center(Indexes/Angles)* are entries of *scrollDict* which determines the centre of the *symmNose* block. It is necessary to insert 4 indexes and 4 angles for each spiral. Each entry corresponds to different orbiting angles (0°, 90°, 180°, 270°) and the position of the centre points is interpolated in between.

The *symmNose* block entry in the *scrollMethods* list is:

symmNose $(blkIdxs)$ $(blkDivs)$ $(i_{\mathbf{A}}\ i_{\mathbf{B}})$ $(a_{\mathbf{A}}\ a_{\mathbf{B}})$ $(i_{\mathbf{C}}\ i_{\mathbf{D}}\ i_{\mathbf{E}}\ i_{\mathbf{F}})$ $(a_{\mathbf{C}}\ a_{\mathbf{D}}\ a_{\mathbf{E}}\ a_{\mathbf{F}})$

Where:

- $(blkIdxs)$ are the sub-block indexes (0 = *spiralByAngle* type of sub-block, 1 = uniform filling). With respect to figure 4.13, there are 6 sub-blocks in the following order: 0 1 1 1 1 0.
- $(blkDivs)$ tangential divisions of the sub-blocks indicated in the *blkIdxs* section. The radial and axial divisions are the global ones previously defined in the *scrollDict*. Obviously, the radial $(jDiv)$ and axial $(zDiv)$ must coincide with the *spiralByAngle* block, to ensure connectivity.
- $(i_{\mathbf{A}}\ i_{\mathbf{B}})$ are the curve indexes of the points A and B (the extremes).
- $(a_{\mathbf{A}}\ a_{\mathbf{B}})$ are the curve tangential angles of the points A and B.
- $(i_{\mathbf{C}}\ i_{\mathbf{D}}\ i_{\mathbf{E}}\ i_{\mathbf{F}})$ are the curve indexes of the points C, D, E, F (figure 4.13). If the user desires to add more sub-blocks, additional points need to be included in this list.
- $(a_{\mathbf{C}}\ a_{\mathbf{D}}\ a_{\mathbf{E}}\ a_{\mathbf{F}})$ are the curve indexes of the points C, D, E, F.

squeezeBox The *squeezeBox* method is necessary to "close" the mesh and connect the first and last *spiralByAngle* blocks. If a bad mesh quality is recorded at the conjunction between the *spiralByAngle* blocks and the *squeezeBox* block it is possible to change the value of the *phiSqueeze* angle, which will reduce/increase the tangential angular width of the first elements at the conjunction.

This block is subdivided into three sub-blocks, which can be observed in figure 4.14. There are two sub-blocks of type A and one central sub-block of type B.

The *squeezeBox* block entry in the *scrollMethods* list is:

squeezeBox $(jDiv_A\ jDiv_B\ iDiv)$ $i_{\mathbf{A}}\ a_{\mathbf{A}}\ i_{\mathbf{B}}\ a_{\mathbf{B}}\ i_{\mathbf{C}}\ a_{\mathbf{C}}\ i_{\mathbf{D}}\ a_{\mathbf{D}}$

Where:

- $(jDiv_A\ jDiv_B\ iDiv)$ are the block divisions. Respectively, the radial divisions of sub-blocks of type A, the radial divisions of sub-blocks of type B, the tangential divisions

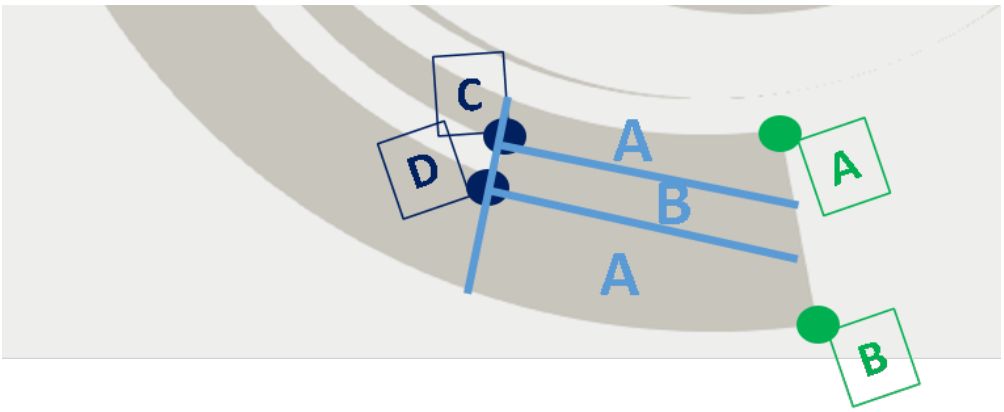

Figure 4.14: scrollMethods: squeezeBox.

of the block. The radial divisions of the blocks of type A must be the same of the *spiralByAngle* blocks to ensure perfect connectivity.

- $i_{\mathbf{A}}$, $i_{\mathbf{B}}$, $i_{\mathbf{B}}$, $i_{\mathbf{B}}$ are the curve indexes of the points A, B, C and D.
- $a_{\mathbf{A}}$, $a_{\mathbf{B}}$, $a_{\mathbf{B}}$, $a_{\mathbf{B}}$ are the curve tangential angles of the points A, B, C and D.

Chapter 5

Expanders and real gas effects

The CoolFOAM wrapper is validated in the first section of this chapter, followed by an analysis of the influence of the determination of real gas properties in a CFD simulation of a scroll expander. The second part of the chapter contains a multi-component numerical analysis of an expander and a plate heat exchanger.

5.1 CoolFOAM validation and real gas effects

5.1.1 Validation

This section contains three validation cases based on experimental studies available in literature. The first case concerns the investigation of natural convection of air in a heat cavity, originally performed by Betts and Bokhari [23]. The other test cases have been carried out on two different nozzles at the *Test Rig for Organic VApors (TROVA)* of Politecnico di Milano [155].

Buoyant cavity

The first comparison is based on the experimental investigation of the turbulent buoyant flow of air in a rectangular box-shaped cavity. The turbulent nature of the flow depends on the geometric proportions of the cavity, as well as the Rayleigh number. The cavity internal geometry is schematized in figure 5.1: the thickness (W) of the box is 0.076 m, the height (H) and the width (D) are respectively 0.52 and 2.18 m. A temperature difference of 19.2 K is maintained between the two y-z surfaces, while the remaining walls are considered adiabatic. The computational domain has been discretized with a structured mesh, taking advantage of the rectangular shape of the system. After a grid convergence analysis, the simulation has been carried out with approximately 80,000 cells.

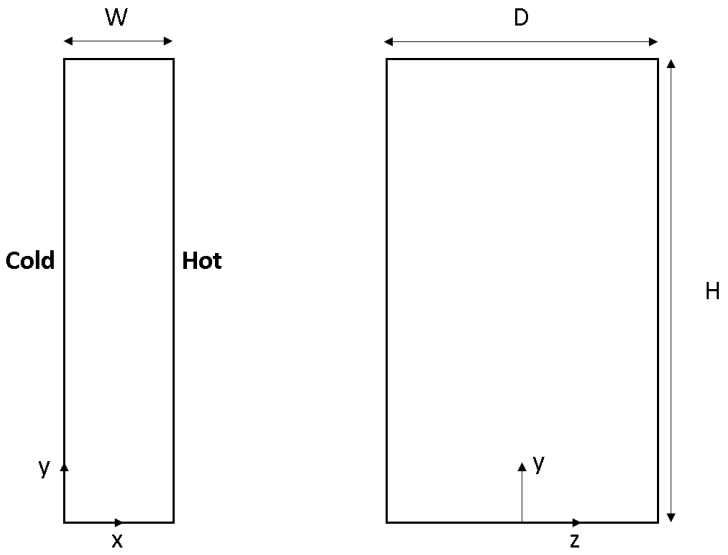

Figure 5.1: Buoyant cavity: geometry scheme. [56]

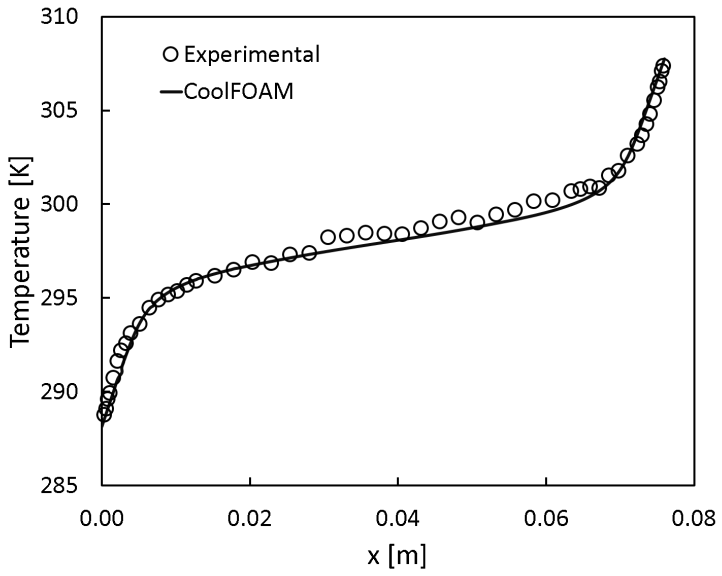

Figure 5.2: Buoyant cavity: temperature trends at $y/H = 0.5$. [56]

The ideal gas approximation is more than tenable for the operative temperature and pressure ranges investigated in this first analysis. Moreover, the specific heat, viscosity and thermal conductivity maximum variations are less than 5% in these conditions. For these reasons, the results obtained with the new library are very similar to the ones calculated with the original *OpenFOAM* thermophysical models. In fact, the absolute variations of temperature and vertical velocity, U_y, are in the order of 0.01 K and $1 \times 10^{-4}\,\mathrm{m\,s^{-1}}$ respectively. As a consequence, it has been chosen to include in the following graphs only the solutions obtained with the CoolFOAM library.

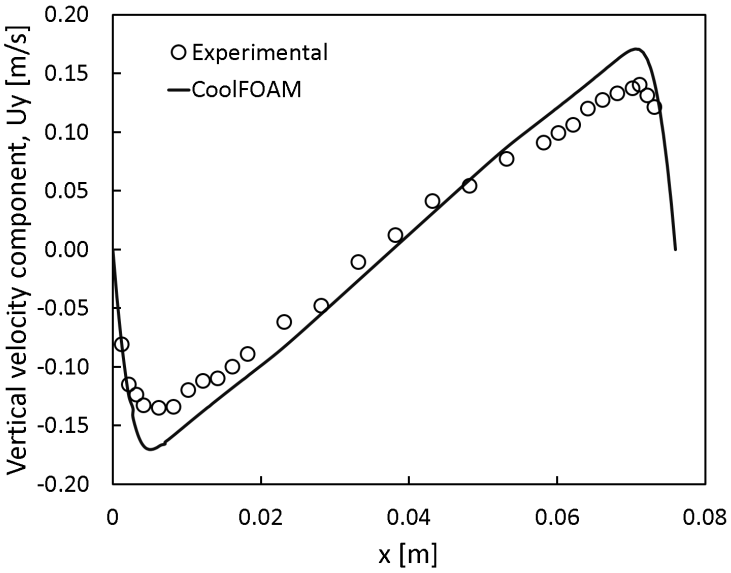

Figure 5.3: Buoyant cavity: vertical velocity trends at $y/H = 0.5$. [56]

In particular, the figures 5.2 and 5.3 display the trends of temperature and vertical velocity in the x direction at $y/H = 0.5$, compared with experimental values.

The purpose of this case is to demonstrate the correct implementation of the CoolProp functionalities in *OpenFOAM*, using a verification case widely used in the community.

Convergent-divergent nozzle

The first experimental case of the *TROVA* test rig regards the expansion of octamethyltrisiloxane (MDM) in a convergent-divergent nozzle. The work by Spinelli et al. [155] investigates two nozzles, characterized by downstream Mach numbers close to 1.5 and 2.

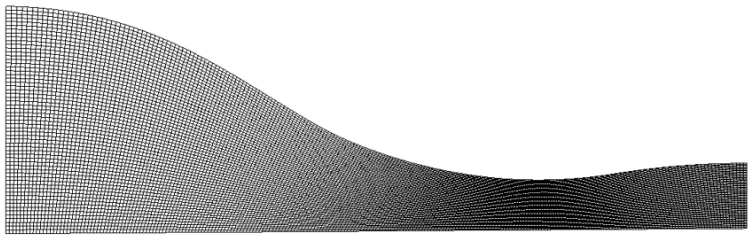

Figure 5.4: Convergent-divergent nozzle: computational domain. [56]

The first nozzle's results are considered in this section: particularly, the case with upstream compressibility Z of approximately 0.81 is the object of the numerical analysis. The considered gas is then strongly non-ideal: this allows the full demonstration of the CoolFOAM interface potentialities. The experimental data available include static pressure measurements and Mach number evaluations. The pressure has been detected through pressure transducers connected to up to nine pressure taps located on the nozzle symmetry axis. The

Mach number has been directly evaluated through the estimation of the Mach waves slope, identified from Schlieren images.

The computational domain has been discretized with a structured two-dimensional mesh, represented in figure 5.4. The independence of the solution to the dimension of the mesh elements has been reached with approximately 60,000 cells. The good quality of the mesh, characterized by a non-orthogonality of less than 30° and by a skewness minor of 0.3, has allowed the adoption of accurate numerical schemes. More precisely, the simulation, performed with the **rhoPimpleFoam** solver, has been executed with a second-order discretization accuracy for the advective and Laplacian terms.

Since the fluid reaches supersonic velocities, there is no need for boundary conditions at the outlet section. At the inlet, a total pressure of 4.59 bar and a total temperature of 512.6 K have been imposed. The solution has been firstly initialized with ideal gas conditions, switching then to the Helmholtz equation of state. After this first step, the hypothesis of inviscid flow has been considered valid for this kind of fluid, characterized by a very low viscosity. The simulation with zero viscosity and laminar approximation has produced very good results when compared to the experimental data, as shown in figure 5.5.

Looking for a higher level of accuracy, the numerical analysis has been improved with polynomial correlations for the viscosity and the thermal conductivity. The reason of adopting polynomials instead of the CoolProp interface stands in the absence of correlations for these properties of the MDM fluid in the CoolProp library. In addition to that, a turbulence k-epsilon model has been implemented, in order to obtain a better representation of the real case's physics.

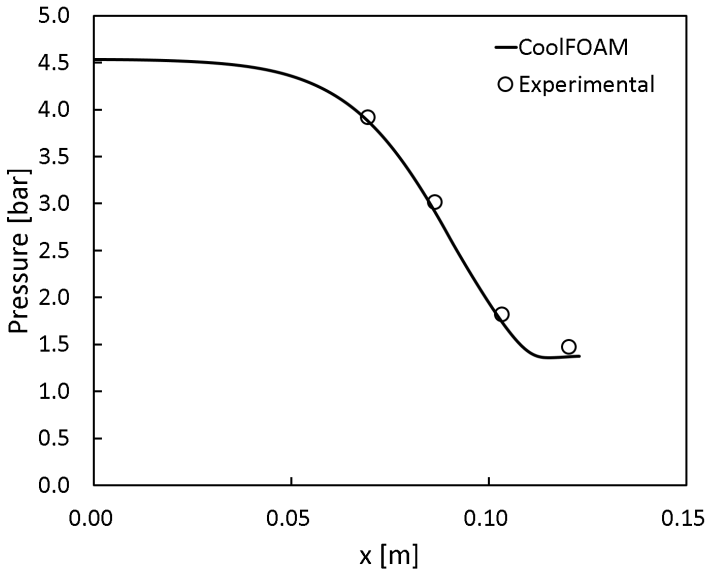

Figure 5.5: Convergent-divergent nozzle: pressure values on the symmetry axis, inviscid flow. [56]

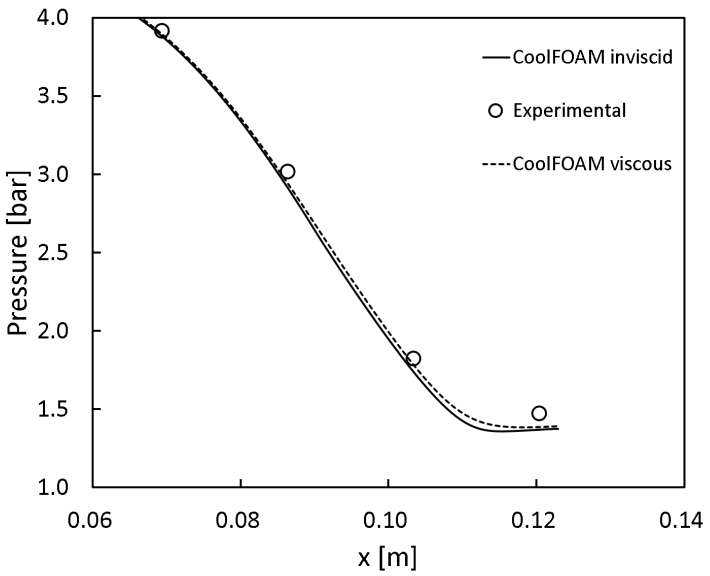

Figure 5.6: Convergent-divergent nozzle: pressure values on the symmetry axis, viscous and inviscid flow. [56]

The pressure trend along the symmetry axis for the turbulent-viscous simulation fits better the experimental values, as represented in figure 5.6. It has to be noticed that the inviscid simulation's results are still fairly close to the experimental values: the possibility to adopt this hypothesis remains a valid possibility for the siloxane fluid analyzed if there is the will of reducing the general level of complexity of the simulation.

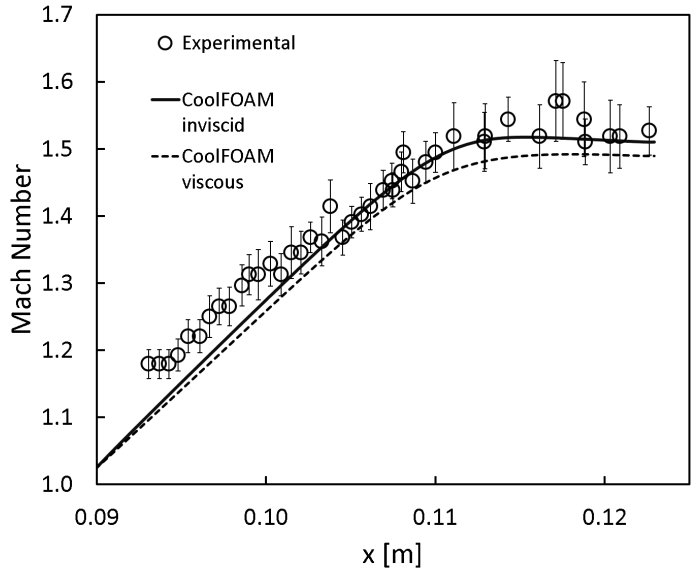

Figure 5.7: Convergent-divergent nozzle: Mach number values on the symmetry axis, viscous and inviscid flow. [56]

The results of the viscous-turbulent simulation have been compared also with the experimental evaluation of the Mach number along the symmetry axis. The graph represented in

figure 5.7 represents this comparison in the region close to the outlet section, where experimental data are available.

Very high accuracy can be noticed in the final part of the nozzle, where the Mach number values are well replicated by the numerical analysis. For lower values of the x coordinate, both the viscous and inviscid models underestimate the dynamic contribution of the flow, if compared to the experimental evidence. It is interesting to notice how the inviscid model better fits these references: the dissipating action of viscous effect has a reducing effect on the Mach number.

Compressible turbulent flow over a Backward-Facing Step

The last validation case reported in this section is based on a nozzle similar to the one described in section 5.1.1. The main difference is the presence of a backward facing step in correspondence of the throat section of the duct. The consequence is the generation of an oblique shock at the reattachment point after the flow separation originated by the wall discontinuity. This phenomenon and the deriving shock-waves system is highlighted in the Schlieren image of the flow: the complex behaviour of the flow has been extensively described in [71].

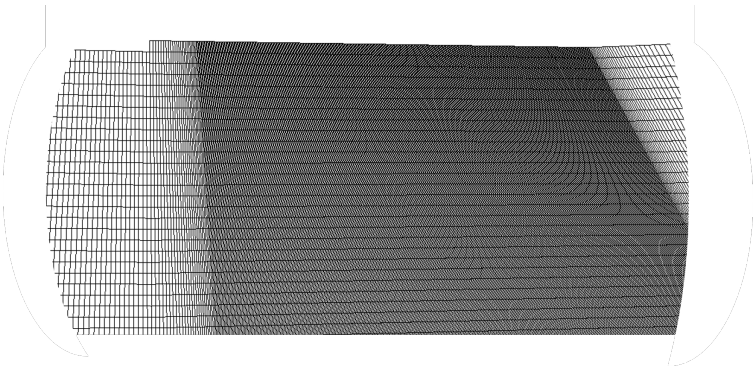

Figure 5.8: Backward Facing Step: detail of the computational domain. [56]

A detail of the mesh close to the discontinuity has been represented in figure 5.8. The structured grid has been refined in the proximity of the shock-waves system according to the experimental reference. In addition, the cells faces have been aligned with the shocks, trying to capture the first pressure discontinuity as accurately as possible. This approach has allowed the maintenance of a very good quality of the mesh with a reasonable number of elements (less than 100,000).

The boundary conditions required for this *CFD* analysis are the inlet total pressure and total temperature, respectively of 4.58 bar and 520.1 K. These conditions correspond to a compressibility factor of 0.82 at the inlet section. The outlet conditions are not required, because of the univocal behaviour of the supersonic flow.

The pressure trend along the symmetry axis gives a very accurate representation of the experimental values, as represented in figure 5.9. The shock is captured with reasonable accuracy by the viscous numerical simulation.

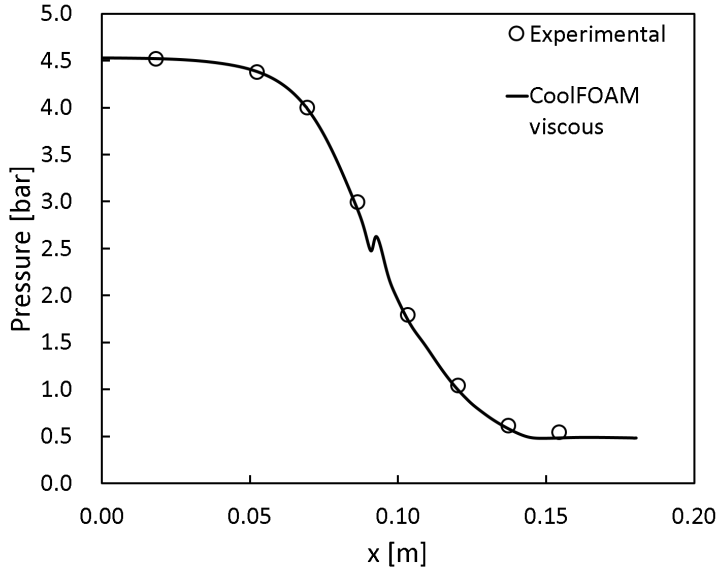

Figure 5.9: Backward Facing Step: pressure values on the symmetry axis, viscous flow. [56]

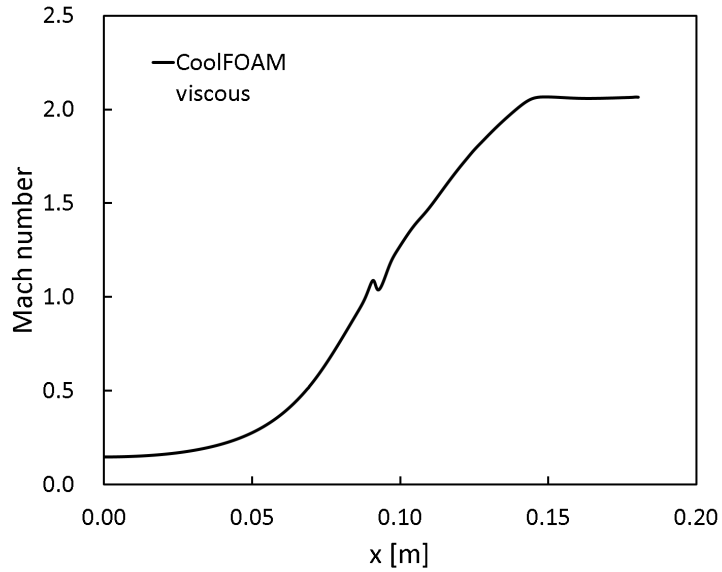

Figure 5.10: Backward Facing Step: Mach number values on the symmetry axis, viscous flow. [56]

In this case, no experimental data for the Mach numbers have been released, but the results of the numerical simulation are shown in figure 5.10. It is interesting to notice how the design Mach number at the outlet (approximately 2.0) has been confirmed by the *OpenFOAM* analysis.

5.1.2 Influence of the equation of state on the CFD analysis of a scroll expander

The last part of this section is focused on the influence of the Helmholtz energy formulation on the results of a *CFD* simulation of a scroll expander. Section 5.2 contains a detailed description of the employed expander and of the numerical aspects of the *CFD* simulation. Here, the focus is set on the influence of the selection of the equation of state on the final results.

Configuration	EOS	Thermodynamic	Transport
A	Ideal gas	Constant Cp	Constant μ and k
B	Bicubic HEOS	Bicubic HEOS	Bicubic Interpolation

Table 5.1: Thermophysical configurations

The expander has been analyzed with two different thermophysical configurations included in Table 5.1, where Cp, μ and k are respectively the specific heat capacity at constant pressure, the dynamic viscosity and the thermal conductivity. Some of the main performance indicators of the machine are summarized in Table 5.2, reporting the *Mass Flow Rate (MFR)*, the power and the pV (forces) efficiency.

Configuration	MFR	Power	η_{forces}
A	$0.0238\,\mathrm{kg\,s^{-1}}$	146.4 W	0.531
B	$0.0316\,\mathrm{kg\,s^{-1}}$	149.2 W	0.408

Table 5.2: Expander performance indicators

Configuration A enhances the resulting performance of the machine, with an efficiency 30% higher. On the other hand, the mass flow rate is reduced by 25 %. Consequently, the adoption of inaccurate thermophysical models can be particularly dangerous during the design phase of the machine. The overall computational time for a complete revolution of the machine is close to 9500 s for configuration B and close to 6600 s for configuration A. This results in a difference of approximately 40 %, which is definitely acceptable if the accuracy gain is considered. The output power difference (of only 3 W) is a misleading index in this case, as it would have given acceptable results notwithstanding the differences described above.

The difference in density between the two models is represented in Figure 5.11: the region with the biggest difference is the first working chamber (i.e. the one closer to the inlet), which is characterized by the lowest compressibility factor according to section 5.2. Accordingly, the density difference is lower in the proximity of the discharge region of the expander, where the deviation from the ideal gas behaviour is smaller.

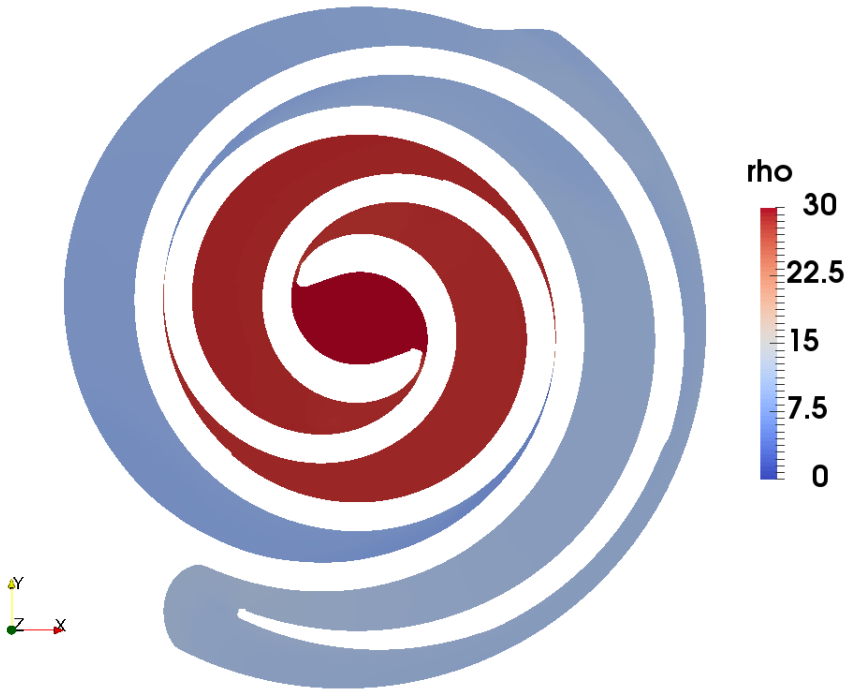

Figure 5.11: Density difference: configuration A - configuration B

5.1.3 Conclusions

A new library for the determination of thermophysical properties in *OpenFOAM* has been developed. The work validated in this section is based on the direct evaluation of the fluid properties through the open-source C++ library CoolProp.

The consistency of the developed models has been compared with experimental data for three validation cases. For the first test case, regarding a buoyant cavity, a typical *OpenFOAM* verification case has been solved in order to check the correct implementation of the two models. In the second and third cases, compressible flows with strongly non-ideal behaviour have been investigated. The results obtained from the numerical analysis present a very good level of agreement with the experimental references.

The author has conducted a study on the performance of different thermophysical property models for the numerical analyses of typical *ORC* and refrigeration applications. The investigation has been carried out in the *OpenFOAM* framework, thanks to the CoolFOAM wrapper for the CoolProp integration in the *CFD* code. Tabular interpolation of the *HEOS* can heavily affect the density calculation, especially in proximity of the critical point and in some points of the saturation line.

Also, high differences are found if models other than *HEOS* are employed. Such difference has a high impact on the outcome of simulations, for example in scroll expanders: the pV efficiency and the flow rate have been found to be highly affected by such misprediction. In light of this, the tabular interpolation of *HEOS* is always suggested in the typical working

range of *ORC*. In addition, direct calls to *HEOS* should be considered when the saturation line or the critical point is approached.

5.2 Multi-component numerical investigation

In this section, a scroll expander has been coupled with a plate heat exchanger and analyzed in a multi-component configuration employing the *CFD* tools introduced in the previous chapters. One of the main objectives of this study is to isolate a portion of an *ORC* and analyze the interactions between the two components considered. This section contains the description of the initial system, an explanation of the alternative configurations tested and the definition of the numerical methods.

5.2.1 ORC system description

The system presented by Bianchi et al. [24] has been taken as a reference for the definition of the model layout. The original cycle consists of two brazed plate heat exchangers as evaporator and recuperator, a piston expander, a volumetric gear pump and a shell and tube heat exchanger as a condenser. The system has been experimentally tested with evaporation pressures up to 19 bar, hot source temperatures up to 358 K and R134a as the working fluid.

The current analysis regards exclusively the expander and the recuperator, which have been numerically modelled (Figure 5.12). It has been decided to analyze a scroll expander, which could be a potential replacement for the piston. The expander has been coupled with a plate heat exchanger and the whole system has been analyzed under the boundary conditions summarized in table 5.3. The *CFD* analysis has run fully turbulent with the k-ω SST model of Menter [111] with updated coefficients [112].

Boundary	**Pressure**	**Temperature**	**Velocity**
Inlet	20 bar	358 K	Zero gradient
Outlet	11 bar	Zero gradient	Zero gradient
Walls	Zero gradient	Adiabatic	No slip
Recuperator interface	Zero gradient	Far field temperature	No slip

Table 5.3: Boundary conditions

5.2.2 Scroll expander

The machine investigated in this work corresponds to the commercial SANDEN TRSA09-3658 scroll compressor with a built-in volume ratio of 1.82. The geometry has been obtained by means of a reverse engineering technique, as illustrated in [114], and the machine has been operated in reverse to work as expander. The expander has been simulated in the absence of

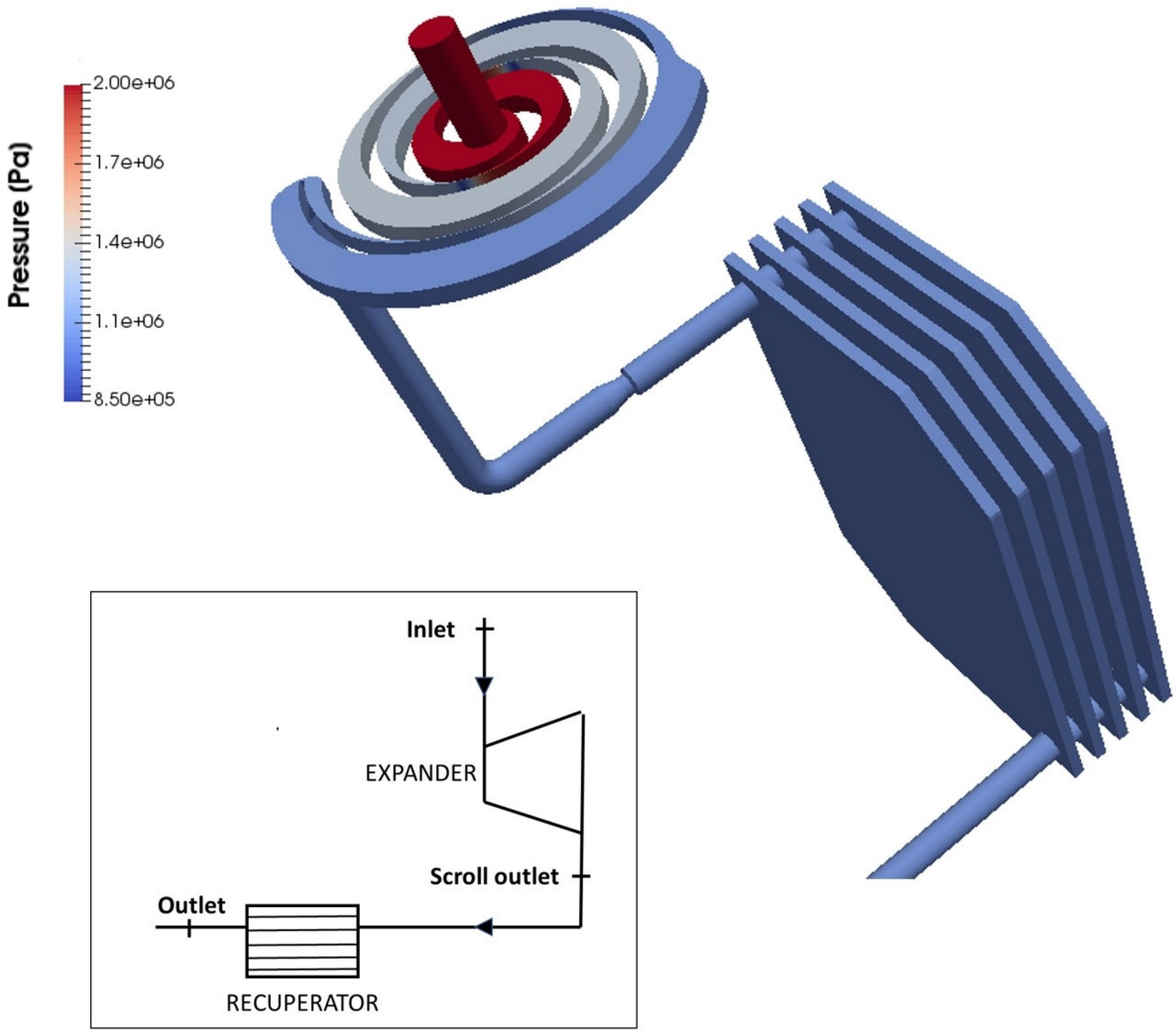

Figure 5.12: Numerical model and schematic of the ORC components investigated. The numerical domain is depicted by its pressure distribution [57].

axial gaps, while the flank gaps that characterize the operation of the machine are reported in Table 5.4. The size of the clearances is fully in line with common engineering practice.

The geometry has been then slightly modified. The first change operated regards the thickness of the scroll, which has been reduced to $1/7^{th}$ of the original value. In this way, the total number of cells of the scroll mesh is strongly reduced without altering the flow nature and the dynamic behaviour of the expander. The second change regards the modification of the position of the discharge port, which has been redesigned to be axial. This choice has allowed avoiding the presence of a non-conformal interface between the discharge area and the morphing region of the scroll domain. These changes are driven by computational effort and stability reasons and do not alter substantially the flow structures and the performance of the machine.

The dynamic mesh strategy employed for the scroll expander is the custom predefined mesh generation, described in section 4.4.

Position	Gap Size (μm)
0° (inlet chambers close)	20
90°	36
180°	94
270°	36

Table 5.4: Flank gap size evolution during the operation of the machine.

5.2.3 Plate heat exchanger and piping system

The plate heat exchanger used for this analysis has been designed to fit the mass flow rate of the expander with reduced thickness. The recuperator consists of 5 elements, which have been modelled only for what concerns the hot side, imposing the appropriate boundary conditions at the interface with the solid plates. The mesh of the fixed regions of the computational domain (pipes and recuperator) has been realized with the **cfMesh** application [86]. In particular, this application is an alternative to **snappyHexMesh** to generate grids mainly characterized by hexahedral cells. In order to connect areas with different refinement levels, transition regions are discretized by means of polyhedral.

The boundary conditions between the recuperator domain and the solid region in correspondence of the cold side are particularly important. The author has adopted the *externalWallHeatFluxTemperature* boundary condition. This boundary condition applies a heat flux condition based on a multi-layer wall analytical modelling, and requires the thickness (1 mm) and thermal conductivity ($200\,\mathrm{W\,m^{-1}\,K^{-1}}$) of each solid layer (just the aluminium of the heat exchanger in this case), the overall heat transfer coefficient of the modelled side, i.e. the cold side, of ($500\,\mathrm{W\,m^{-2}\,K^{-1}}$) and an average temperature of the the modelled side (325 K). This boundary condition allows for a realistic simulation of the temperature field inside the hot section of the heat exchanger without the extra cost of a conjugate heat transfer analysis.

5.2.4 Thermophysical properties

The thermophysical properties of the refrigerants have been firstly evaluated using the ideal gas approximation with constant thermodynamic and transport properties. However, the working fluids are employed in conditions in which the deviation from the ideal behaviour should be considered. Hence, it has been decided to test, and then adopt, the equations of state published by Tillner-Roth et al. [166] and Richter and al. [138]. Both formulations are explicit in the Helmholtz energy.

The real gas modelling is accomplished by means of the CoolFOAM wrapper developed by the author [56]. The employment of CoolFOAM has produced an increase of the 23 % in the computational time of one revolution of the expander with respect to the ideal gas

model case. Nevertheless, there are significant improvements in terms of the accuracy of the calculation, since the inlet compressibility factor Z is around 0.85. The deflection from the ideal behaviour of the refrigerant during the operation is reported in Figure 5.13. The maximum deflection from 1 is found in the inlet chamber and is roughly 15%. As a general remark, the real gas effects are lower (Z tends to 1) as the fluid goes through the gaps and increase in the bulk of the chambers.

Figure 5.13: Compressibility factor for R134a during the operation of the expander [59]

5.2.5 Results

Mesh Results

The final result is a mesh with satisfying values of skewness, orthogonality, and aspect ratio. All these parameters, and many others, widely fit all the quality criteria set by the OpenFOAM standards. An example of structured mesh is presented in Figure 5.14, which represents the discretization of a SANDEN TRSA09-3658 scroll compressor. In this application, the *squeezeBox* strategy described in section 4.4 has not been applied, using an extensions of the *spiralByAngle* block to close the structured domain. This has been possible because of the shape of the domain at the end of the mobile spiral, as shown in figure 5.14.

Table 5.5 contains some illustrative values of skewness, non-orthogonality, and aspect ratio for this grid.

Position	0°	90°	180°	270°
Max. Skewness	2.28	2.39	2.45	2.58
Max. Non-Orthogonality	78.23	60.96	50.30	50.99
Avg. Non-Orthogonality	8.04	7.41	7.61	7.90
Max. Aspect Ratio	863.25	528.44	219.34	200.98

Table 5.5: Mesh quality parameters in function of the mobile scroll position.

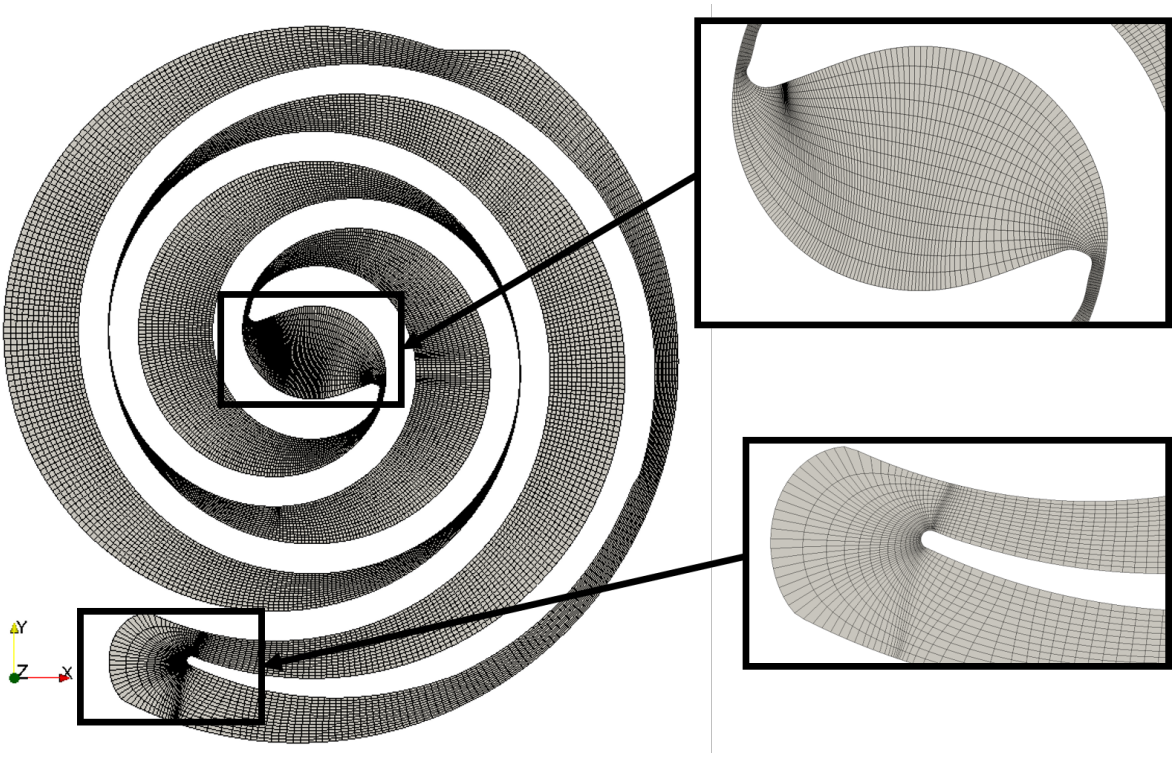

Figure 5.14: Structured mesh: final result [59].

System performance with the standard layout

The pressure pattern as the operation of the scroll evolves is reported in Figure 5.15. The filling procedure of the high-pressure chamber can be noticed passing from Figure 5.15a–d. Furthermore, the good operation in the proximity of the design point is proven by the pressure of the chamber before the opening of the discharge port (Figure 5.15d shows the pressure distribution of a few degrees before the actual opening): the pressure in the chamber is slightly above the output value, and therefore, no under or over-expansion is recorded. The minimum pressure recorder in the domain is slightly above 8 bar and it is reached downstream the working chamber sealing clearance. In such areas, the flow becomes choked as reported in [33]. The simulation catches well such phenomena and proves to be robust and stable also in case of transonic problems.

The mass flow rate elaborated over a complete revolution of the expander is represented in Figure 5.16. The average value settles down at $0.0275\,\mathrm{kg\,s^{-1}}$. However, it should be

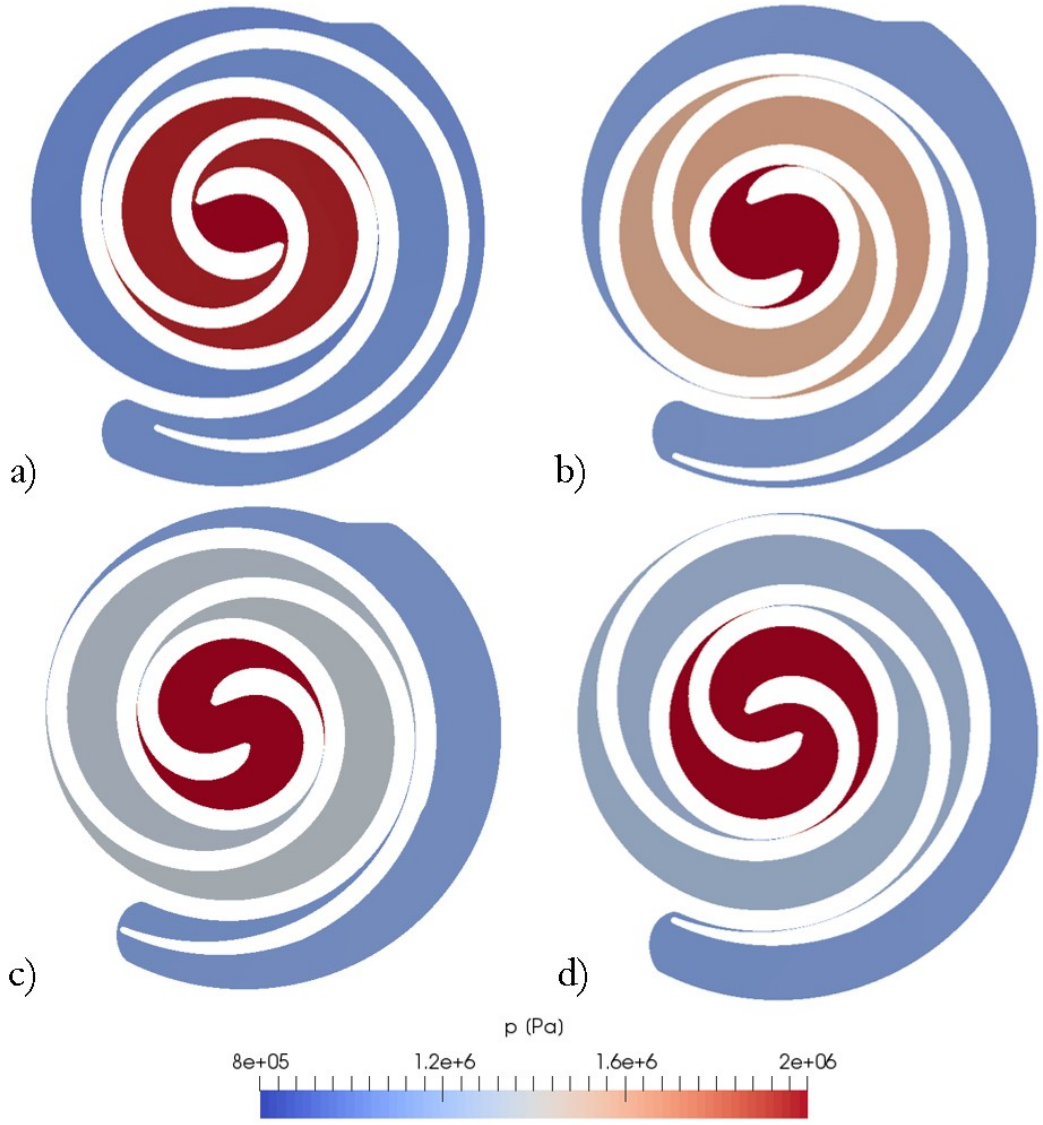

Figure 5.15: Pressure pattern evolution during the operation of the expander: (**a**) 0°, (**b**) 90°, (**c**) 180°, and (**d**) 270°.

considered that the geometry analyzed represents only a portion of the entire machine. Consequently, the value reported is comparable with other analyses carried out on the same expander [114]. A series of high frequency oscillations is recorded in the scroll outlet trend reported in figure 5.16. These oscillations are given by a fluid dynamic interaction between the fluid dynamic structures originated downstream of the flank gaps and the positioning of the discharge port. However, these oscillations are quickly smoothed down in the pipe connecting the scroll expander and the recuperator.

The ratio between the theoretical volume processed by the scroll and the one calculated by means of the *CFD* analysis is called *Volumetric Flow Matching Ratio (VFM)* . The resulting *VFM* value is 1.22, which is included in the range between 1.07 to 1.3 reported in [109]. The mass imbalance resulting from the simulation is of the order of 0.2 %, which is a definitely small value considering the application of two *ACMIs*. The expander outflow is characterized

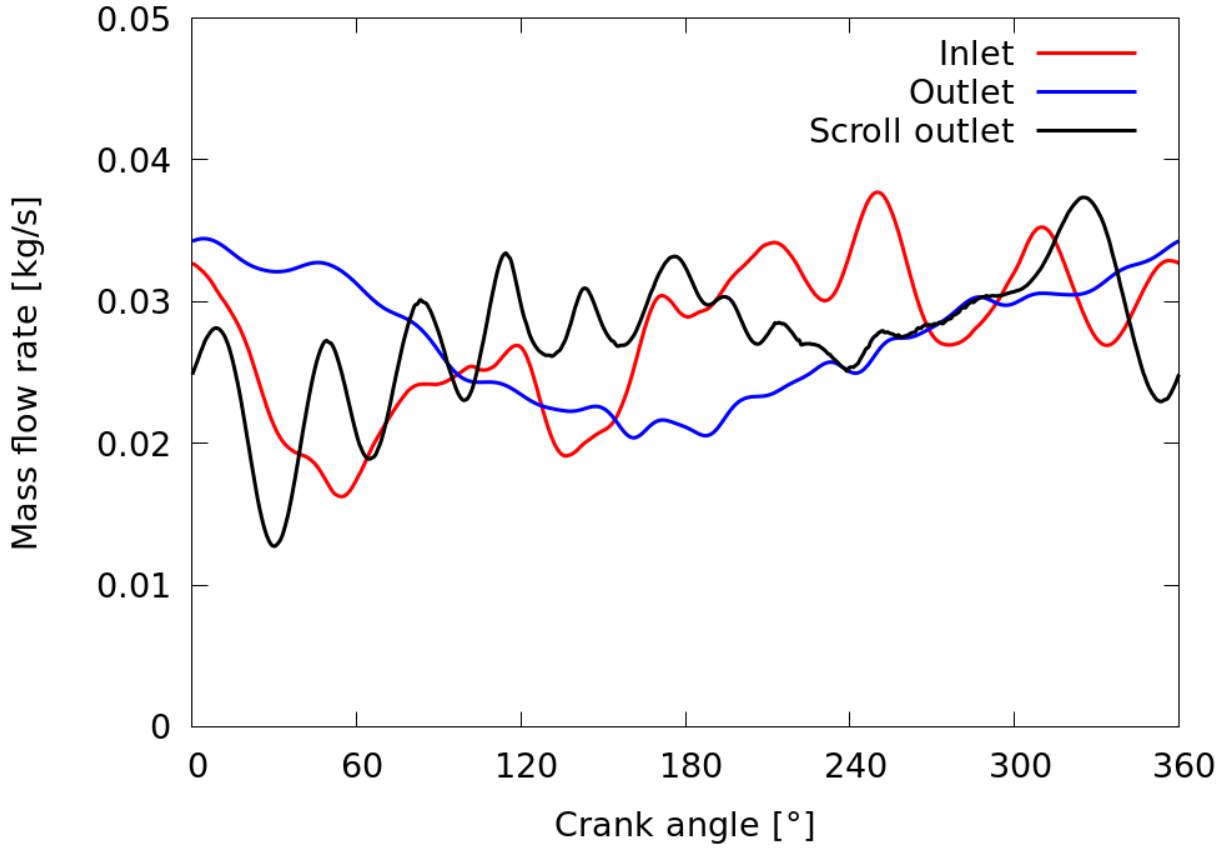

Figure 5.16: Mass flow rate trends: Red - scroll inlet, Blue - heat exchanger outlet, Black - scroll outlet. The smoother trend of the domain outlet can be noticed if compared to the scroll outlet [57].

by high pulsations if compared to the inlet trend. However, the heat exchanger and piping systems have a flywheel effect on these pressure pulsations, resulting in a smoother mass flow trend at the outlet of the domain (figure 5.16).

The output power extracted from the expander varies from 50 W to 250 W, with an average value of 149.2 W. The reported values have been evaluated as the product between the rotational speed (2000 rpm) and the mechanical torque. The outlet pressure variation over a shaft revolution is represented in Figure 5.17. The minimum value, slightly below 10.8 bar, is registered right after the discharge phase, while the average is 11.03 bar. The internal pV efficiency of the expander has been calculated as the ratio of the power produced by the expander and the power it would produce if the expansion of the fluid was isentropic. The average value is close to 41 %, which is not large but still reasonable for this kind of applications [109]. The same tests carried out with the ideal gas approximation leads to an under-prediction of the output power of less than 5%, but the mass flow rate difference is around 25% and the pV efficiency misprediction is even higher (roughly 30%).

The system integration can also give insight into the actual working conditions of the heat exchanger. In this case, the heat exchanger that is typically assumed to work in steady

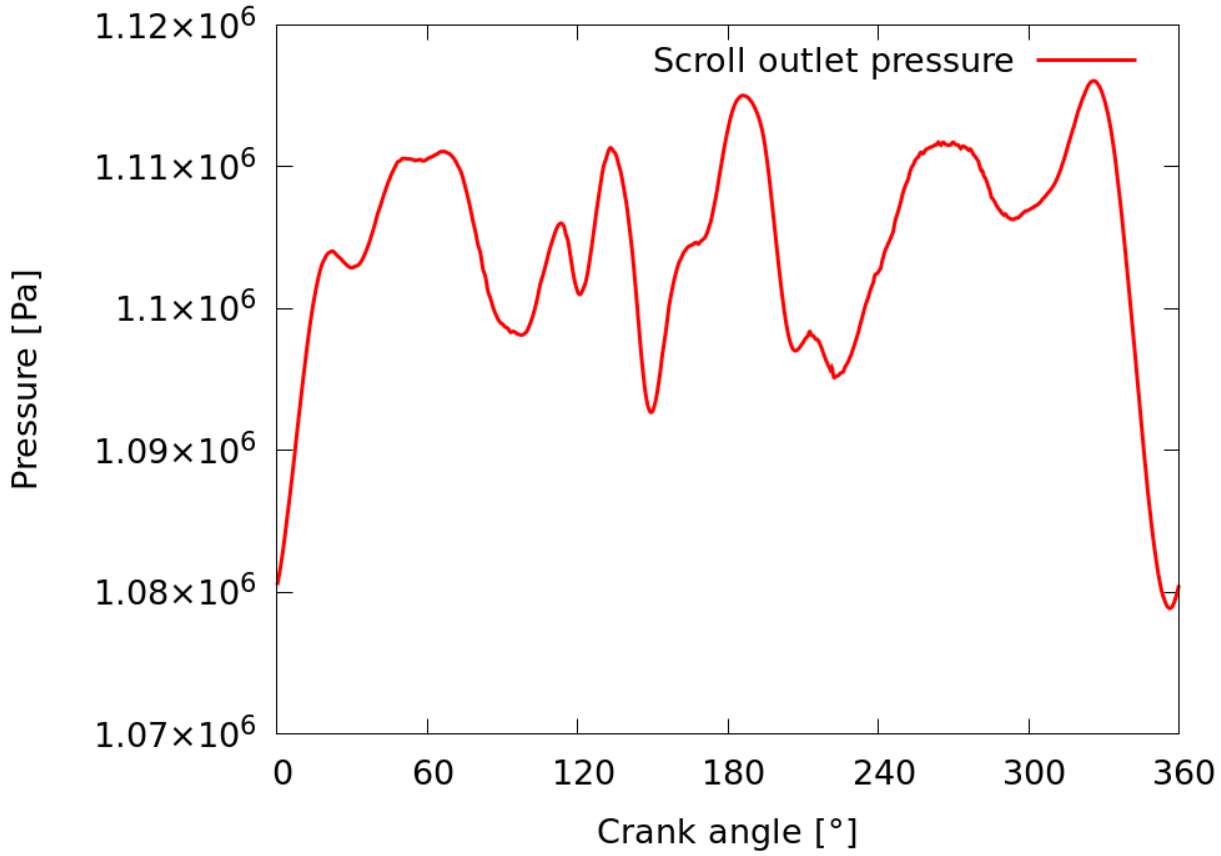

Figure 5.17: Pressure variation over a revolution of the shaft [57].

condition, sees a high variation of flow rate. These pulsations reflect in an oscillation of the heat transfer coefficient of about 10 %. Also, a good balance of the heat exchange and of the processed flow rate among the different plates is recorded. Peaks of heat transfer coefficient of about ten times the mean value are found in the proximity of the inlet channel of each plate.

System performance with super heating

This section regards the investigation of the consequences of a variation in the hot source temperature or flow rate. This variation might translate into a superheating of the working fluid due to increased heat transfer at the evaporator. In such conditions the inlet state of the expander is distanced from the saturated vapour line. The representation of the states on the ph diagram is reported in Figure 5.18. In the same diagram also the expander outlet state and the recuperator outlet are depicted.

It can be noticed that the system exploits very well the extra enthalpy provided: as the efficiency of the scroll remains very similar, a proportionally higher portion of heat is transferred to the cold side. Indeed, the enthalpy difference between the superheated and "base" outlet states is smaller than the difference in the inlet states. In both cases, the risk

of condensation in the plate heat exchanger is minimal due to the noticeable distance from the *Vapor-Liquid Equilibrium (VLE)* at the outlet, but also in the most critical areas inside the device.

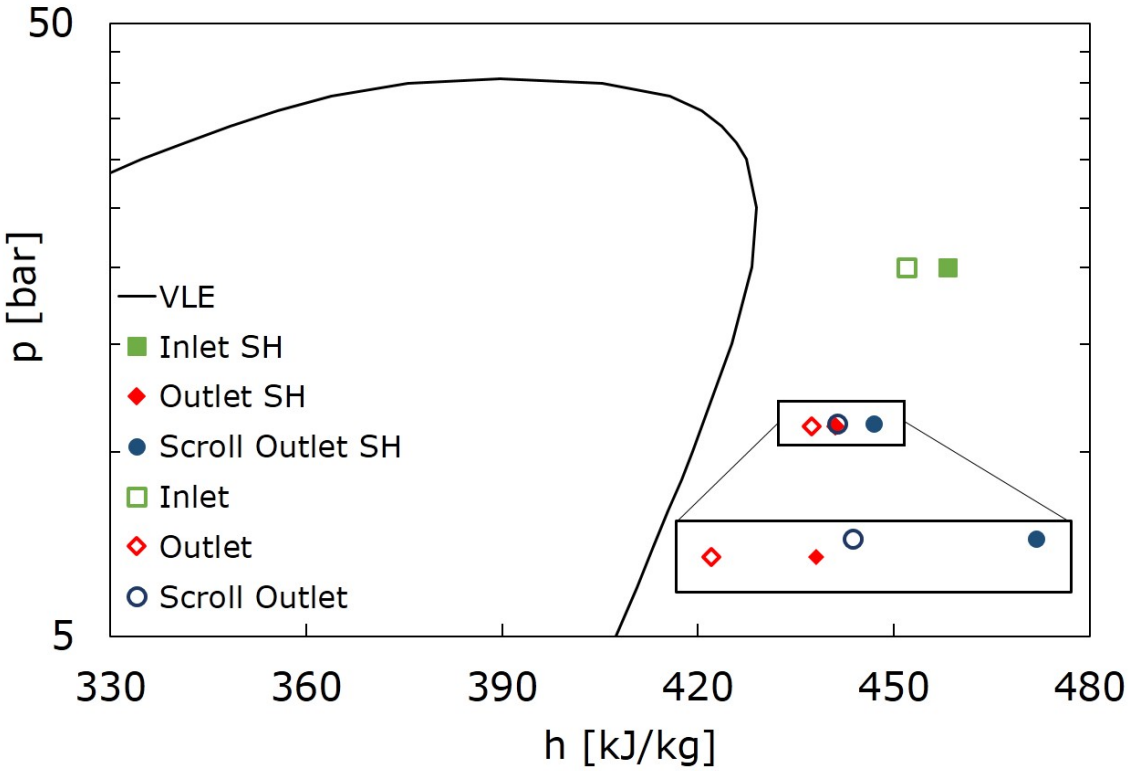

Figure 5.18: ph diagram of R134a and fluid states in the investigated cases: SH for super heating [57]. States are defined in Figure 5.12.

Case	**R134a**	**R134a_SH**	**R1234yf**
Flow rate $\mathrm{kg\,s^{-1}}$	0.0275	0.0266	0.0315
Power W	145.22	144.97	144.74
η_{forces}	39.69 %	39.67 %	39.64 %
T scroll outlet K	334.85	340.04	336.93
T outlet K	330.90	333.82	332.36
PHE Heat flux $\mathrm{W\,m^{-2}}$	120.06	181.38	164.82

Table 5.6: Scroll expander and recuperator: system performance

The increase in the scroll inlet temperature leads to a slight reduction of the mass flow rate processed by the machine, while the output power and the pV efficiency maintain similar values (Tab. 5.6). The mass flow rate reduction can be the cause of a lower pump consumption, which is beneficial for the cycle overall efficiency.

System performance with candidate replacement R1234yf

The differences in system performance with the adoption of the R1234yf working fluid can be retrieved from Table 5.6. In the new configuration, there is an increase in the mass flow

rate processed by the expander, which is related to the higher density of the new working fluid. On the contrary, the output power and the pV efficiency are not strongly affected by this modification. For what concerns the recuperator parameters, a higher scroll outlet temperature and the increase in mass flow rate contribute rising the overall heat flux. This reflects in a higher part of heat that is transferred to the cold side, increasing the efficiency of the cycle.

5.2.6 Conclusions

In this section, the system integration of micro-*ORC* components has been carried out. The author has proposed this numerical work to highlight the possible outcomes of a full three-dimensional analysis of coupled *ORC* components. The integration proves to be of interest when off-design operating conditions or candidate fluid replacements are to be investigated.

The application of *ScrollFOAM* provides a unique tool for the numerical investigation of refrigerant behaviour in scroll machines with open-source tools. The procedure has been demonstrated for a scroll expander. This tool can be used to foresee the off-design behaviour of the *ORC* cycle in terms of output power performance. Variations in the boundary conditions have been tested, and the solver proves to be robust and accurate in catching over- and under-expansions. The suitability of the entire infrastructure to the investigation of *ORC* cycles is enhanced by the coupling of the solver with CoolFOAM, the CoolProp wrapper for *OpenFOAM*. With such an expedient, the real gas modelling gains in accuracy as the Helmholtz equation of state can be used.

As highlighted in this section, the development of scrollFOAM is a fundamental step to enlarge the open-source modelling capabilities of *ORC* expanders, as the state-of-the-art in fast and robust simulations of positive displacement expanders in OpenFOAM is limited to piston-type expanders. The extension of the modelling capabilities to other types of machines is needed for a more spread usability of *CFD* in *ORC* cycles. The open-source nature of the code allows for future developments of a custom solver able to deal with complex phenomena, such as phase change in the heat exchangers and two-phase expansion.

Chapter 6

PDSim and scrollFOAM: comparison and validation

This chapter is focused on the assessment and validation of the scroll machines simulation tools presented in this work. Danfoss Compressors, one of the most important companies in the refrigeration sector, has provided a test case based on a commercial compressor in the scope of a research collaboration project. The test case, which includes the complete geometry of the scroll machine and the results of an experimental campaign, has been simulated using the software developed by the author. In the first part of the chapter, the experimental data have been taken as a reference for the validation of the numerical codes. Later, the results of the quasi-static and CFD simulations have been analyzed and compared. All the sensitive data have been normalized for confidentiality reasons.

6.1 The test case

The scroll compressor analyzed in this work is an air conditioning compressor developed for medium-to-large applications such as rooftops, chillers or process cooling. The simulations have all been performed employing the design working fluid (R410a) in oil-free conditions, although the original compressor works as an oil-flooded machine. The sealing action of the oil has been considered by reducing the flank gap size, while the cooling effects have been neglected. Figure 6.1 reports a simplified scheme of the geometry of the compressor, including a suction port (blue), a large reservoir downstream the discharge region (red) and the compression region containing the scroll wraps (grey).

The experimental campaign provided by *Danfoss Compressors* is characterized by three operating conditions. The operating point corresponding to the *ARI* standard has been taken as a reference, with a rotational speed of 2900 *rpm*. The pressure ratio has been varied to inspect under and over-compression. In particular, the pressure ratio of the *ARI* point

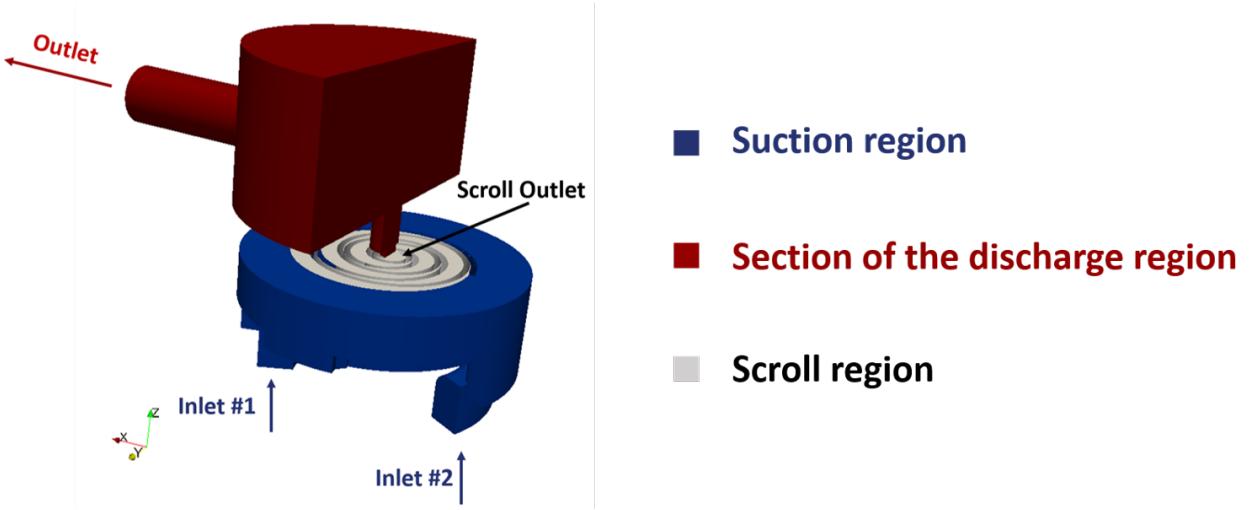

Figure 6.1: Scheme of the geometry of the test case [55].

is multiplied by 1.83 to reach the high *PR* point, while the low *PR* condition is set to a pressure ratio corresponding to the 51 % of the reference one. The experimental study is extensively described in the work presented by Picavet et al. [130].

6.2 OpenFOAM results

The simulations presented in this section have been performed with the built-in OpenFOAM solver *rhoPimpleFoam*, employing the libraries developed by the author and described in chapter 4.

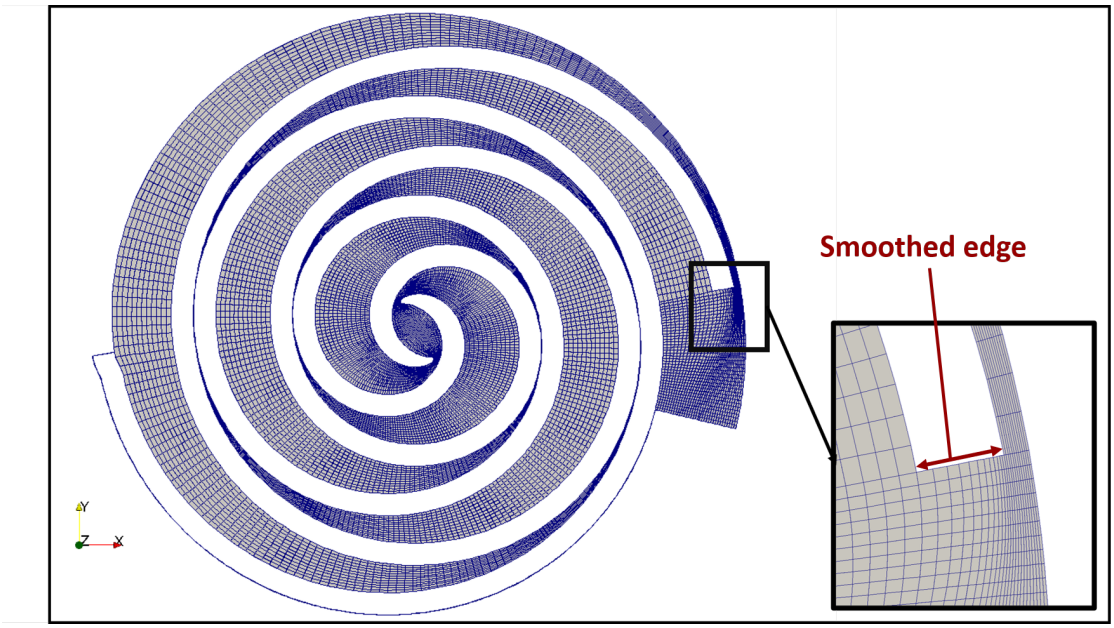

Figure 6.2: Structured mesh of the moving domain. Highlighted area: adaptive grading of the cells of the squeezeBox block [55].

While the moving region has been discretized with a structured mesh, in accordance

with the methodology reported in chapter 4, the stationary parts have been meshed with the unstructured mesh generator **snappyHexMesh**. The patch indicated in figure 6.1 with the name *Scroll Outlet* is an *Arbitrarily Coupled Mesh Interface (ACMI)* interface between the moving part and the discharge region. This patch has been used to evaluate the mass flow rate at the machine outlet. The resulting structured mesh is aligned with the software requirements in terms of mesh quality, as confirmed by the *OpenFOAM* native utility **checkMesh**. More particularly, the gap regions are characterized by regular stretched cells with an aspect ratio of approximately 220, as shown in figure 6.2.

The representation of the structured grid at an orbiting angle of 0° is reported in figure 6.2, where the region in correspondence of the end of the mobile spiral has been highlighted. This important area, which is in the proximity of the *ACMI* interface between the moving domain and the suction port, has been meshed with the aid of a quadratic grading function (typical of the *squeezeBox* block described in section 4) that reduces the size of the cells in accordance with the local width of the flank gap. The grading function has been applied to the edge reported as *Smoothed edge* in figure 6.2.

The simulations have run fully parallel on a 40 cores machine, with a computational time of approximately four scroll revolutions per 24 computational hours on a mesh with more than 2.5E+06 cells (corresponding to the case with the reservoir). Approximately, 600k and 800k cells have been used to discretize respectively the moving and the suction domains. The average values of *y-plus* calculated at the domain boundaries range from approximately 20 to 400. The highest values have been evaluated at the reservoir walls, where particular accuracy is not required considering the purpose of this work. A grid independence study has not been included in this work, because the mesh size has been chosen according to the author's experience in similar computational studies performed on scroll machines. Furthermore, in these applications the number of radial divisions of the mesh is constrained by the flank gap size: increasing the number of cells results in higher aspect ratios of the cells in correspondence of the flank gap.

6.2.1 Numerical schemes and boundary conditions

Fully turbulent adiabatic simulations employing Menter's k-ω SST model with updated coefficients have been performed. A second-order discretization scheme has been applied to spatial and time-dependent terms, with the exception of turbulent quantities. Furthermore, gradient limiters have been necessary to ensure the stability of the analyses.

The boundary conditions imposed for the full domain cases include fixed static pressure at inlet and outlet and inflow conditions based on specified mixing length for turbulence specific dissipation. The turbulent kinetic energy is evaluated at inlet and outlet, in case of inflow, according to a user-supplied turbulence intensity value. Temperature values have

been imposed in presence of flows entering the domain, while zero gradient conditions have been applied to the outflows. It is particularly important to take care of reverse flow both at inlet and outlet because it is an inherent phenomenon in positive displacement machines, especially in the case of under compression. Accordingly, the velocity boundary conditions have been set as follows: for the flow leaving the domain, a zero gradient condition has been applied. On the other hand, for the flow entering in the domain a velocity value based on the flux in the patch-normal direction has been imposed. Lastly, some simulations have been performed with a modified discharge region, with no reservoir, to improve the convergence. In this case, the outlet boundary conditions on velocity and pressure have been replaced with the *OpenFOAM* native implementation of non-reflective boundary conditions.

6.2.2 Validation

The pressure trends during the compression process are very well captured for all the operating conditions. In this work, the *direct* chamber is the compression chamber that firstly opens towards the discharge port, while *indirect* refers to the other. In figures 6.3, 6.4, 6.5, *pDirect* and *pIndirect* refer to the pressure recorded in the direct and indirect chambers. *pSuction* is the pressure recorded by a probe in the suction region, while *pDischarge* has been evaluated in the discharge region. Lastly, *pExDir* and *pExInd* are the experimental trends collected by Picavet et al. [130], respectively for the direct and indirect chamber.

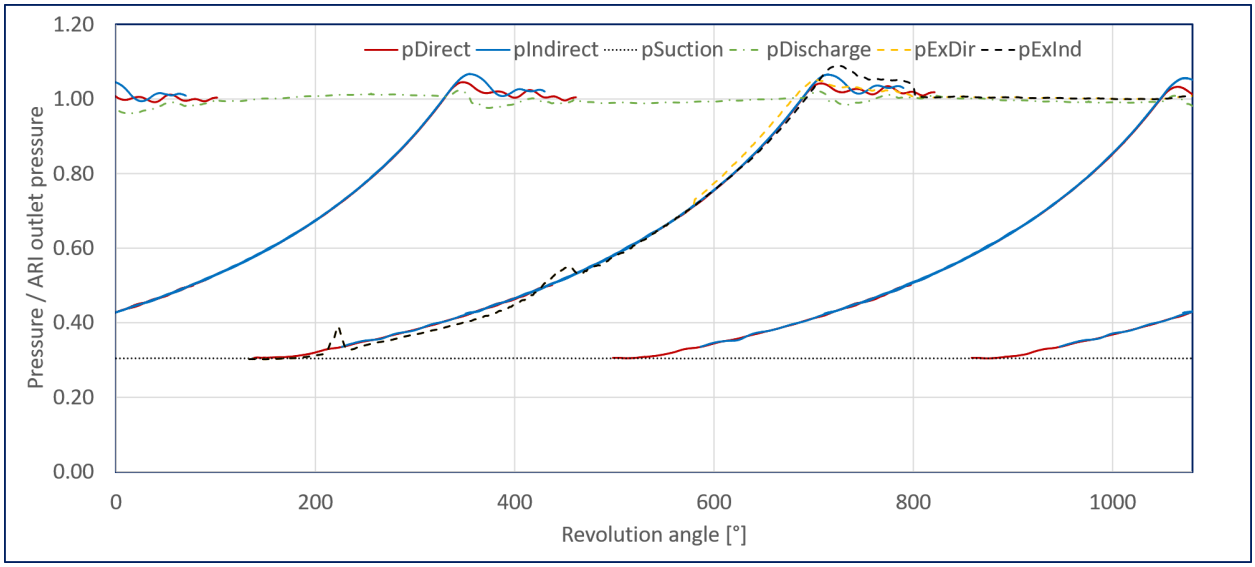

Figure 6.3: Danfoss compressor: pressure trends validation, *ARI*, [55].

ARI: the pressure trend (figure 6.3) is accurately reproduced, especially in the second half of the compression process. There is a small overestimation of the two peaks that occur in the discharge phase. This difference is probably due to the absence of tip seals in the final part of the scroll wrap (not modelled in this work), as reported in [130].

Low pressure ratio: The most interesting aspect of the low pressure ratio trend (figure 6.4) is related to the expansion process corresponding to the opening of the compression chamber. The discharge pressure experiences a fast decrease before stabilizing again at the outlet pressure levels. In this case, the peaks of the simulated trends are higher than the experimental data.

High pressure ratio: The under-compression generates reverse flow as the discharge port opens (figure 6.5). The consequent pressure peaks are very well captured by the numerical simulation. This validation is important as it is not highly influenced by the gap sizes. On the other hand, underestimation of the pressure values can be seen in the final part of the compression. The higher pressure ratio amplifies the effects of the modelling assumptions described in section 2.3.1.

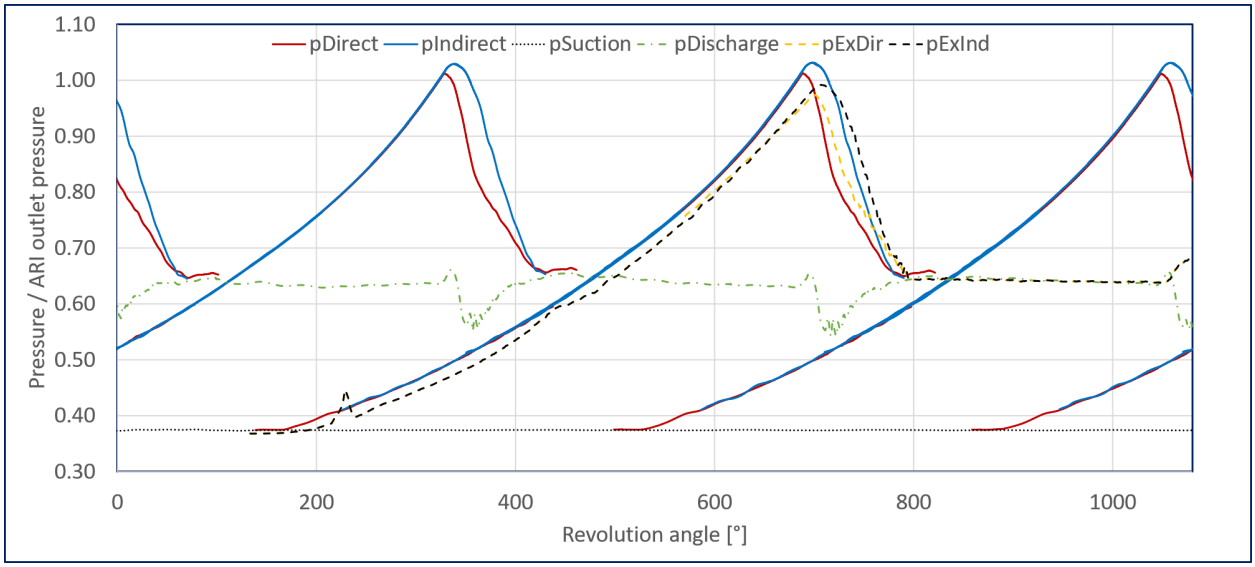

Figure 6.4: Danfoss compressor: pressure trends validation, low PR, [55].

6.2.3 Performance with varying pressure ratio

	$\dot{m}_{in}/\dot{m}_{in,ARI,OF}$	$\dot{m}_{out}/\dot{m}_{in,ARI,OF}$	$\dot{m}_{out}/\dot{m}_{in}$	η_v	η_{forces}
ARI	1.0	1.017	1.017	0.967	0.861
High *PR*	0.381	0.396	1.039	0.941	0.766
Low *PR*	1.214	1.213	0.9991	0.975	0.694
ARI NR	1.002	1.005	1.003	0.969	0.864
ARI NR 100 µm	0.941	0.948	1.007	0.910	0.833

Table 6.1: Revolution-averaged mass flow rate, mass imbalance and volumetric and pV efficiencies, OpenFOAM. (NR = No Reservoir, OF = OpenFOAM).

At first, the effects of under and over-compression are reflected in the volumetric efficiency of the compressor, as reported in table 6.1. The high *PR* case is characterized by a reduction

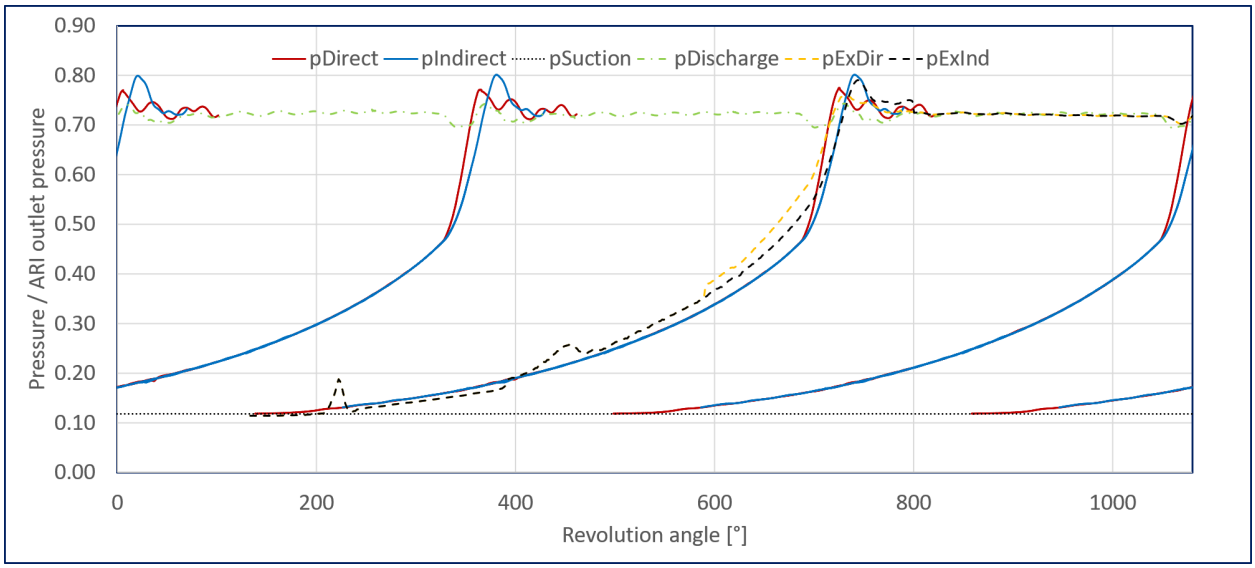

Figure 6.5: Danfoss compressor: pressure trends validation, high PR, [55].

of the volumetric efficiency close to 2.5 %, due to the increased leakages mass flow rate. Overall, the compressor shows good volumetric performance, even in presence of strong variations in the pressure ratio.

The average mass flow rate elaborated by the compressor in the high PR case is more than 50 % lower with respect to the ARI point. The main reason is related to the different density of the fluid corresponding to the inlet conditions. This information can be deducted by the value of the volumetric efficiency, which remains close to 95 % even when the machine is subjected to a PR that is 83 % higher. Similarly, the mass flow rate corresponding to the lower PR case is more than 20 % higher than the ARI's one.

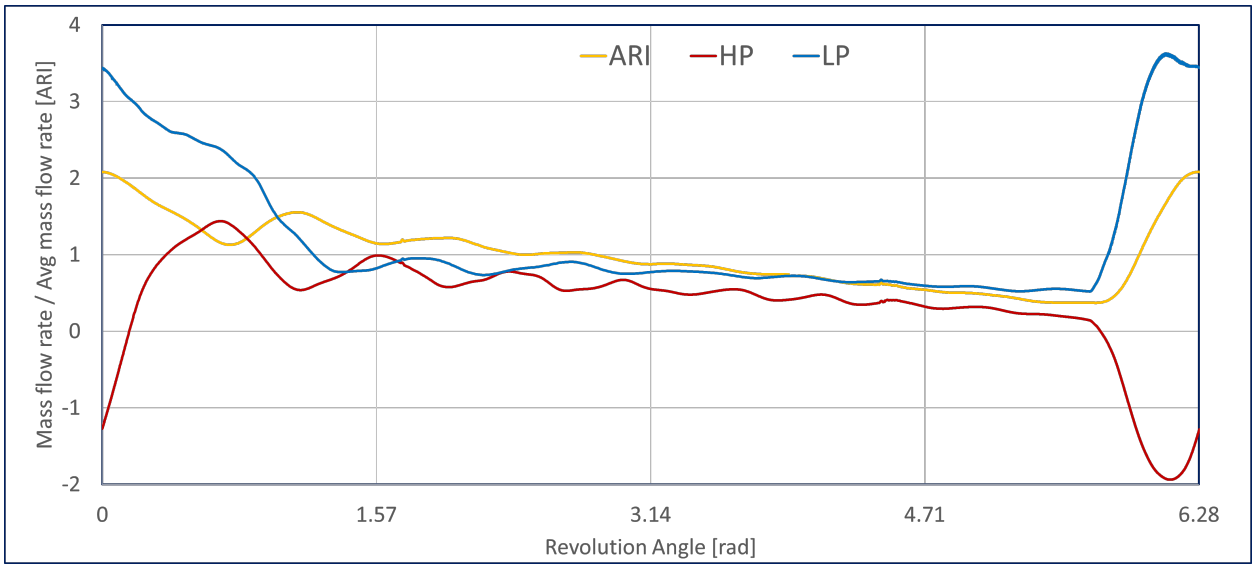

Figure 6.6: Danfoss compressor: scroll outlet mass flow rate comparison.

The trends of the mass flow rate at the outlet of the scroll compressor are reported in figure 6.6, where all the values have been divided by the average value of the mass flow

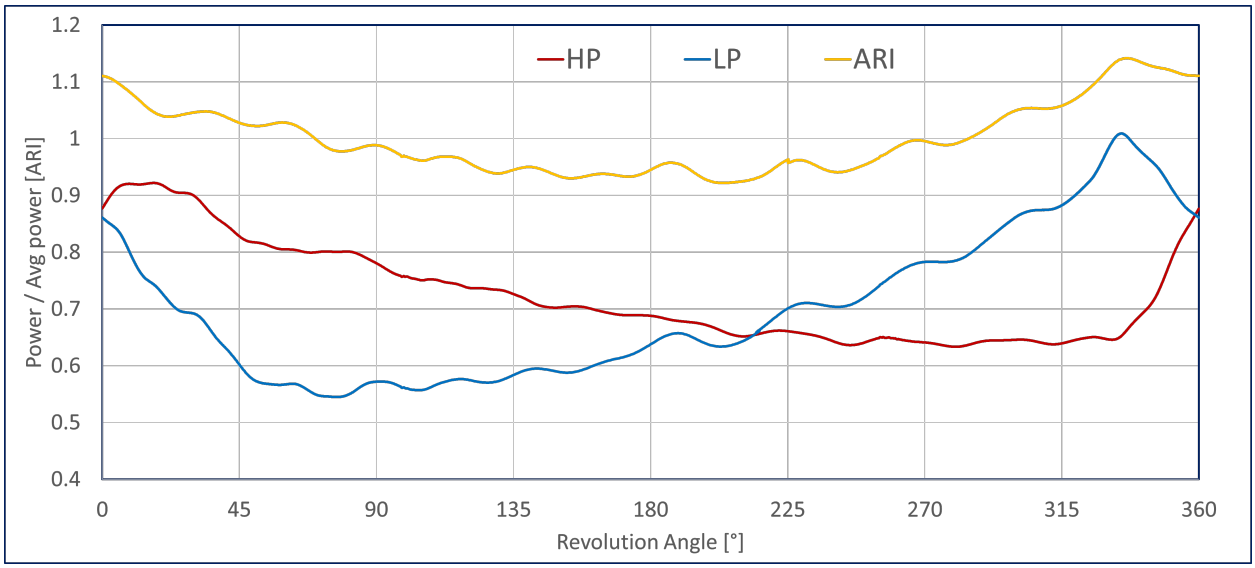

Figure 6.7: Danfoss compressor: power consumption comparison.

rate at *ARI* conditions. The smoothness of the discharge process at the design point (*ARI*) is clearly highlighted by the correspondent curve, which shows a moderate peak after the discharge angle. The same peak is definitely higher for the low *PR* case, while is reversed when a negative peak is recorded when the *PR* is higher than the design specifications.

The power consumption of the three cases is compared in figure 6.7. The high *PR* case reaches the maximum power consumption in correspondence with the maximum values of reverse flow. On the contrary, the low *PR* and *ARI* conditions show a peak right before the discharge process. Generally speaking, the two off-design conditions consume a definitely smaller amount of power, but table 6.1 shows that their pV efficiency is consistently lower than the *ARI*'s one. In fact, the high *PR* condition is characterized by a lower mass flow rate, while the low *PR* case shows a consistent reduction of the enthalpic jump between inlet and outlet conditions.

6.2.4 Reservoir and convergence

It is interesting to notice how the presence of the reservoir generates an imbalance between the inlet and outlet mass flow rate. The reason is clearly represented in figure 6.8, where the different periodicity of the mass flow rate trend at the domain outlet (*Outlet*) is highlighted. The pressure waves that produce this mass flow rate trend are influencing also the region in proximity of the scroll outlet (*maxZ*), increasing the time needed to reach an acceptable level of convergence. These issues are the main reasons behind the decision of performing an additional simulation with no reservoir. Regarding the pressure values in the compression chambers, the absence of the reservoir does not produce significant variations (figure 6.10). Conversely, the removal of the reservoir has a beneficial effect on the global conservation of

the mass flow rate. Table 6.1 highlights a consistent reduction (from 1.6 % to 0.3 %) in the difference between the suctioned and discharged mass flow rate over a complete revolution of the machine. The trends of the mass flow rate of the simulation without reservoir is reported in figure 6.9. The low-frequency oscillations in the mass flow rate trend recorded at the domain outlet have been completely removed by eliminating the reservoir.

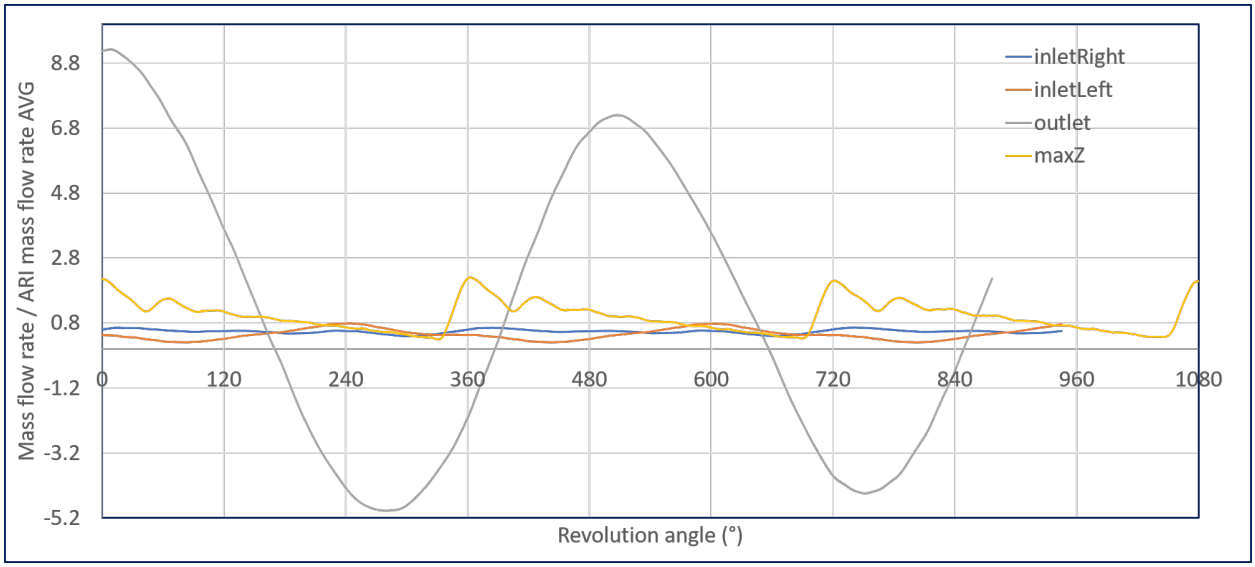

Figure 6.8: Danfoss compressor: domain outlet mass flow rate, *ARI*.

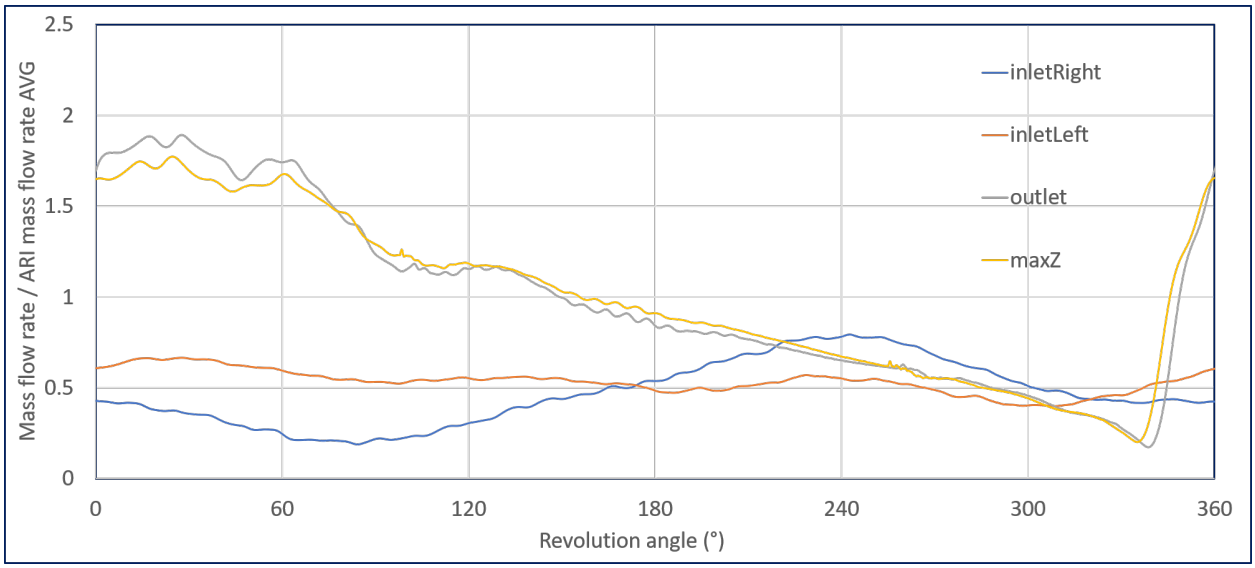

Figure 6.9: Danfoss compressor: domain outlet mass flow rate, *ARI*, no reservoir.

6.2.5 Gap size effects

The determination of the flank gap size leading to the most accurate solution is certainly a challenging task. The first analysis conducted in this section regards the flank gap size:

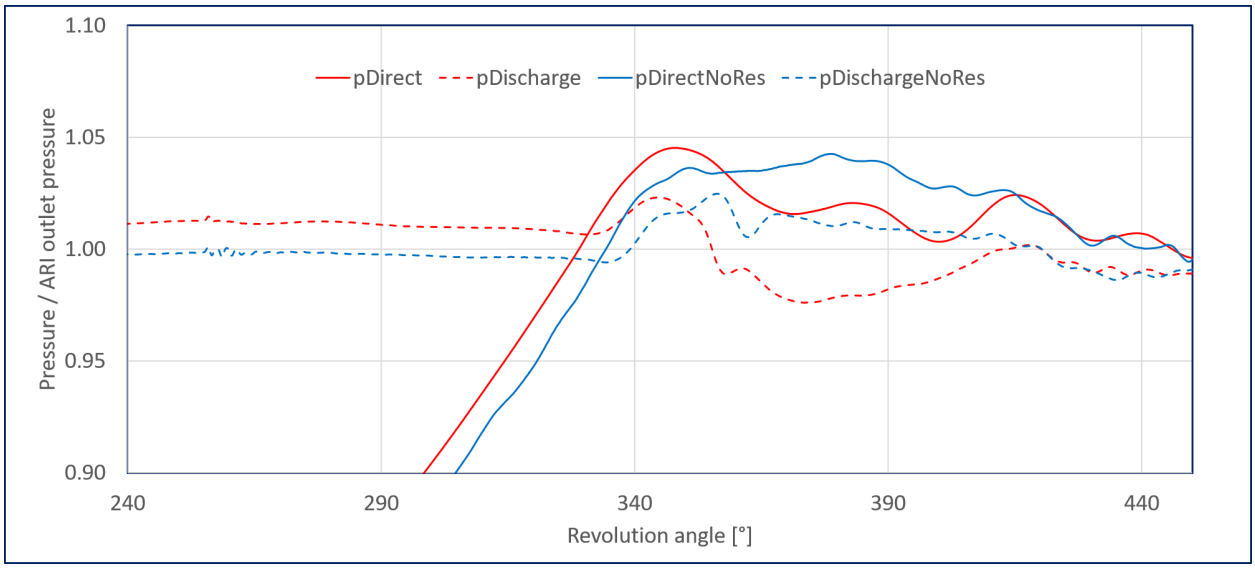

Figure 6.10: Danfoss compressor: discharge pressure trends, *ARI*, no reservoir.

starting from the simulation with no reservoir, the distance between the two spirals has been increased from 60 µm to 100 µm.

The comparison between figure 6.11 and figure 6.3 shows that the value of 60 µm produces a solution that is closer to the experimental reference. However, the low pressure ratio and high pressure ratio trends show that there is still room for improvement, probably in the area of the tip region modelling.

It is important to underline that the introduction of axial gap modelling requires additional interfaces, which would be placed in regions where cells with high aspect-ratio are needed.

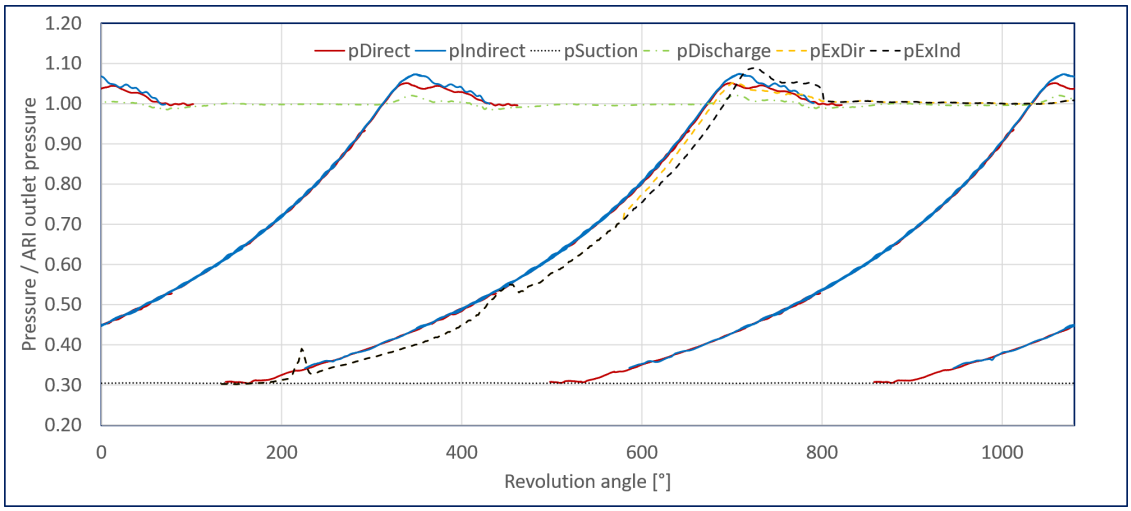

Figure 6.11: Pressure trends as functions of the revolution angle, *ARI*, no reservoir, 100 µm [55].

6.2.6 3D flow features in scrolls

The contour of the velocity magnitude is represented in figure 6.12 at four different orbital positions. It is interesting to notice the reduction of the velocity of the fluid trapped in the compression chambers during the orbiting motion. The outermost chamber is characterized by the higher velocity, with the only exception of the discharge region when the last compression chamber opens towards the outlet port.

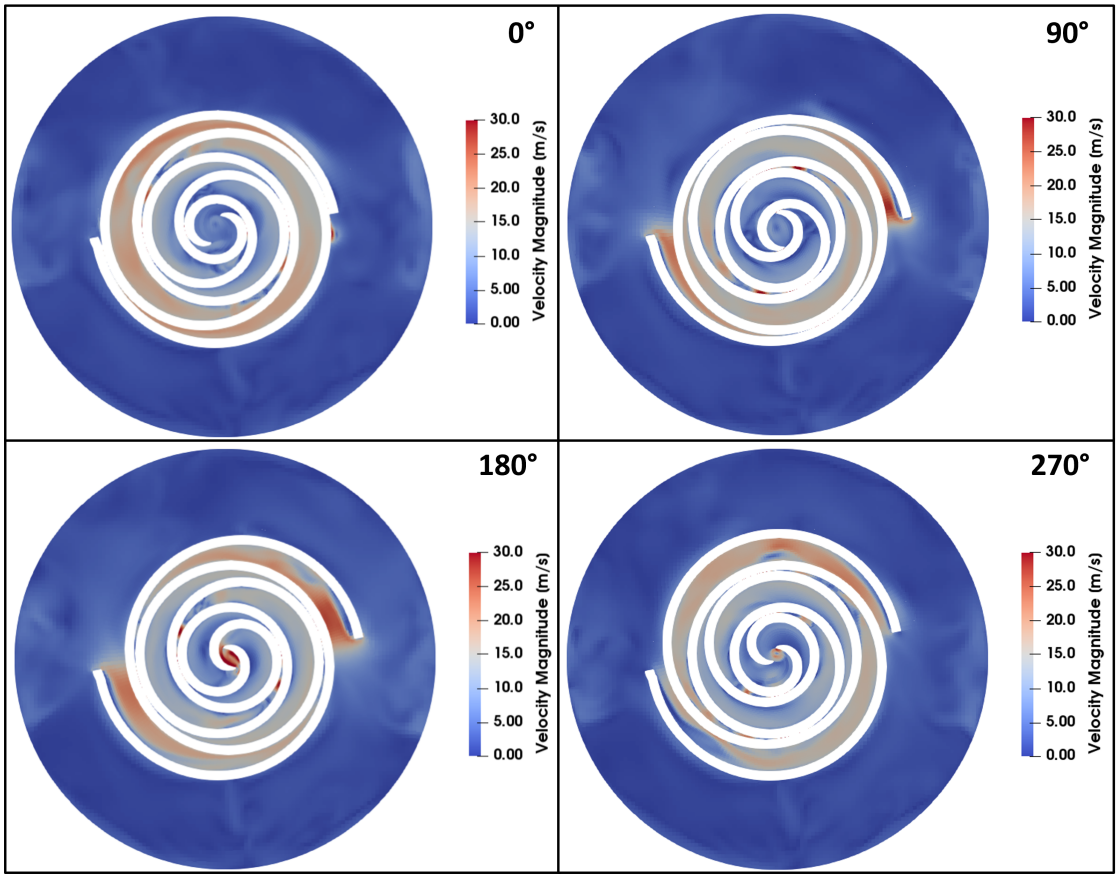

Figure 6.12: Contour of the velocity magnitude at different orbit angles, *ARI*

Suction process

The suction domain of the test case compressor is constituted by two inlet channels, where an asymmetric behaviour is recorded. The velocity in the channel placed in correspondence of the direct chamber reaches higher values, resulting in a 10 % increase of the mass flow rate with respect to the one measured in the channel corresponding to the indirect chamber. This effect is represented in figure 6.13, where a pressure contour has been added to highlight the presence of lower pressure in the direct suction chamber. Consequently, a higher pressure difference between this chamber and the external volume produces higher velocities in the right-side inlet channel.

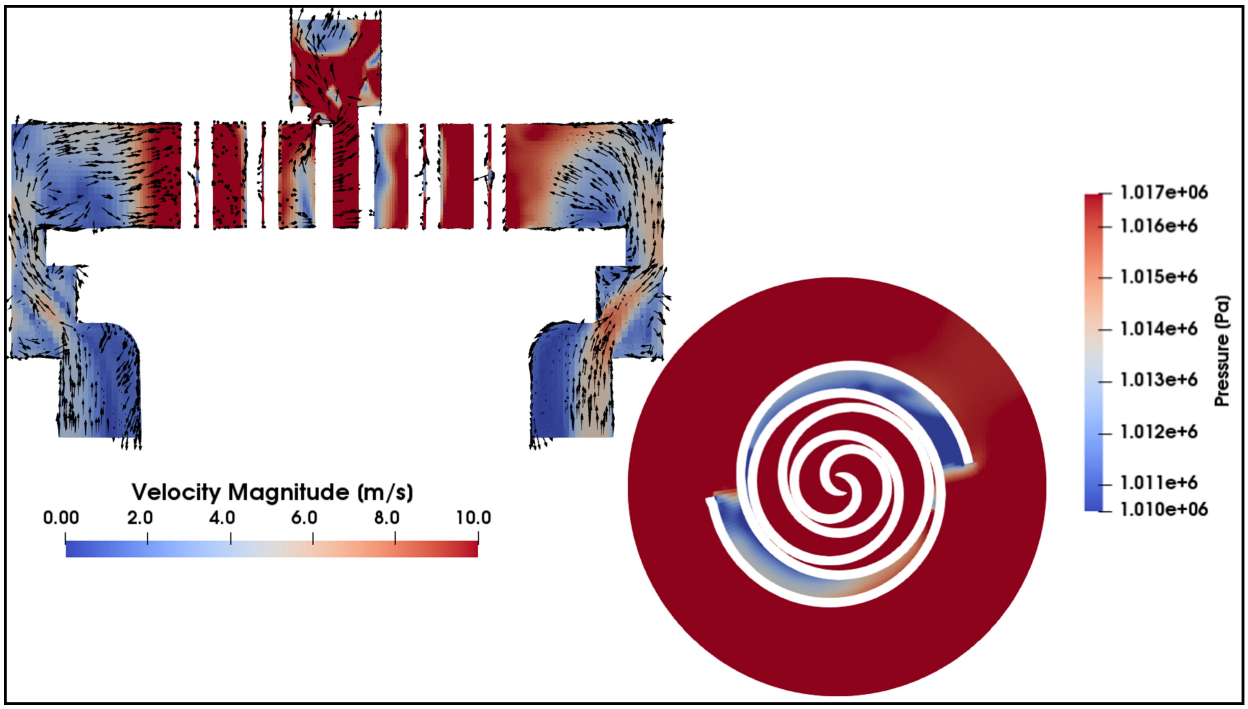

Figure 6.13: Contour of the pressure and of the velocity magnitude during the suction process.

Discharge process

The discharge process is firstly represented in the contour of the velocity magnitude (figure 6.14). There are several fluid dynamics phenomena to be highlighted: in the *ARI* case, the separation zone downstream of the main outlet duct is clearly visible on the left. This phenomenon is strongly amplified when a lower pressure ratio is imposed between outlet and inlet, leading to a jet flow that occurs when the compression chambers open.

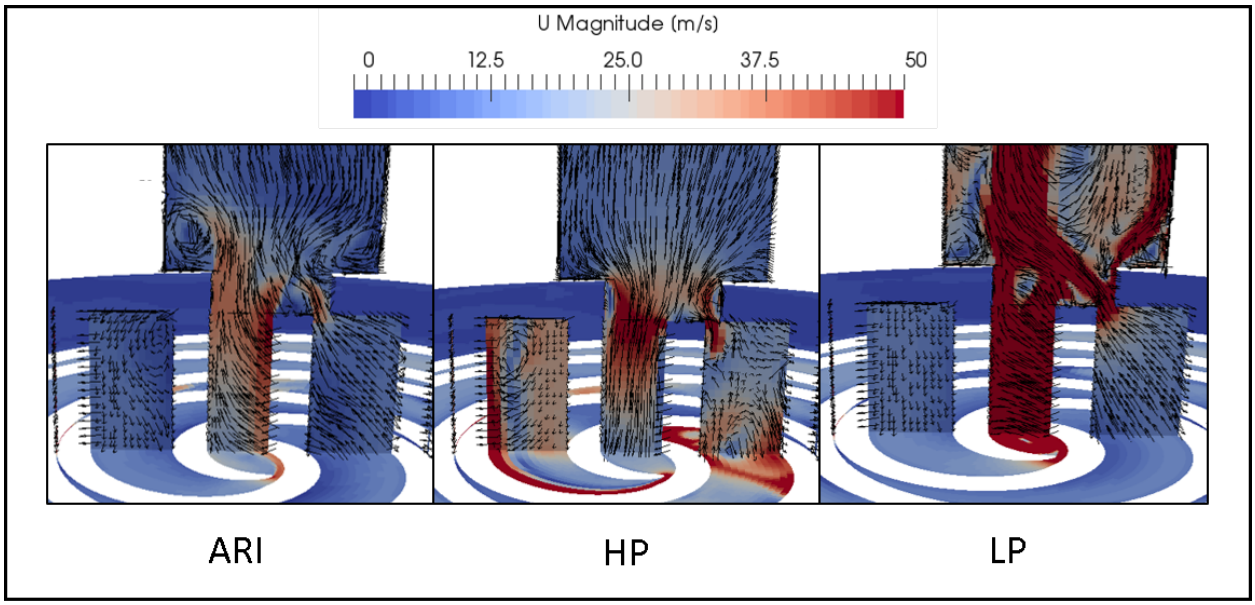

Figure 6.14: Contour of the velocity magnitude during the discharge process [55].

Lastly, the high pressure ratio case is characterized by a large amount of reverse flow, which enters in the scroll domain influencing also the upstream chambers.

An accurate representation of the fluid dynamics of the discharge process is one of the most difficult results to obtain without using *CFD* tools. Chamber models may fail in correctly predicting the mass flow rate and pressure trends in the discharge region because the representation of such a complex process using exclusively control volumes and flow path is not trivial.

6.3 PDSim results

The three operating conditions presented in section 6.1 have all been simulated using the simplified chamber model of the PDSim project. These simulations are characterized by a smaller difference between the trends of the pressure recorded in the direct and indirect chambers. When the last compressor chambers open towards the discharge region, the time required to reach a pressure equilibrium appears to be underestimated by the PDSim models. This phenomenon is clearly visible in all three operating conditions (Figures 6.15, 6.16 and 6.17), where the disequilibrium between the two chambers is smoothed roughly 100° before the experimental reference. On the contrary, the OpenFOAM results reported in figures 6.3, 6.5 and 6.4 offer a definitely more accurate representation of the discharge process.

	$\dot{m}_{in}/\dot{m}_{in,ARIOF}$	$\dot{m}_{out}/\dot{m}_{in,ARIOF}$	$\dot{m}_{out}/\dot{m}_{in}$	η_v	η_{forces}
ARI	0.993	0.992	0.999	0.950	0.886
High *PR*	0.365	0.396	1.003	0.920	0.789
Low *PR*	1.231	1.229	0.998	0.964	0.692
ARI 100 µm	0.944	0.945	1.001	0.904	0.851

Table 6.2: Revolution-averaged mass flow rate, mass imbalance, volumetric and pV efficiencies, PDSim. (OF = OpenFOAM).

	$\Delta\dot{m}_{in}$ %	$\Delta\dot{m}_{out}$ %	$\Delta Imbalance$ %	$\Delta\eta_v$ %	$\Delta\eta_{forces}$ %
ARI	0.7 %	2.5 %	1.8 %	1.8 %	2.82 %
High *PR*	4.2 %	0.0 %	3.5 %	2.2 %	2.92 %
Low *PR*	1.4 %	1.4 %	0.1 %	1.1 %	0.3 %
ARI 100 µm	0.3 %	0.3 %	0.6 %	0.7 %	2.1 %

Table 6.3: Percent error of revolution-averaged performance indicators, difference between OpenFOAM and PDSim. ($\dot{m}$ = Mass Flow Rate).

Excluding the discharge process, the pressure trends are very well captured by the PDSim simulations. Furthermore, the chamber models show accurate results also from the quantitative point of view: this is schematized in tables 6.3 and 6.2. In general, PDSim shows better values in terms of mass imbalance: this is due to the presence of the reservoir in

the *OpenFOAM* simulations. For this reason, the 100 µm case is characterized by a smaller difference in the mass imbalance because of the absence of the reservoir both in the PDSim and *OpenFOAM* simulations. The difference in the performance indicator (volumetric efficiency and pV efficiency) is very small, recording a maximum of 2.92 % for the pV efficiency of the high *PR* case. These results confirm the excellent reliability of both the simulation tools employed in this thesis, especially considering the comparison with the experimental pressure trends.

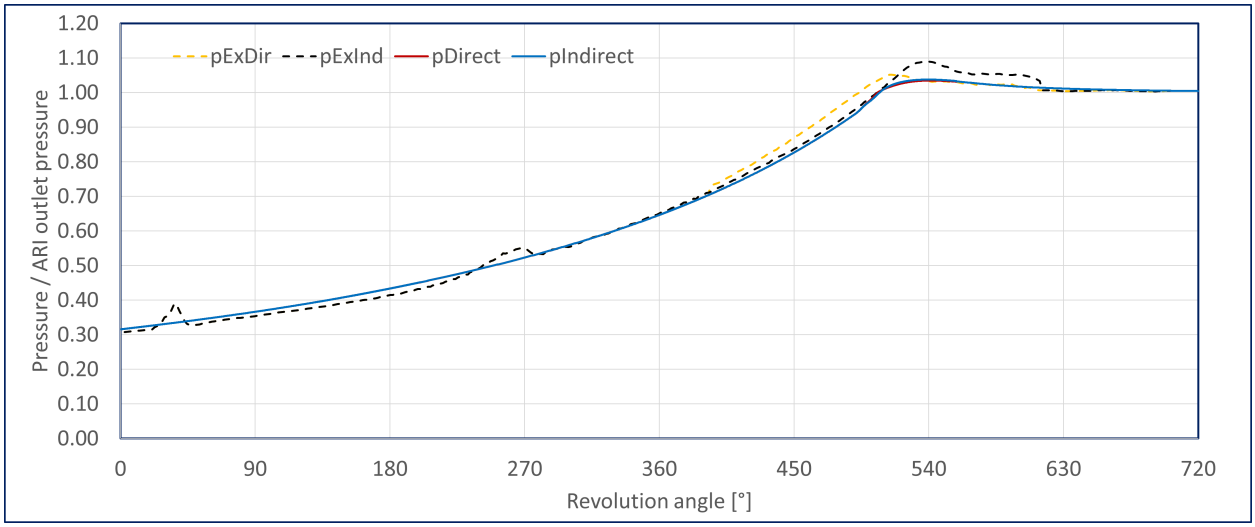

Figure 6.15: Danfoss compressor: PDSim pressure trends validation, *ARI*.

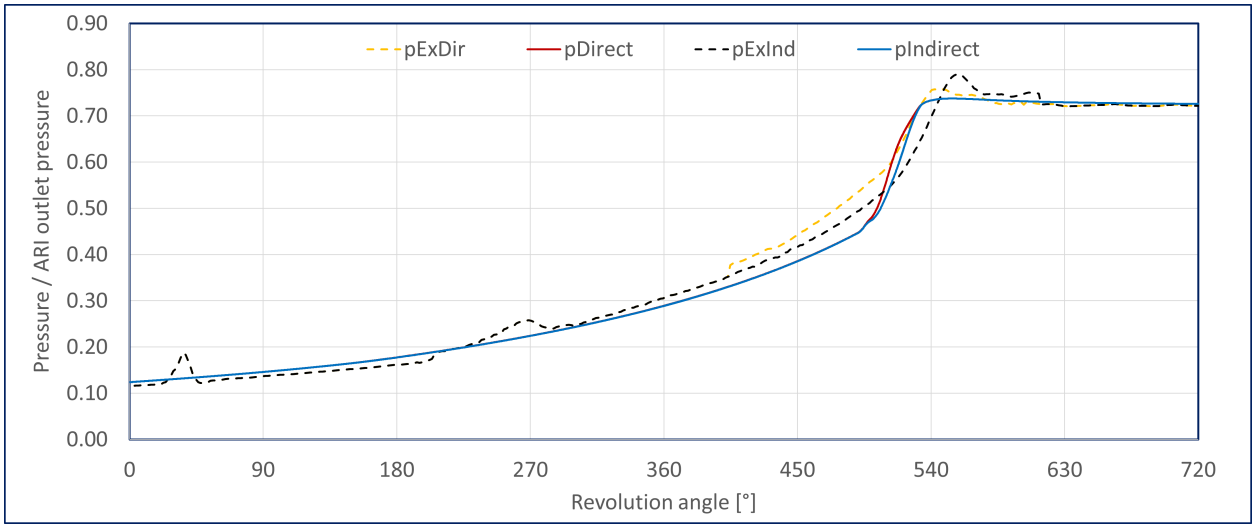

Figure 6.16: Danfoss compressor: PDSim pressure trends validation, high *PR*.

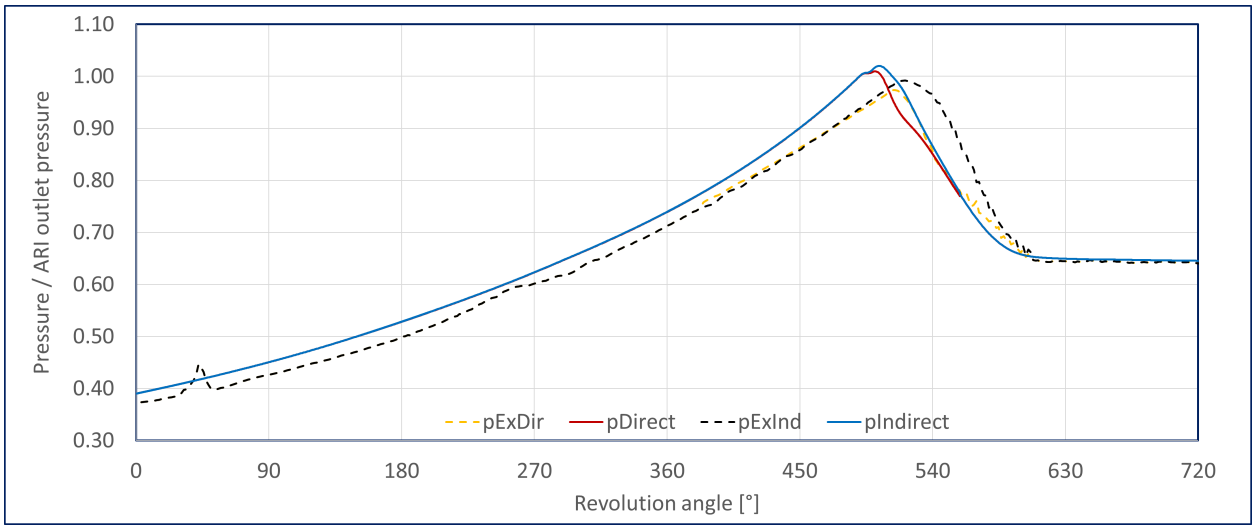

Figure 6.17: Danfoss compressor: PDSim pressure trends validation, low *PR*.

The limitations of PDSim, and chamber models in general, are highlighted in figure 6.18, where the mass flow rate trends are compared. As soon as the last compression chamber open towards the discharge region, an unusual instability is recorded in the PDSim mass flow rate. A small reverse flow peak is followed by numerical oscillations of the outlet flow rate. On the contrary, all the other oscillations highlighted by the OpenFOAM simulation are smoothed down by the *0-D* model.

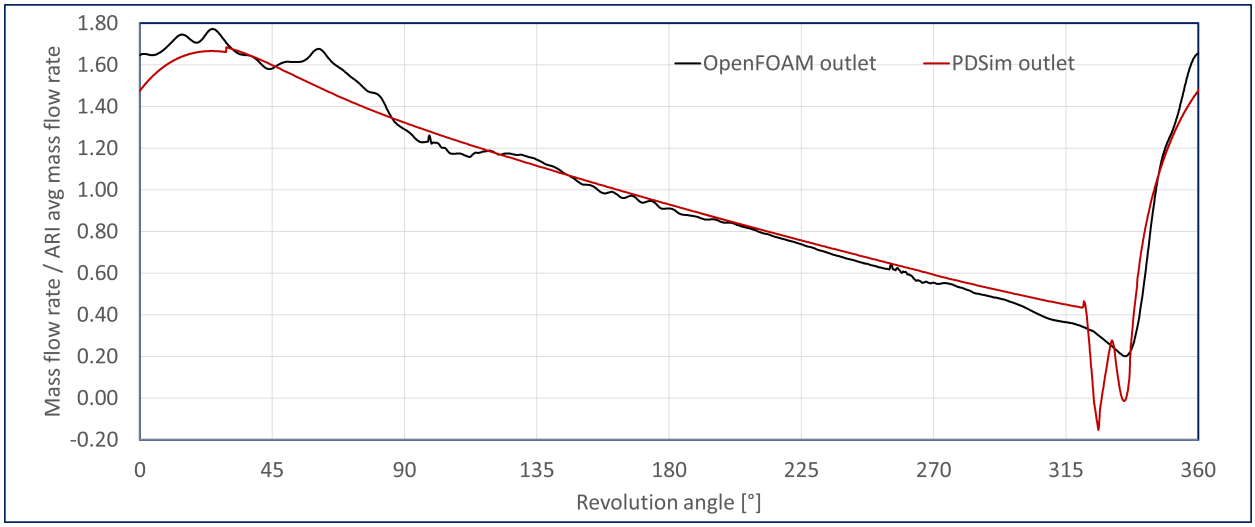

Figure 6.18: Danfoss compressor mass flow rate: OpenFOAM vs PDSim comparison, *ARI*.

The precise matching of the pressure trends of both the simulations with the experimental data is confirmed by figure 6.19, where the trends of the forces are reported. The forces acting on the orbiting scroll, used to determine the power transferred to the fluid, are characterized by an almost identical trend. Since these trends are a direct consequence of the pressure evolution during the compression process, this graph serves as an additional validation of the simulation codes.

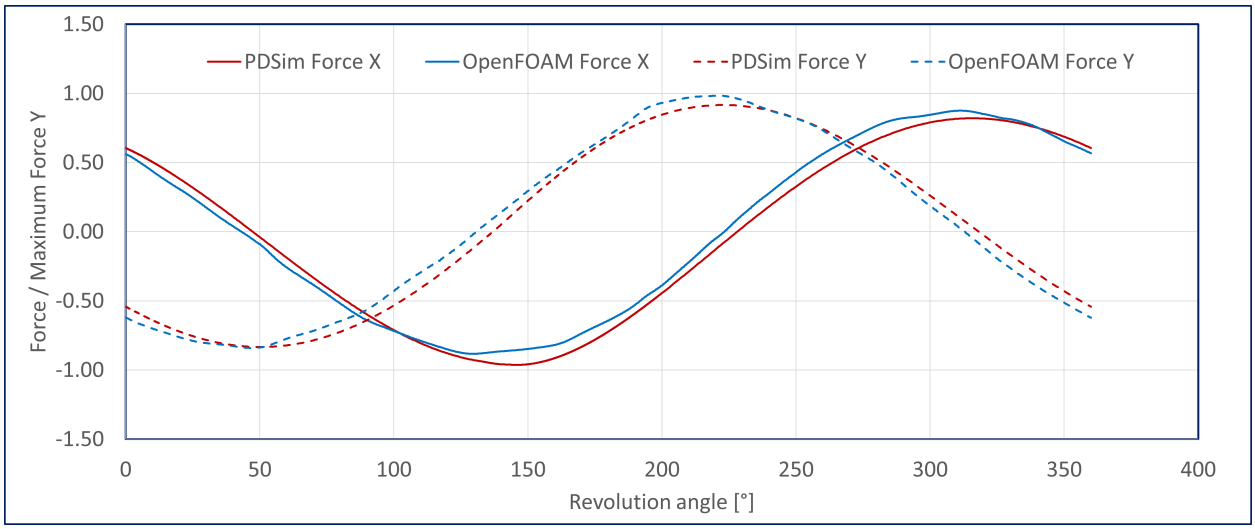

Figure 6.19: Danfoss compressor forces: OpenFOAM vs PDSim comparison, *ARI*.

6.4 Conclusions

The author has presented the first open-source simulation of a commercial scroll compressor, complete with experimental validation. This achievement could represent a starting point for including new modelling options in the field of positive displacement machines *CFD*. In fact, open-source frameworks are particularly suitable for the implementation of multiphase models, studies on heat transfer or optimization procedures.

The post-processing highlights the importance of *CFD* in the analysis of off-design conditions characterized by over and under-compression phenomena. The fluid dynamic behaviour of the compressor during the discharge processes can be analyzed at different operating points, with the possibility of extracting loss coefficients that can be adopted in reduced-order models.

Additionally, the flank gap size has been the object of a preliminary analysis, with the aim of evaluating the variations of the pressure trends in the compression chambers, as well as the reduction in the volumetric efficiency.

The *CFD* results have also been compared with quasi-static analyses performed with PDSim. The limitations of low-order models in the investigation of the discharge process have been highlighted. However, the general trends of the compression process are very well captured by both the numerical tools.

Chapter 7

Open-source optimization of a variable thickness scroll compressor

In this chapter, an optimization process based on the kriging response surface method is presented. A constant thickness scroll operating in under-compression conditions has been substituted by an optimized variable thickness scroll, with a consistent reduction of the costs. The optimization has been performed using the results of PDSim simulations as collected data. Lastly, the final geometry has been simulated with OpenFOAM, adding a sensitivity analysis of the gap size effects.

7.1 Kriging

Kriging, also known as Gaussian Process Regression, is a method of spatial interpolation originally developed in the geostatistics field [41, 140]. This method, as well as other *Response Surface Methods (RSMs)*, is not properly an optimizer but represents a regression tool to perform optimization by substituting direct and expensive calls to expensive simulation methods with cheap calls to a surrogate model of the simulation method.

Especially in the first decade of the 00s, several researchers have been focusing on the application of *RSMs* to optimization processes for computer-based experiments [64, 65, 73, 84]. One of the main advantages of kriging is the possibility of iteratively adding new evaluation points to an initial DOE to refine the *Response Surface Method (RSM)* during an optimization process. Moreover, the kriging model is able to deal with complex functions and return error evaluations.

The kriging *RSM* is initially based on a starting set of sampled data, which can be planned with *Design of Experiments (DOE)* techniques such as the *Latin Hypercube Sampling (LHS)*, which is employed in this work. The main structure of the kriging predictor is based on a mean term $\hat{\mu}$, where the circumflex indicates a *MLE*, and a sum of n basis functions Ψ

centred around the n sampled points:

$$\hat{y}(\mathbf{x}_{n+1}) = \hat{\mu} + \sum_{i=1}^{n} b_i \Psi_i(\|\mathbf{x}_{n+1} - \mathbf{x}_i\|) \tag{7.1}$$

The basis functions are based on the correlation between the sampled points and a random variable at the new point of interest, $\mathbf{x}_{n+1}$:

$$\mathbf{\Psi} = \begin{pmatrix} Corr\left[Y(\mathbf{x}_{n+1}), Y(\mathbf{x}_1)\right] \\ \vdots \\ Corr\left[Y(\mathbf{x}_{n+1}), Y(\mathbf{x}_n)\right] \end{pmatrix} = \begin{pmatrix} exp\left[-\sum_{j=1}^{k} \hat{\theta}_j (\|x_{n+1} - x_{1,j}\|)^{\hat{p}_j}\right] \\ \vdots \\ exp\left[-\sum_{j=1}^{k} \hat{\theta}_j (\|x_{n+1} - x_{1,j}\|)^{\hat{p}_j}\right] \end{pmatrix} \tag{7.2}$$

The hyper-parameters $\hat{p}$ and $\hat{\theta}$ are fitted by means of an optimization procedure that maximize the likelihood of the predictor. In general, $\hat{p}$ is a measure of the smoothness of the function approximation, and a value equal to 2 means that the basis function is infinitely differentiable through a sample point. On the other hand, $\hat{\theta}$ is a measure of the variance of the basis function: it determines how fast the function changes when the new point moves away from the reference sample point.

The values of the constants b_i are calculated according to the following column vector:

$$\mathbf{b} = \mathbf{R}^{-1}(\mathbf{y} - \mathbf{1}\hat{\mu}) \tag{7.3}$$

Where $\mathbf{R}$ is a matrix of correlations between the sampled data, $\mathbf{y}$ is a column vector of the sampled data and $\mathbf{1}$ is the unity column vector. The MLE of the mean is calculated as follows:

$$\hat{\mu} = \mathbf{1}^T\mathbf{R}^{-1}\mathbf{y}/\mathbf{1}^T\mathbf{R}^{-1}\mathbf{1} \tag{7.4}$$

Following the first definition of the kriging predictor, it is possible to improve the accuracy of the *RSM* by refining the surface with additional data in regions where there is the maximum probability of finding a new maximum/minimum. The infill criterion is based on the equilibrium between a global exploration of the surface, which would be only based on the kriging error $\hat{s}^2$, and a local exploitation of the current predictor $\hat{\mathbf{y}}$. Every time a new point is added to the set of known data, the kriging predictor is rebuilt with newly optimized hyper-parameters, and eventually, a new point is infilled. The kriging error can be calculated as:

$$\hat{s}^2(\mathbf{x}_{n+1}) = \hat{\sigma}^2(1 - \mathbf{\Psi}^T\mathbf{R}^{-1}\mathbf{\Psi}) \tag{7.5}$$

Where:

$$\hat{\sigma}^2 = (\mathbf{y} - \mathbf{1}\hat{\mu})^T\mathbf{R}^{-1}(\mathbf{y} - \mathbf{1}\hat{\mu})/n \tag{7.6}$$

The value of the function at $\mathbf{x}$ is treated as a stochastic process with a mean given by

the predictor $\hat{y}(\mathbf{x})$ and the variance given by the kriging error:

$$\frac{1}{\sqrt{2\pi}\hat{s}(\mathbf{x})} exp - \frac{1}{2}\left(\frac{Y(\mathbf{x}) - \hat{y}(\mathbf{x})}{\hat{s}(\mathbf{x})}\right)^2 \tag{7.7}$$

$\hat{y}(\mathbf{x})$ is the most probable value at $\mathbf{x}$, but it is not certain as the variance related to the kriging error $\hat{s}^2$ is introduced.

The expectation of the new infill candidate being an improvement on the current minimum can be expressed as:

$$E\left[I(\mathbf{x})\right] = \int_{-\infty}^{\infty} max(f_{min} - Y(\mathbf{x}), 0)\xi(Y(\mathbf{x}))dY \tag{7.8}$$

And, solving the integral:

$$E\left[I(\mathbf{x})\right] = \begin{cases} \left[f_{min} - \hat{y}(\mathbf{x})\right] \boldsymbol{\Xi}\left(\frac{f_{min} - Y(\mathbf{x})}{\hat{s}(\mathbf{x})}\right) + \hat{s}\xi\left(\frac{f_{min} - Y(\mathbf{x})}{\hat{s}(\mathbf{x})}\right) & \text{if } \hat{s} > 0 \\ 0 & \text{if } \hat{s} = 0 \end{cases} \tag{7.9}$$

Where $\boldsymbol{\Xi}$ and ξ are the normal cumulative distribution function and the probability density function, respectively.

The maximum *Expected Improvement (EI)* is the criterion chosen by the author to detect the new points to be added to the sampled data during the optimization process.

7.2 Test case

The optimization procedure described in section 7.1 has been applied to a scroll compressor employed in low-temperature air-source heat pumps. Bell [17] introduced a similar test case in an optimization example of liquid-flooded scroll compressors, where a theoretical pressure ratio of 7.9 was needed. Reaching high volume ratios with constant thickness requires the construction of expensive machines, because of the increased machining cost and leakage losses due to the increased length of the scroll wraps. For this reason, he suggested that the employment of variable thickness scroll geometries might allow reaching higher volume ratios in compact form factors.

From a theoretical point of view, variable thickness scrolls allow reaching the same volume ratios of constant thickness geometries due to the shorter angular length of the spirals. Consequently, this kind of machines is characterized by smaller machining costs and, possibly, reduced leakage losses. Bell [17] stated that both the efficiency and the difficulty of manufacturing increase with the volume ratio in presence of under-compression losses. For this reason, he indicated a volume ratio of approximately 4 as a reasonable compromise, especially considering that a volume ratio of 4 would not differ significantly from the values

currently available on the market.

In this section, the author has designed a constant thickness scroll machine with a built-in volume ratio of 4. This constant thickness compressor has been taken as a reference to run a kriging optimization procedure to determine the best variable thickness geometry for the under-compression operating conditions taken from [17]. The resulting geometry, characterized by the same displacement of the initial compressor, has been finally simulated with *OpenFOAM* to validate the optimization results and analyze the details of the fluid dynamics.

7.2.1 Constant thickness geometry

The geometrical parameters of the reference geometry are reported in table 7.1.

$\mathbf{r_b}$	$\boldsymbol{\phi_e}$	$\boldsymbol{\phi_{os}}$	$\boldsymbol{\phi_{is}}$	$\boldsymbol{\phi_{i0}}$	**Rot. speed**
0.002 51 m	28.955 rad	0.9 rad	π+0.9 rad	0.0 rad	2900 *rpm*
Width	**Discharge**	**t**	**Flank gap**	**Axial gap**	**Fluid**
0.0256 m	2Arcs, $r_2 = 0.001$ m	0.003 m	15 µm	15 µm	R410a

Table 7.1: Optimization reference compressor: geometrical parameters.

The main parameters of the scroll, such as basic radius, width and ϕ_e, have been retrieved with a minimization of the theoretical leakage area, imposing the wrap thickness according to [17]. The discharge region has been designed to guarantee a smooth outflow during the operation of the compressor.

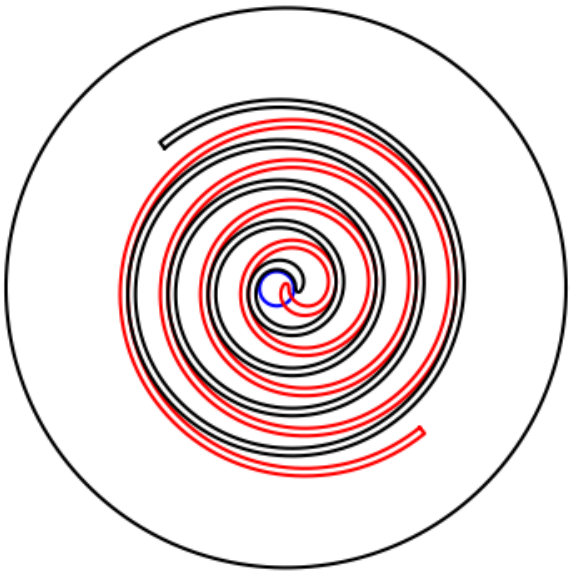

Figure 7.1: Optimization starting geometry: constant thickness.

This constant thickness reference geometry (Figure 7.1) is characterized by a displacement of the compressor is 98 cm^3 and a high number of windings to reach the objective volume ratio of 4. It has to be observed that this geometry represents a limit case in the scenario of commercial scroll compressors: the number of windings is high, as well as the volume ratio, resulting in significant machining cost and a more complex structural design of the compressor. Moreover, the length of the spiral enhances the leakage losses, especially if the gap size is increased during the manufacturing process.

The operation of the machine has been simulated with PDSim, and the results are reported in table 7.2.

$\dot{\mathbf{m}}$	$\eta_{\mathbf{v}}$	$\eta_{\mathbf{forces}}$	$\dot{\mathbf{W}}_{\mathbf{forces}}$
0.042 12 kg s^{-1}	0.917	0.826	4.382 kW

Table 7.2: Optimization reference compressor: PDSim results.

7.3 Variable thickness optimization

The constant thickness compressor described in section 7.2.1 has been taken as starting point for a kriging optimization procedure. It has been decided to impose a series of geometrical constraints to obtain a final geometry similar enough to the reference. All the main parameters of the constant thickness scroll have been retained constant, except for the final angle of the wrap, Φ_e. According to the geometrical formulation described in 3.2, a single increment in the derivative of the curvature radius, h, and the starting angle of this increment, Φ_A, represent the other two variables of the kriging optimization.

The parameters and the constraints included in the optimization are summarized below:

- **Variables:**
  - Φ_e: from 18.52 rad to 29.52 rad
  - h: from 0.0 to 0.01
  - Φ_A: from 2π rad to 4π rad
- **Constraints:**
  - Displacement, maximum variation allowed: 2 % of the nominal value of 98 cm^3.
- **Constants:**
  - r_b, Φ_{os}, Φ_{is}, Φ_{i0}, *Width*, *Wrap thickness*, *Gap sizes*, *Discharge geometry*, *Fluid*, *Rotational speed*.

7.3.1 Kriging surrogate model

The kriging surrogate model has been constructed starting from the results of flow simulations performed with PDSim. The first *RSM* is created starting from a DOE based on an optimized *LHS* with 16 points and 3 variables. Eventually, a small percentage of failures due to unfeasible geometries can be ignored during the construction of the initial *RSM*. The overall efficiency ($\eta_v \bullet \eta_{forces}$) has been selected as the objective function of the optimization.

Further points have been added to the initial DOE according to a constrained *EI* method, which is summarized below:

- In parallel with the main surrogate model, secondary kriging *RSMs* are created to evaluate the constraints (in this case, a single *RSM* models the compressor displacement).
- Black-box optimization methods, such as *Genetic Algorithm (GA)* or *Particle Swarm Optimization (PSO)*, are employed to search the maximum *EI* in the design space. In the meantime, the displacement is evaluated using the secondary kriging model: if the constraint is not satisfied, the *EI* of that point is penalized with a negative constant.
- The point with the maximum constrained *EI* is simulated with PDSim and the kriging models (the main model and the secondary ones) are updated. This method ensures that only certain regions of the design space, the ones that satisfy the constraints, are further investigated with the addition of new points.

7.3.2 Optimization results

The operation of the addition of new points to the starting *LHS* is schematized in figures 7.2 and 7.3. The new points have been added according to the criterion of the maximum constrained expected improvement, which places the new simulations in the surroundings of the maximum value of efficiency that satisfies the constraints. For this reason, the region close to the maximum is refined better and better as long as new analyses are executed.

The improvement in the accuracy of the model in that part of the domain is testified by the evolution of the R^2 of model, as represented in figure 7.3. The optimization procedure has been stopped according to a minimum expected improvement criterion of 10^{-12}, considering that the starting points were characterized by values higher than 0.01.

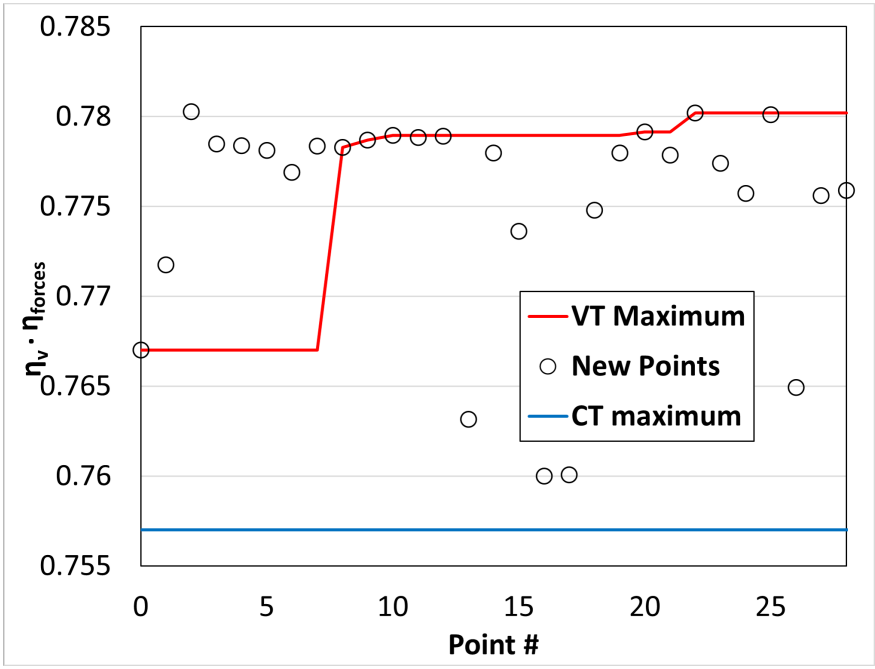

Figure 7.2: Optimization: additional points trend.

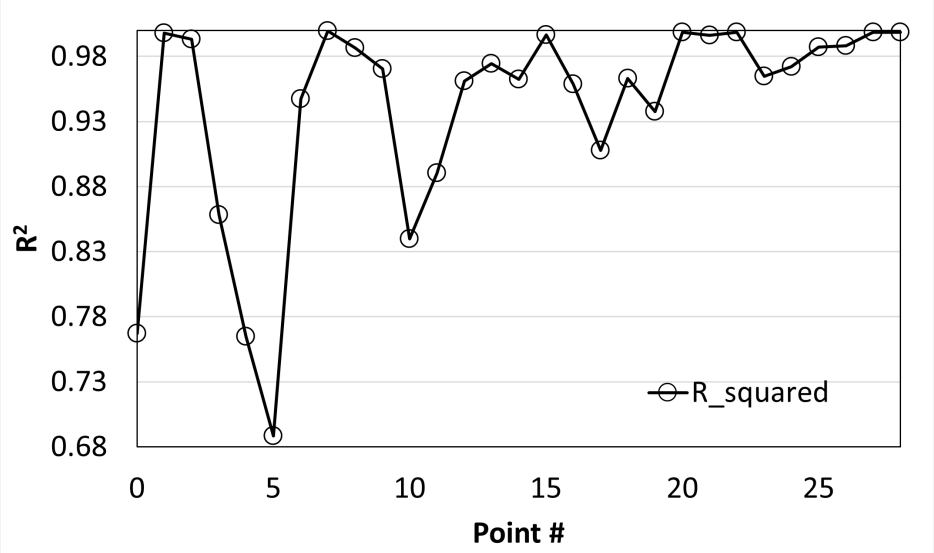

Figure 7.3: Optimization: additional points R^2.

The optimized geometry retains the design requirements proper of the starting constant thickness compressor: the displacement of 98 cm^3 is maintained almost constant, reaching a value of 99.7 cm^3. Similarly, the volume ratio is comparable to the original one, while the size of the shell is identical. According to figure 7.2, the pV efficiency of the new compressor reaches a value slightly higher than 78 %. The performance indicators of the compressor, represented in figure 7.4, are schematized in table 7.3.

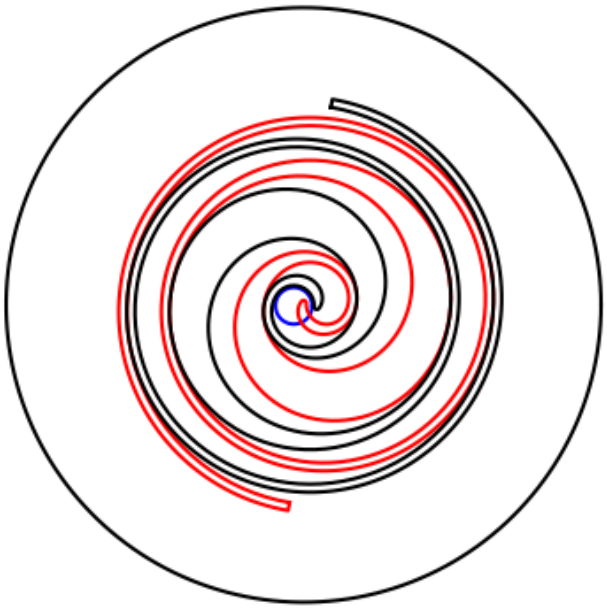

Figure 7.4: Optimization final geometry: variable thickness.

$\dot{m}$	η_v	η_{forces}	$\dot{W}_{forces}$
$0.042\,72\,kg\,s^{-1}$	0.914	0.854	4.320 kW

Table 7.3: Optimized compressor: PDSim results.

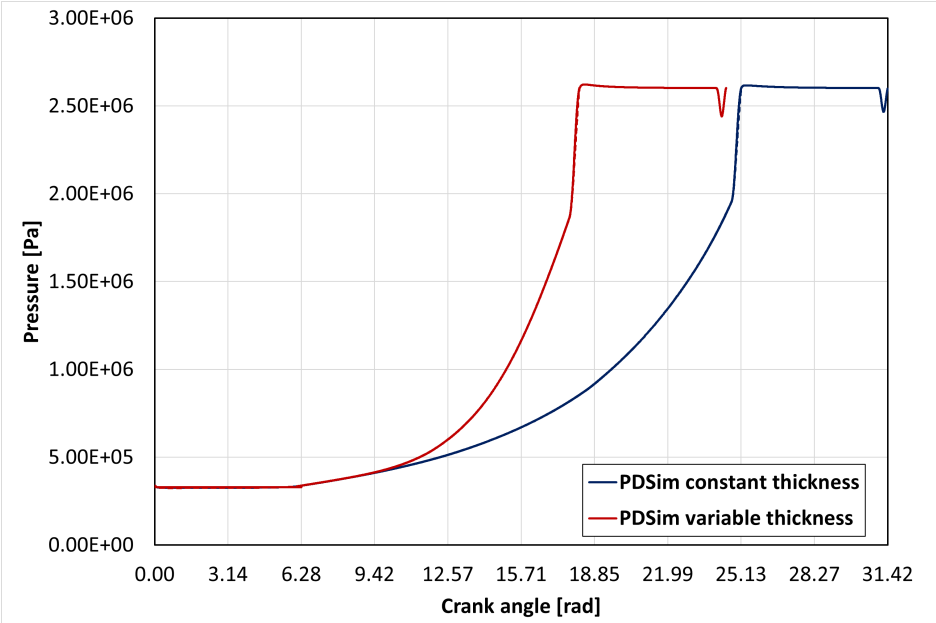

Figure 7.5: Constant thickness geometry vs optimized geometry: pressure-crank angle.

The pressure trends as functions of the crank angle are represented in figure 7.5 for both the reference and the optimized compressor. It is interesting to notice how the constant thickness requires one more revolution to perform the compression process. The beginning

of the variable thickness section, placed slightly after a crank angle of 8 rad, is highlighted by an evident change in the compression ratio. The design parameters of the optimized compressor are reported in table 7.4.

$\mathbf{r_b}$	$\boldsymbol{\phi_e}$	$\boldsymbol{\phi_{os}}$	$\boldsymbol{\phi_{is}}$	$\boldsymbol{\phi_{i0}}$	$\mathbf{h_{VT}}$
0.002 51 m	21.819 76 rad	0.9 rad	π+0.9 rad	0.0 rad	0.0095

Width	**Discharge**	**t**	**Flank gap**	**Axial gap**	$\boldsymbol{\phi_A}$
0.0256 m	2Arcs, $r_2 = 0.001$ m	0.003 m	15 µm	15 µm	8.04225

Table 7.4: Optimized compressor: geometrical parameters.

7.3.3 OpenFOAM validation

The optimization process has been validated using data with higher fidelity obtained with *OpenFOAM* simulation. In particular, the reference geometry and the optimized geometry have been simulated using a flank gap of 30 µm and a axial gap of 0 µm. The axial gap has been set to 0 because the implementation of the axial gap support has not been included in scrollFOAM yet. This kind of leakage represents a complex phenomenon to model, as already mentioned in section 2.3.1.

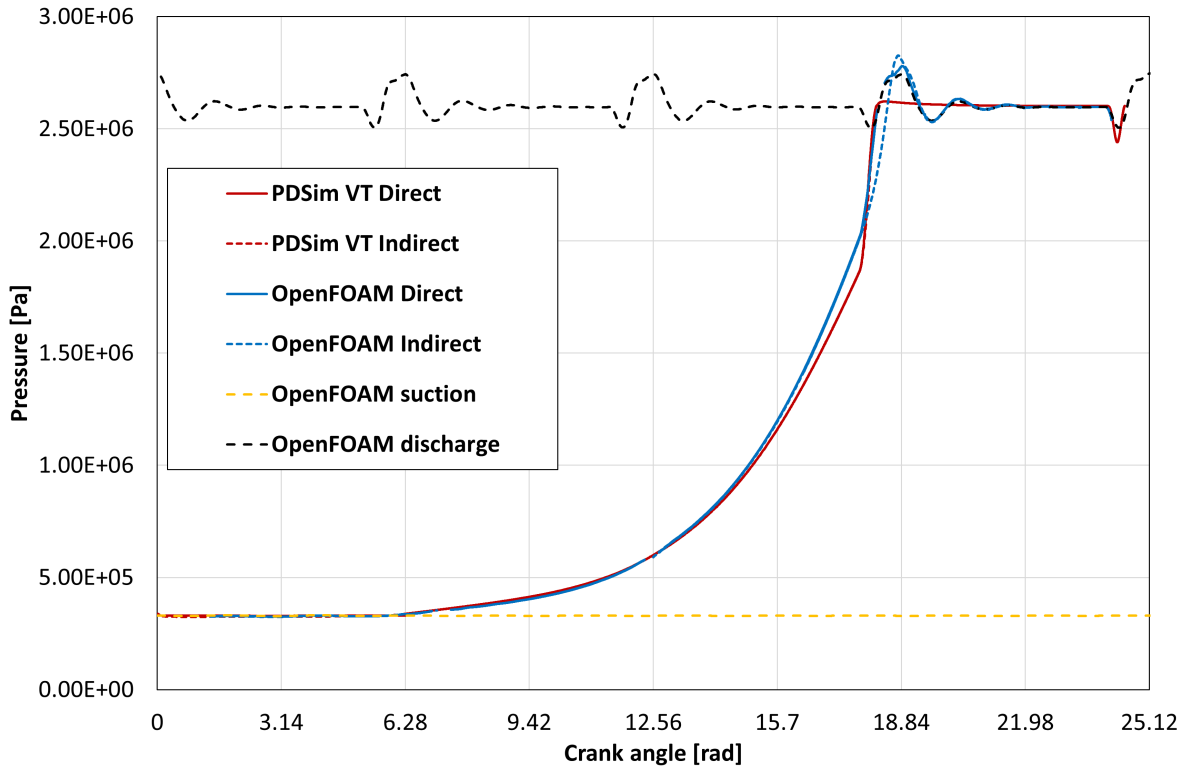

Figure 7.6: Optimized geometry: PDSim pressure trends compared with OpenFOAM pressure trends.

The pressure trends exhibit a very good agreement between the *OpenFOAM* and PDSim

results (figures 7.6 and 7.7). However, the *CFD* model shows a definitely smoother trend in the pressure behaviour in correspondence with the discharge angle. In both cases, the pressure is fastly increased after the discharge angle as a consequence of the reverse flow that happens because of the under-compression operating conditions. However, a re-compression is recorded in the discharge chamber according to the *OpenFOAM* data: this behaviour disappears completely in the 0-D model. The re-compression can be noticed because, in the *CFD* curves, the pressure of the discharge chamber reaches a value that is higher than the outlet pressure.

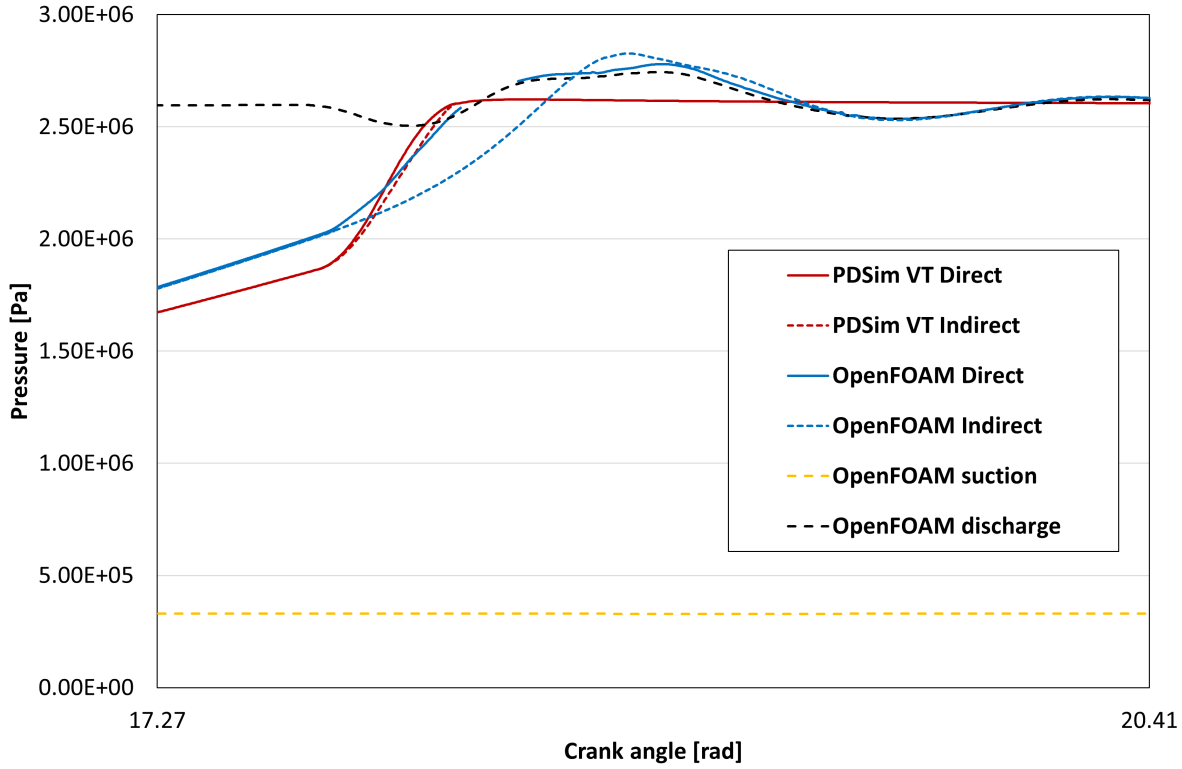

Figure 7.7: Optimized geometry: PDSim pressure trends compared with OpenFOAM pressure trends, discharge process.

Furthermore, as already observed in the validation test case of chapter 6, PDSim shows some issues in detecting the pressure difference between the direct and indirect chambers. A very slight difference between the two chambers can be spotted in the zoomed discharge trends of figure 7.7, but the equilibrium is reached again very quickly. On the contrary, the blue *OpenFOAM* curves require more than 0.5π rad to share the same pressure values again, following the discontinuity triggered by the beginning of the discharge process.

While the pressure trends show consistent accordance between the two simulation tools, some interesting information can be retrieved from the quantitative results reported in tables 7.5 and 7.6.

In general, the performance of both the compressors determined with PDSim are moderately superior if compared to the OpenFOAM ones. Furthermore, the results with the gap

	$\dot{m}$	η_v	η_{forces}	$\dot{W}_{forces}$
Reference	$0.0434\,kg\,s^{-1}$	0.944	0.872	4.159 kW
Optimized	$0.0440\,kg\,s^{-1}$	0.941	0.856	4.312 kW

Table 7.5: Reference compressor vs optimized compressor: PDSim results, no axial gap, flank gap = 30 µm.

	$\dot{m}$	η_v	η_{forces}	$\dot{W}_{forces}$
Reference	$0.0427\,kg\,s^{-1}$	0.929	0.851	4.259 kW
Optimized	$0.0430\,kg\,s^{-1}$	0.921	0.833	4.427 kW

Table 7.6: Reference compressor vs optimized compressor: OpenFOAM results, no axial gap, flank gap = 30 µm.

sizes employed for the *CFD* validation highlight an opposite trend with respect to the original optimization that included the radial leakages. In this case, the reference compressor has a slightly worst efficiency than the reference geometry, and this behaviour is confirmed by the *OpenFOAM* findings. As a consequence, it has been decided to use PDSim to conduce an analysis, presented in section 7.3.4, of the influence of the gap sizes on the performance of the reference and optimized compressors.

7.3.4 Gap effects

The analysis of the influence of the leakages on the performance of the two compressors has been realized by performing 9 PDSim simulations with different gap sizes. Three levels have been selected for the sizes of both the flank and axial gaps. The values adopted for the flank gap are 15, 30 and 60 µm, while the values for the axial gap are 0, 15 and 30 µm. The performance indicators analyzed are the volumetric efficiency and the pV efficiency, and the results are collected in tables 7.7 and 7.8 for the reference and optimized compressor respectively. It is interesting to observe that a axial gap size of 30 µm has already a completely disruptive effect on the performance of the compressor. Furthermore, the pV efficiency is more affected by a flank gap size variation, while an increase of the radial leakages is particularly detrimental for the volumetric efficiency.

η_v	**F 15**	**F 30**	**F 60**
R 0	0.958	0.944	0.910
R 15	0.917	0.901	0.853
R 30	0.671	0.629	0.487

η_{forces}	**F 15**	**F 30**	**F 60**
R 0	0.906	0.872	0.814
R 15	0.826	0.817	0.732
R 30	0.739	0.696	0.606

Table 7.7: Volumetric and pV efficiency at variable gap sizes, constant thickness geometry. (F = Flank leakage, R = Radial leakage), Gap sizes in µm.

η_v	F 15	F 30	F 60
R 0	0.957	0.941	0.899
R 15	0.914	0.893	0.835
R 30	0.685	0.640	0.510

η_{forces}	F 15	F 30	F 60
R 0	0.899	0.855	0.769
R 15	0.854	0.814	0.732
R 30	0.812	0.772	0.686

Table 7.8: Volumetric and pV efficiency at variable gap sizes, optimized geometry. (F = Flank leakage, R = Radial leakage), Gap sizes in µm.

In the author's opinion, the most efficient representation of the results is a contour of the percentage difference between the efficiencies of the optimized geometry (indicated as VT) and the efficiencies of the reference geometry (indicated as CT).

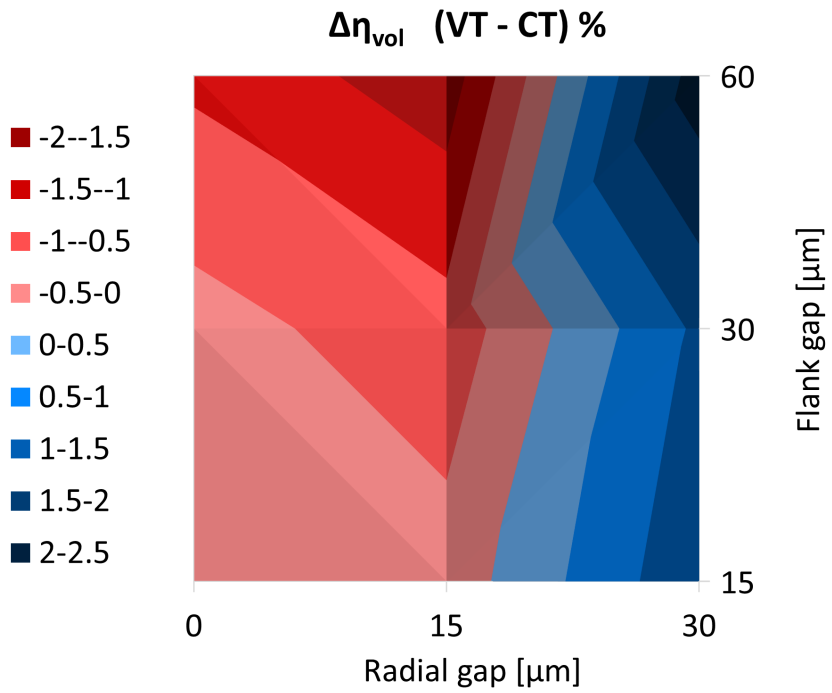

Figure 7.8: Gap size effects: volumetric efficiency. (VT = Variable Thickness, CT = Constant Thickness)

These contours, represented in figures 7.8 and 7.9, show that the constant thickness geometry appears to be more efficient when the size of the flank gap outweighs the size of the axial gap. Negative values of the percentage difference, shown in red gradations, indicate that the efficiency of the reference compressor is higher than the one of the optimized compressor in that particular region.

The test case selected for the optimization, characterized by a value of 15 µm for both the considered gaps, is placed in a region where the pV efficiency of the optimized compressors is clearly superior to the reference one. However, the validation case with no axial gap, placed at the south-west corner, shows an opposite behaviour as confirmed by the *CFD* simulations.

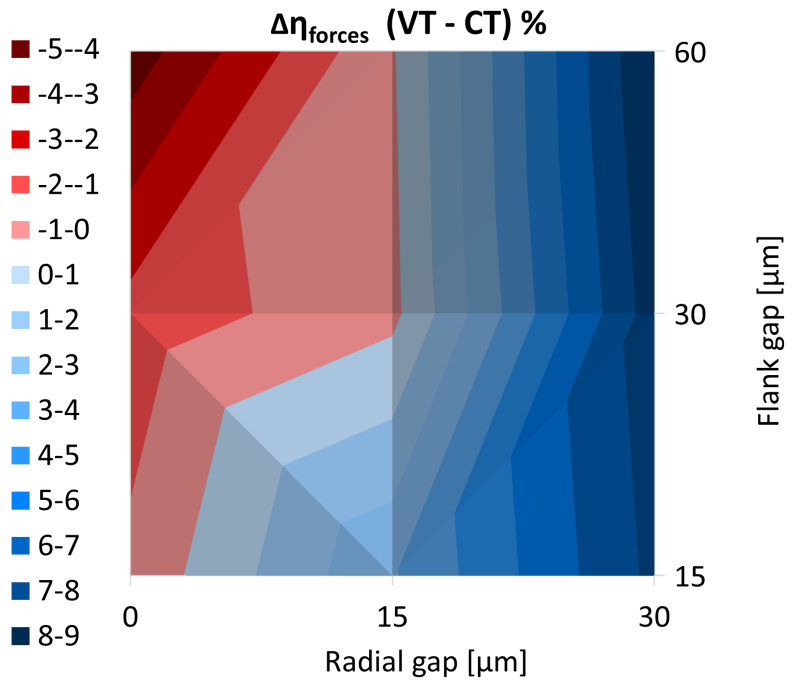

Figure 7.9: Gap size effects: pV efficiency. (VT = Variable Thickness, CT = Constant Thickness)

These results are consistent with the physics of the problem since variable thickness geometries are characterized by shorter but thicker spirals: the area of the flank gap is the same (since the width of the compressor is retained constant), but the length is reduced. For this reason, along the flank gap path, the high pressure region is closer to the low pressure region and the resistance to the flow is lower. On the contrary, axial gaps in variable thickness geometries are characterized by smaller areas (the spiral is shorter) and longer paths (the spiral is thicker): constant thickness geometries appear to be more prone to the radial leakage phenomenon.

7.4 Conclusions

This section contains a demonstration of the capabilities of the open-source tool-chain introduced in this thesis. Starting from the design parameters, both the simulation tools developed by the author have been employed to run an optimization process and to validate the obtained results.

Variable thickness geometries appear to be a very interesting candidate within the scope of reducing the manufacturing costs without a significant alteration of the performance. In addition to that, the analysis of the effects of the leakages run with PDSim has shown that, in presence of axial gaps, the introduction of variable thickness wraps should improve the efficiency of the machine.

The accordance between PDSim and *OpenFOAM* results has been further validated,

obtaining a good level of agreement for both the pressure trends and the quantitative evaluations of the performance.

The kriging optimization process is a promising tool that can be employed not only to include variable thickness sections to the wraps but also to perform a more general design procedure of a whole compressor/expander. The first response surface can be quickly built in parallel, while the infill procedure benefits from the introduction of the constraints, which allows investigating only the regions of interest considering the design requirements.

Chapter 8

Conclusions

8.1 Summary

- **Chapter 1** highlights the importance of scroll compressors and expanders in a wide range of energy-related fields of application. In particular, the attention is focused on the current modelling capabilities of the academic and industrial sectors. Although some highly proprietary simulation tools have been developed especially in the industrial environment, no or limited options are available in the open-source world.
  The introductory chapter presents a set of python and C++ libraries that have been developed to reduce this gap between open-source and commercial realities. Furthermore, variable thickness scroll geometries are firstly introduced, having been the object of an optimization procedure that fully exploits the simulation tool-chain presented in this thesis.

- **Chapter 2** firstly reviews the literature works focused on the geometry of scrolls. Afterwards, the attention is moved to experimental and numerical studies of the compressors, highlighting the high number of semi-empirical models presented by researchers. In the second part of the chapter, the more recent concept of employing scroll compressors as expanders in *ORCs* is presented, including once again experimental and numerical modelling.
  A special section is then dedicated to *CFD* simulations of scroll machines, showing that no open-source study has been conducted yet. Lastly, a complete literature review of variable thickness works has been included, describing the geometrical formulations published during the first two decades of the new millennium. Particular attention has been placed on the absence of rigorous comparison between constant thickness and variable thickness compressors.

- **Chapter 3** analyzes the mathematical foundations of the geometrical definition of

scroll machines. The formulation conceptualized by Bell [17] is reported in the first section of the chapter, followed by an extension of the study of Gravesen and Henrisken [72] performed by the author.

- **Chapter 4** reports the numerical tools used and developed by the author. PDSim, the recently published open-source software for quasi-static analyses of *PDMs*, is described in the first section. Particular attention is placed on the original development of a geometrical module for the analysis of variable thickness geometries.
  The remaining parts of the chapter are dedicated to the open-source *CFD* software *OpenFOAM*. The majority of the novelties presented in this thesis has been performed within this framework, which is the most used open-source software in the *CFD* world. In particular, two sets of libraries are presented: the first, CoolFOAM, extends the capabilities in the thermophysical properties calculation by coupling *OpenFOAM* and CoolProp. The second, scrollFOAM, supports the full *3-D* simulations of scroll compressors and expanders.

- **Chapter 5** presents the validation of the CoolFOAM library with experimental data related to incompressible and compressible applications. Furthermore, different *CFD* analyses of scroll expanders are included in the remaining parts of the chapter. In the first place, the influence of the accuracy of the evaluation of real gas properties has been investigated. In addition to that, the expander has been coupled with a plate heat exchanger to perform a multi-component *CFD* investigation of a portion of an *ORC*.

- **Chapter 6** validates the scrollFOAM framework with a set of pressure measurements conducted by the private company Danfoss Compressors in the scope of a collaboration between industry and academia. Three operating conditions have been tested to match the calculated pressure trends in the working chambers with the experimental reference. An additional cross-validation is included in the second part of the chapter, where the same compressor has been analyzed with PDSim and the results have been compared with both the *OpenFOAM* and experimental results.

- **Chapter 7** presents a kriging optimization of a variable thickness scroll compressor. This chapter is particularly important since it contains an assessment of the whole open-source tool-chain that is the main product of this thesis. Encouraging results show a cost reduction associated with the employment of variable thickness geometries, maintaining comparable levels of performance. The last section introduces a numerical study of the effect of gap sizes on the performance of the constant and variable thickness compressor.

8.2 Main achievements

- The scrollFOAM set of libraries for the simulation of scroll compressors in *OpenFOAM* has been successfully developed. The development has been integrated with a complete experimental validation using different operating conditions. In addition to that, the results have been compared with quasi-static simulations performed with PDSim, assessing the reliability of all the software employed.

- The importance of *CFD* simulations of positive displacement machines has been highlighted by the results obtained in the different analyses presented in this thesis. In particular, the comparison with low-order results showed how a deeper understanding of discharge and suction processes can be retrieved from *3-D* results.

- The *OpenFOAM* offer has been enlarged with the addition of the CoolFOAM wrapper for the evaluation of thermophysical properties. The library has been fully validated and applied to *CFD* simulations of scroll machines.

- The effects of off-design operation of the expander side of an ORC system has been the object of a complete analysis. The scroll expander, coupled with a recuperator, has also been simulated with different fluids to introduce the employment of scrollFOAM and CoolFOAM for the study of fluid replacements.

- A flexible formulation for the generation of variable thickness scroll geometries has been introduced by the author. Both the *OpenFOAM* and PDSim codes have been adapted to work with this kind of geometry.

- The whole open-source tool-chain presented in this thesis has been applied to an optimization process to design a variable thickness scroll compressor starting from a constant thickness reference. The results have indicated how variable thickness scroll could represent an important advancement in both the refrigeration and *WHR* worlds. In this specific case, the machining costs of the scroll have been consistently reduced by reducing the length of the spiral. The introduction of the variable thickness geometry has allowed maintaining the same level of performance and to equally satisfy the design constraints.

8.3 Future developments

- The set of scrollFOAM libraries could represent a starting point for the development of more advanced *CFD* models for scroll compressors, including two-phase flow simulations, fluid-structure interaction and conjugate heat transfer analyses. This thesis is

mostly focused on the fluid dynamics aspect of the scrolls, but other phenomena like oil-injection, two-phase compression and heat transfer have a significant influence on the performance of the machine.

- Currently, the radial leakages are not included in the meshing software that has been introduced in this work. Modelling these feature is not a trivial task, because tip sealings are often employed to avoid this kind of phenomenon. For this reason, advanced techniques should be developed to capture the real behaviour of the flow in the axial gap. This is particularly important if the results of chapter 7 are considered: variable thickness scrolls appear to be more resistant to radial leakages.

- The introduction of variable thickness scrolls is an interesting solution that should receive more attention from the academic world. Besides the costs reduction effect highlighted in this thesis, other optimization processes can be performed to increase the efficiency of compressors by increasing the volume ratio with comparable manufacturing costs. In the case of under-compression applications, where high volume ratios are needed, this should result in higher efficiencies of the compressors. Moreover, further analyses of the link between variable thickness features and the amount of leakage flow rate may be particularly interesting. Lastly, the role of variable thickness geometries in expanders applications should be investigated in the attempt of maximizing the power converted by *WHR* systems.

Bibliography

[1] HELYX. https://engys.com/products/helyx.

[2] OpenFOAM. http://www.openfoam.com.

[3] Wikki ltd. http://wikki.co.uk/.

[4] L. Abdelli, J. Degroote, and J. Vierendeels. Cfd analysis of an expansion process using different real gas models. *Master of Science in Electromechanical Engineering.*

[5] T. Allison. Janaf thermochemical tables, nist standard reference database 13, 1996.

[6] A. Ameli, A. Uusitalo, T. Turunen-Saaresti, and J. Backman. Numerical sensitivity analysis for supercritical co2 radial turbine performance and flow field. *Energy Procedia*, 129:1117–1124, 2017.

[7] F. Ayachi, E. Ksayer, P. Neveu, and A. Zoughaib. Experimental investigation and modeling of a hermetic scroll expander. *Applied Energy*, 181:256–267, 2016. cited By 30.

[8] N. Baltadjiev, C. Lettieri, and Z. Spakovszky. An investigation of real gas effects in supercritical co2 centrifugal compressors. *Journal of Turbomachinery*, 137(9), 2015.

[9] Y. Bartosiewicz, Z. Aidoun, and Y. Mercadier. Numerical assessment of ejector operation for refrigeration applications based on cfd. *Applied Thermal Engineering*, 26(5-6):604–612, 2006.

[10] N. Basha, S. Rane, and A. Kovacevic. Multiphase flow analysis in an oil-injected twin screw compressor. 04 2018.

[11] S. Behnel, R. Bradshaw, C. Citro, L. Dalcin, D. S. Seljebotn, and K. Smith. Cython: The best of both worlds. *Computing in Science Engineering*, 13(2):31–39, 2011.

[12] I. Bell, E. Groll, J. Braun, and W. Horton. Experimental testing of an oil-flooded hermetic scroll compressor. *International Journal of Refrigeration*, 36(7):1866–1873, 2013. cited By 21.

[13] I. Bell, E. Groll, J. Braun, W. Horton, and V. Lemort. Comprehensive analytic solutions for the geometry of symmetric constant-wall-thickness scroll machines. *International Journal of Refrigeration*, 45:223–242, 2014.

[14] I. Bell, E. Groll, J. Braun, and G. King. Update on scroll compressor chamber geometry. 01 2010.

[15] I. Bell, E. Groll, J. Braun, G. King, and W. Horton. Optimization of a scroll compressor for liquid flooding. *International Journal of Refrigeration*, 35(7):1901–1913, 2012.

[16] I. Bell, V. Lemort, E. Groll, J. Braun, G. King, and W. Horton. Liquid flooded compression and expansion in scroll machines - part ii: Experimental testing and model validation. *International Journal of Refrigeration*, 35(7):1890–1900, 2012.

[17] I. H. Bell. Theoretical and experimental analysis of liquid flooded compression in scroll compressors. 2011.

[18] I. H. Bell, E. A. Groll, J. E. Braun, and W. T. Horton. A computationally efficient hybrid leakage model for positive displacement compressors and expanders. *International Journal of Refrigeration*, 36(7):1965–1973, 2013. New Developments in Compressor Technology.

[19] I. H. Bell, J. Wronski, S. Quoilin, and V. Lemort. Pure and pseudo-pure fluid thermophysical property evaluation and the open-source thermophysical property library coolprop. *Industrial & Engineering Chemistry Research*, 53(6):2498–2508, 2014.

[20] I. H. Bell, J. Wronski, S. Quoilin, and V. Lemort. Pure and pseudo-pure fluid thermophysical property evaluation and the open-source thermophysical property library coolprop. *Industrial & engineering chemistry research*, 53(6):2498–2508, 2014.

[21] I. H. Bell, D. Ziviani, V. Lemort, C. R. Bradshaw, M. Mathison, W. T. Horton, J. E. Braun, and E. A. Groll. Pdsim: A general quasi-steady modeling approach for positive displacement compressors and expanders. *International Journal of Refrigeration*, 110:310 – 322, 2020.

[22] W. Bennett, N. Nikiforakis, and R. Klein. A moving boundary flux stabilization method for cartesian cut-cell grids using directional operator splitting. *Journal of Computational Physics*, 368:333–358, 2018.

[23] P. Betts and I. Bokhari. Experiments on turbulent natural convection in an enclosed tall cavity. *International Journal of Heat and Fluid Flow*, 21(6):675–683, 2000.

[24] M. Bianchi, L. Branchini, N. Casari, A. De Pascale, F. Melino, S. Ottaviano, M. Pinelli, P. Spina, and A. Suman. Experimental analysis of a micro-orc driven by piston expander for low-grade heat recovery. *Applied Thermal Engineering*, 148:1278–1291, 2019.

[25] P. Bin, V. Lemort, A. Legros, Z. Hongsheng, and G. Haifeng. Variable thickness scroll compressor performance analysis—part i: Geometric and thermodynamic modeling. *Proceedings of the Institution of Mechanical Engineers, Part E: Journal of Process Mechanical Engineering*, 231(4):633–640, 2017.

[26] P. Bin, V. Lemort, A. Legros, Z. Hongsheng, and G. Haifeng. Variable thickness scroll compressor performance analysis—part ii: Dynamic modeling and model validation. *Proceedings of the Institution of Mechanical Engineers, Part E: Journal of Process Mechanical Engineering*, 231(4):641–649, 2017.

[27] B. Blunier, G. Cirrincione, Y. Hervé, and A. Miraoui. A new analytical and dynamical model of a scroll compressor with experimental validation. *International Journal of Refrigeration*, 32(5):874–891, 2009.

[28] S. Bock, E. Bich, E. Vogel, A. S. Dickinson, and V. Vesovic. Calculation of the transport properties of carbon dioxide. III. volume viscosity, depolarized rayleigh scattering, and nuclear spin relaxation. *The Journal of Chemical Physics*, 121(9):4117–4122, 2004.

[29] R. Bracco, S. Clemente, D. Micheli, and M. Reini. Experimental tests and modelization of a domestic-scale orc (organic rankine cycle). *Energy*, 58:107–116, 2013.

[30] J. W. Bush and W. P. Beagle. Derivation of a general relation governing the conjugacy of scroll profiles. 1992.

[31] N. Casari, E. Fadiga, M. Pinelli, A. Suman, A. Kovacevic, S. Rane, and D. Ziviani. Numerical investigation of oil injection in a roots blower operated as expander. *IOP Conference Series: Materials Science and Engineering*, 604:012075, sep 2019.

[32] N. Casari, A. Suman, M. Morini, and M. Pinelli. Real gas expansion with dynamic mesh in common positive displacement machines. *Energy Procedia*, 129:248–255, 2017.

[33] N. Casari, A. Suman, D. Ziviani, M. Van Den Broek, M. De Paepe, and M. Pinelli. Computational models for the analysis of positive displacement machines: Real gas and dynamic mesh. *Energy Procedia*, 129:411–418, 2017.

[34] N. Casari, A. Suman, D. Ziviani, M. van den Broek, M. D. Paepe, and M. Pinelli. Computational models for the analysis of positive displacement machines: Real gas

and dynamic mesh. *Energy Procedia*, 129:411 – 418, 2017. 4th International Seminar on ORC Power SystemsSeptember 13-15th 2017POLITECNICO DI MILANOBOVISA CAMPUSMILANO, ITALY.

[35] J. R. Cash and A. H. Karp. A variable order runge-kutta method for initial value problems with rapidly varying right-hand sides. *ACM Trans. Math. Softw.*, 16(3):201–222, Sept. 1990.

[36] G. Cavazzini, F. Giacomel, G. Ardizzon, N. Casari, E. Fadiga, M. Pinelli, A. Suman, and F. Montomoli. Cfd-based optimization of scroll compressor design and uncertainty quantification of the performance under geometrical variations. *Energy*, 209:118382, 2020.

[37] CFX Berlin. Twinmesh.

[38] Y. Chen, N. P. Halm, J. E. Braun, and E. A. Groll. Mathematical modeling of scroll compressors — part ii: overall scroll compressor modeling. *International Journal of Refrigeration*, 25(6):751–764, 2002.

[39] Y. Chen, N. P. Halm, E. A. Groll, and J. E. Braun. Mathematical modeling of scroll compressors—part i: compression process modeling. *International Journal of Refrigeration*, 25(6):731 – 750, 2002.

[40] N.-K. Cho, Y. Youn, B. C. Lee, and M. K. Min. The characteristics of tip leakage in scroll compressors for air conditioners. 2000.

[41] N. Cressie. Geostatistics. *The American Statistician*, 43(4):197–202, 1989.

[42] L. Creux. Rotary engine, October 1905. US Patent no.801,182.

[43] C. Cuevas and J. Lebrun. Testing and modelling of a variable speed scroll compressor. *Applied Thermal Engineering*, 29(2-3):469–478, 2009. cited By 63.

[44] C. Cuevas, J. Lebrun, V. Lemort, and E. Winandy. Characterization of a scroll compressor under extended operating conditions. *Applied Thermal Engineering*, 30(6-7):605–615, 2010. cited By 36.

[45] V. D'Alessandro, L. Binci, S. Montelpare, and R. Ricci. On the development of openfoam solvers based on explicit and implicit high-order runge–kutta schemes for incompressible flows with heat transfer. *Computer Physics Communications*, 222:14–30, 2018.

[46] L. Dardenne, E. Fraccari, A. Maggioni, L. Molinaroli, L. Proserpio, and E. Winandy. Semi-empirical modelling of a variable speed scroll compressor with vapour injection. *International Journal of Refrigeration*, 54, 03 2015.

[47] B. Dechesne, F. Tello-Oquendo, S. Gendebien, and V. Lemort. Residential air-source heat pump with refrigerant injection and variable speed compressor: Experimental investigation and compressor modeling [pompe à chaleur aérothermique résidentielle avec injection de frigorigène et compresseur à vitesse variable: Étude expérimentale et modélisation du compresseur]. *International Journal of Refrigeration*, 108:79–90, 2019. cited By 5.

[48] I. Demirdžić and M. Perić. Space conservation law in finite volume calculations of fluid flow. 8(9):1037–1050.

[49] R. Dickes, O. Dumont, S. Declaye, S. Quoilin, I. Bell, and V. Lemort. Experimental investigation of an orc system for a micro-solar power plant. 07 2014.

[50] H. Ding and Y. Jiang. Cfd simulation of an oil flooded scroll compressor using vof approach. 2016.

[51] M. Diniz, E. Pereira, and C. Deschamps. A lumped-parameter thermal model for scroll compressors including the solution for the temperature distribution along the scroll wraps. *International Journal of Refrigeration*, 53:184–194, 2015. cited By 7.

[52] O. Dumont, A. Parthoens, R. Dickes, and V. Lemort. Experimental investigation and optimal performance assessment of four volumetric expanders (scroll, screw, piston and roots) tested in a small-scale organic rankine cycle system. *Energy*, 165, 06 2018.

[53] S. Emhardt, G. Tian, and J. Chew. A review of scroll expander geometries and their performance. *Applied Thermal Engineering*, 141:1020 – 1034, 2018.

[54] S. Emhardt, G. Tian, P. Song, J. Chew, and M. Wei. Cfd modelling of small scale orc scroll expanders using variable wall thicknesses. *Energy*, 199:117399, 2020.

[55] E. Fadiga, N. Casari, B. Angel, and A. Picavet. Flow computation inside a scroll compressor based on open-source code. *IOP Conference Series: Materials Science and Engineering*, 1180(1):012015, sep 2021.

[56] E. Fadiga, N. Casari, A. Suman, and M. Pinelli. Coolfoam: The coolprop wrapper for openfoam. *Computer Physics Communications*, page 107047, 2019.

[57] E. Fadiga, N. Casari, A. Suman, and M. Pinelli. Multi-component numerical investigation of a micro organic rankine cycle. In *Rankine 2020*, 2020.

[58] E. Fadiga, N. Casari, A. Suman, and M. Pinelli. Structured mesh generation and numerical analysis of a scroll expander in an open-source environment. *Energies*, 13(3):666, 2020.

[59] E. Fadiga, N. Casari, A. Suman, and M. Pinelli. Structured mesh generation and numerical analysis of a scroll expander in an open-source environment. *Energies*, 13(3):666, 2020.

[60] E. Fadiga, N. Casari, A. Suman, M. Pinelli, and F. Montomoli. Design considerations and numerical simulations of variable thickness scroll geometries. In *ECOS 2021*, 07 2021.

[61] G. R. Fanti, D. A. Romão, R. B. de Almeida, and P. E. B. de Mello. Influence of flank clearance on the performance of a scroll expander prototype. *Energy*, 193:116823, 2020.

[62] P. Farrell and J. Maddison. Conservative interpolation between volume meshes by local galerkin projection. *Computer Methods in Applied Mechanics and Engineering*, 200:89–100, 2011.

[63] J. H. Ferziger and M. Perić. *Computational Methods for Fluid Dynamics*. Springer, Berlin, 2nd edition, 1999.

[64] A. I. Forrester, A. Sóbester, and A. J. Keane. Multi-fidelity optimization via surrogate modelling. *Proceedings of the Royal Society A: Mathematical, Physical and Engineering Sciences*, 463(2088):3251–3269, 2007.

[65] A. I. J. Forrester, A. J. Keane, and N. W. Bressloff. Design and analysis of "noisy" computer experiments. *AIAA Journal*, 44(10):2331–2339, 2006.

[66] D. P. Gagne and J. Nieter. Simulating scroll compressors using a generalized conjugate surface approach. 1996.

[67] H. Gao, H. Ding, and Y. Jiang. 3d transient cfd simulation of scroll compressors with the tip seal. *IOP Conference Series: Materials Science and Engineering*, 90:012034, 08 2015.

[68] H. Gao, H. Ding, and Y. Jiang. 3d transient CFD simulation of scroll compressors with the tip seal. *IOP Conference Series: Materials Science and Engineering*, 90:012034, aug 2015.

[69] J. Gernert, A. Jäger, and R. Span. Calculation of phase equilibria for multi-component mixtures using highly accurate helmholtz energy equations of state. *Fluid Phase Equilibria*, 375:209 – 218, 2014.

[70] A. Goodwin, J. Sengers, C. Peters, R. S. of Chemistry (Great Britain), I. U. of Pure, A. C. Physical, B. C. Division, and I. A. of Chemical Thermodynamics. *Applied Thermodynamics of Fluids*. Royal Society of Chemistry, 2010.

[71] G. Gori, M. Zocca, G. Cammi, A. Spinelli, and A. Guardone. Experimental assessment of the open-source su2 cfd suite for orc applications. *Energy Procedia*, 129:256–263, 2017.

[72] J. Gravesen and C. Henriksen. The geometry of the scroll compressor. *Society for Industrial and Applied Mathematics*, 43:113–126, 03 2001.

[73] H.-M. Gutmann. A radial basis function method for global optimization. *JOURNAL OF GLOBAL OPTIMIZATION*, 19:2001, 1999.

[74] H. Guttinger. Displacement machine for compressible media, 1976. US Patent no.3,989,422.

[75] J. Hesse, A. Spille-Kohoff, R. Andres, and F. Hetze. Cfd simulation of scroll compressors with axial and radial clearances and thermal deformation. In *18. ISS*, pages 123–137, 2018.

[76] C. Hirsch. *Numerical Computation of Internal and External Flows*. Butterworth-Heinemann, Oxford, second edition, 2007.

[77] J. Honra, M. Berana, L. Danao, and M. Manuel. Cfd analysis of supersonic ejector in ejector refrigeration system for air conditioning application. *Lecture Notes in Engineering and Computer Science*, 2230:1019–1024, 2017.

[78] S. M. E. Hoque. Experimental investigation of an r134a based organic rankine cycle. 2011.

[79] M. L. Huber, A. Laesecke, and R. A. Perkins. Model for the viscosity and thermal conductivity of refrigerants, including a new correlation for the viscosity of r134a. *Industrial & Engineering Chemistry Research*, 42(13):3163–3178, 2003.

[80] M. L. Huber, R. A. Perkins, A. Laesecke, D. G. Friend, J. V. Sengers, M. J. Assael, I. N. Metaxa, E. Vogel, R. Mareš, and K. Miyagawa. New international formulation for the viscosity of h2o. *Journal of Physical and Chemical Reference Data*, 38(2):101–125, 2009.

[81] M.-J. Huron and J. Vidal. New mixing rules in simple equations of state for representing vapour-liquid equilibria of strongly non-ideal mixtures. *Fluid Phase Equilibria*, 3(4):255 – 271, 1979.

[82] N. Ishii, K. Bird, K. Sano, M. Oono, S. Iwamura, and T. Otokura. Refrigerant leakage flow evaluation for scroll compressors. 1996.

[83] N. James, J. Braun, E. Groll, and W. Horton. Semi-empirical modeling and analysis of oil flooded r410a scroll compressors with liquid injection for use in vapor compression systems. *International Journal of Refrigeration*, 66:50–63, 2016. cited By 15.

[84] D. Jones. A taxonomy of global optimization methods based on response surfaces. *J. of Global Optimization*, 21:345–383, 12 2001.

[85] M. Jradi, J. Li, H. Liu, and S. Riffat. Micro-scale ORC-based combined heat and power system using a novel scroll expander. *International Journal of Low-Carbon Technologies*, 9(2):91–99, 02 2014.

[86] F. Juretic. cfmesh user guide (v1.1).

[87] D. Kang, J. Kim, and C. Sohn. Effects of leakage flow model on the thermodynamic performance of a scroll compressor. 2002.

[88] S. H. Kang. Design and experimental study of orc (organic rankine cycle) and radial turbine using r245fa working fluid. *Energy*, 41(1):514 – 524, 2012. 23rd International Conference on Efficiency, Cost, Optimization, Simulation and Environmental Impact of Energy Systems, ECOS 2010.

[89] M. Khennich and N. Galanis. Optimal design of orc systems with a low-temperature heat source. *Entropy [electronic only]*, 2, 12 2012.

[90] H. J. Kim, J. M. Ahn, I. R. Park, and P. C. Rha. Scroll expander for power generation from a low-grade steam source. *Proceedings of the Institution of Mechanical Engineers, Part A: Journal of Power and Energy*, 221:705 – 711, 2007.

[91] S. Klein. Engineering Equation Solver; F-Chart Software, 2010.

[92] A. Kovacevic and S. Rane. Algebraic generation of single domain computational grid for twin screw machines part ii–validation. *Advances in Engineering Software*, 109:31–43, 2017.

[93] A. Kovacevic, N. Stosic, and I. Smith. *Screw Compressors: Three Dimensional Computational Fluid Dynamics and Solid Fluid Interaction*, volume 46. Springer Science & Business Media, 2007.

[94] O. Kunz and W. Wagner. The gerg-2008 wide-range equation of state for natural gases and other mixtures: An expansion of gerg-2004. *Journal of Chemical & Engineering Data*, 57(11):3032–3091, 2012.

[95] C. Kutlu, M. Erdinc, J. Li, Y. Su, G. Pei, G. Gao, and S. Riffat. Evaluate the validity of the empirical correlations of clearance and friction coefficients to improve a scroll expander semi-empirical model. *Energy*, 202, 2020. cited By 1.

[96] A. Landelle, N. Tauveron, P. Haberschill, R. Revellin, and S. Colasson. Organic rankine cycle design and performance comparison based on experimental database. *Applied Energy*, 204:1172–1187, 2017.

[97] D. Leal, R. Beltrán, P. Cardenas, S. Islas, and N. Velázquez. Design and analysis of the domestic micro-cogeneration potential for an orc system adapted to a solar domestic hot water system. *Entropy*, 21:911, 09 2019.

[98] B. C. Lee, T. Yanagisawa, M. Fukuta, and S. Choi. A study on the leakage characteristics of tip seal mechanism in the scroll compressor. 2002.

[99] Y.-R. Lee and W.-F. Wu. On the profile design of a scroll compressor. *International Journal of Refrigeration*, 18(5):308–317, 1995.

[100] E. Lemmon, R. Jacobsen, S. Penoncello, and D. Friend. Thermodynamic properties of air and mixtures of nitrogen, argon, and oxygen from 60 to 2000 k at pressures to 2000 mpa. *Journal of Physical and Chemical Reference Data*, 29(3):331–362, 2000.

[101] E. W. Lemmon, I. Bell, M. L. Huber, and M. O. McLinden. NIST Standard Reference Database 23: Reference Fluid Thermodynamic and Transport Properties-REFPROP, Version 10.0, National Institute of Standards and Technology, 2018.

[102] V. Lemort and A. Legros. 12 - positive displacement expanders for organic rankine cycle systems. In E. Macchi and M. Astolfi, editors, *Organic Rankine Cycle (ORC) Power Systems*, pages 361 – 396. Woodhead Publishing, 2017.

[103] V. Lemort, S. Quoilin, C. Cuevas, and J. Lebrun. Testing and modeling a scroll expander integrated into an organic rankine cycle. *Applied Thermal Engineering*, 29(14):3094 – 3102, 2009.

[104] V. Lemort, S. Quoilin, and J. J. Lebrun. Numerical simulation of a scroll expander for use in a rankine cycle. 2008.

[105] H. Li, Y. Chen, K. Wu, T. Wu, and X. Zhang. Experimental study on influencing factors of axial clearance for scroll compressor. *International Journal of Refrigeration*, 54:38–44, 2015. cited By 5.

[106] D. Lindsay and R. Radermacher. Theory and application of alternative scroll geometries. 2000.

[107] B. Luo. Theoretical study of r32 in an oil flooded compression cycle with a scroll machine [Étude théorique du r32 dans un cycle à compression noyée dans l'huile avec une machine à spirale]. *International Journal of Refrigeration*, 70:269–279, 2016. cited By 12.

[108] E. Macchi and M. Astolfi. *Organic Rankine Cycle (ORC) Power Systems: Technologies and Applications*. 09 2016.

[109] J. A. Mathias, J. R. Johnston, J. Cao, D. K. Priedeman, and R. N. Christensen. Experimental testing of gerotor and scroll expanders used in, and energetic and exergetic modeling of, an organic rankine cycle. *Journal of Energy Resources Technology*, 131(1):012201, 2009.

[110] L. C. Mendoza, J. Navarro-Esbrí, J. C. Bruno, V. Lemort, and A. Coronas. Characterization and modeling of a scroll expander with air and ammonia as working fluid. *Applied Thermal Engineering*, 70(1):630–640, 2014.

[111] F. R. Menter and T. Esch. Elements of industrial heat transfer prediction. *16th Brazilian Congress of Mechanical Engineering (COBEM)*, 2001.

[112] F. R. Menter, M. Kuntz, and R. Langtry. Ten years of industrial experience with the sst turbulence model. *Turbulence, heat and mass transfer*, 4(1):625–632, 2003.

[113] C. Montelius. Rotary compressor or motor, 1943. US Patent no.2,324,168.

[114] M. Morini, C. Pavan, M. Pinelli, E. Romito, and A. Suman. Analysis of a scroll machine for micro orc applications by means of a re/cfd methodology. *Applied Thermal Engineering*, 80:132–140, 2015.

[115] E. Morishita, M. Sugihara, T. Inaba, and T. Nakamura. Scroll compressor analytical model. 1984.

[116] E. Morishita, M. Sugihara, and T. Nakamura. Scroll compressor dynamics : 1st report, the model for the fixed radius crank. *Bulletin of JSME*, 29:476–482, 02 1986.

[117] F. Moukalled, L. Mangani, and M. Darwish. *The Finite Volume Method in Computational Fluid Dynamics: An Advanced Introduction with OpenFOAM® and Matlab®*, volume 113. 10 2015.

[118] T. Mukha, S. Rezaeiravesh, and M. Liefvendahl. A library for wall-modelled large-eddy simulation based on openfoam technology. *Computer Physics Communications*, 2019.

[119] A. A. Murthy, A. Subiantoro, S. Norris, and M. Fukuta. A review on expanders and their performance in vapour compression refrigeration systems. *International Journal of Refrigeration*, 106:427–446, 2019.

[120] J. Muye, G. Praveen Kumar, J. Bruno, R. Saravanan, and A. Coronas. Modelling of scroll expander for different working fluids for low capacity power generation. *Applied Thermal Engineering*, 159, 2019. cited By 2.

[121] E. Navarro, A. Redón, J. Gonzálvez-Macia, I. Martinez-Galvan, and J. Corberán. Characterization of a vapor injection scroll compressor as a function of low, intermediate and high pressures and temperature conditions. *International Journal of Refrigeration*, 36(7):1821–1829, 2013. cited By 43.

[122] V. Novaresio, M. García-Camprubí, S. Izquierdo, P. Asinari, and N. Fueyo. An open-source library for the numerical modeling of mass-transfer in solid oxide fuel cells. *Computer Physics Communications*, 183(1):125–146, 2012.

[123] Y. C. Park, Y. Kim, and H. Cho. Thermodynamic analysis on the performance of a variable speed scroll compressor with refrigerant injection. *International Journal of Refrigeration*, 25(8):1072–1082, 2002.

[124] E. L. Pereira and C. J. Deschamps. Numerical analysis and correlations for radial and tangential leakage of gas in scroll compressors. *International Journal of Refrigeration*, 110:239–247, 2020.

[125] B. Peris, J. Navarro-Esbrí, F. Molés, J. P. Martí, and A. Mota-Babiloni. Experimental characterization of an organic rankine cycle (orc) for micro-scale chp applications. *Applied Thermal Engineering*, 79:1 – 8, 2015.

[126] H.-D. Pham, T. Brandt, and D. H. Rowinski. Modeling a scroll compressor using a cartesian cut-cell based cfd methodology with automatic adaptive meshing. 2018.

[127] A. Picavet and B. Angel. Numerical simulation of the flow inside a scroll compressor equipped with intermediate discharge valves. In *Proc. 23th Int. Compressor Eng. Conference at Purdue*, 2016.

[128] A. Picavet and D. Genevois. Three-dimensional navier-stokes simulations of working of scroll compressors. In *Proc. 24th Int. Compressor Eng. Conference at Purdue*, 2018.

[129] A. Picavet and D. Genevois. *Three-Dimensional Navier-Stokes Simulations Of Working Of Scroll Compressors*, volume 1235, page 1–8. 2018.

[130] A. Picavet and P. Ginies. Experimental pressure-volume diagrams of scroll compressors. In *Proc. 22nd Int. Compressor Eng. Conference at Purdue*, 2014.

[131] J. Qiang and Z. Liu. Scroll profiles in scroll compressors: General criteria and error sensitivity. *International Journal of Refrigeration*, 36(7):1796–1808, 2013.

[132] S. Quoilin, M. V. D. Broek, S. Declaye, P. Dewallef, and V. Lemort. Techno-economic survey of organic rankine cycle (orc) systems. *Renewable and Sustainable Energy Reviews*, 22:168 – 186, 2013.

[133] J. Rak, S. Pietrowicz, Z. Gnutek, et al. The scroll compressor with internal cooling system–conception and cfd analysis. In *Proc. Int. Compress. Eng. Conf., Purdue, Paper*, volume 2364, 2014.

[134] S. Ramaraj, B. Yang, J. Braun, E. Groll, and W. Horton. Experimental analysis of oil flooded r410a scroll compressor. *International Journal of Refrigeration*, 46:185–195, 2014.

[135] S. Rane. *Grid generation and CFD analysis of variable geometry screw machines*. PhD thesis, City University London, 2015.

[136] S. Rane and A. Kovacevic. Algebraic generation of single domain computational grid for twin screw machines. part i. implementation. *Advances in Engineering software*, 107:38–50, 2017.

[137] S. Rane, A. Kovacevic, N. Stosic, and M. Kethidi. Grid deformation strategies for CFD analysis of screw compressors. 36(7):1883 – 1893.

[138] M. Richter, M. O. McLinden, and E. W. Lemmon. Thermodynamic properties of 2,3,3,3-tetrafluoroprop-1-ene (r1234yf): Vapor pressure and p-ρ-t measurements and an equation of state. *Journal of Chemical & Engineering Data*, 56(7):3254–3264, 2011.

[139] D. H. Rowinski, Y. Li, and K. Bansal. Investigations of automatic meshing in modeling a dry twin screw compressor. 2018.

[140] J. Sacks, W. J. Welch, T. J. Mitchell, and H. P. Wynn. Design and Analysis of Computer Experiments. *Statistical Science*, 4(4):409 – 423, 1989.

[141] T. SAITOH, N. YAMADA, and S. ichiro WAKASHIMA. Solar rankine cycle system using scroll expander. *Journal of Environment and Engineering*, 2(4):708–719, 2007.

[142] D. Seher, T. Lengenfelder, J. Gerhardt, N. Eisenmenger, M. Hackner, and I. Krinn. Waste heat recovery for commercial vehicles with a rankine process. In *21st Aachen*

Colloquium on Automobile and Engine Technology, Aachen, Germany, Oct, pages 7–9, 2012.

[143] J. Sengers. Transport properties of fluids near critical points. *International Journal of Thermophysics*, 6(3):203–232, 1985. cited By 155.

[144] B. R. Shaffer and E. A. Groll. Variable wall thickness scroll geometry modeling with use of a control volume approach. *International Journal of Refrigeration*, 36(7):1809 – 1820, 2013. New Developments in Compressor Technology.

[145] C. Shen, F. Sun, and X. Xia. Implementation of density-based solver for all speeds in the framework of openfoam. *Computer Physics Communications*, 185(10):2730–2741, 2014.

[146] Simerics. Pumplinx - simericsmp+.

[147] G. Singh, S. Sun, A. Kovacevic, Q. Li, and C. Bruecker. Transient flow analysis in a roots blower: Experimental and numerical investigations. *Mechanical Systems and Signal Processing*, 134:106305, 2019.

[148] S. Singh, A. Singh, and M. Dasgupta. Cfd modeling of a scroll work recovery expander for trans-critical co2 refrigeration system. *Energy Procedia*, 109:146–152, 2017. International Conference on Recent Advancement in Air Conditioning and Refrigeration, RAAR 2016, 10-12 November 2016, Bhubaneswar, India.

[149] P. Song, M. Wei, L. Shi, S. N. Danish, and C. Ma. A review of scroll expanders for organic rankine cycle systems. *Applied Thermal Engineering*, 75:54–64, 2015.

[150] P. Song, W. Zhuge, Y. Zhang, L. Zhang, and H. Duan. Unsteady leakage flow through axial clearance of an orc scroll expander. *Energy Procedia*, 129:355 – 362, 2017. 4th International Seminar on ORC Power SystemsSeptember 13-15th 2017POLITECNICO DI MILANOBOVISA CAMPUSMILANO, ITALY.

[151] R. Span. *Multiparameter Equations of State*. Springer Berlin Heidelberg, 2000.

[152] R. Span, E. Lemmon, R. Jacobsen, W. Wagner, and A. Yokozeki. A reference equation of state for the thermodynamic properties of nitrogen for temperatures from 63.151 to 1000 k and pressures to 2200 mpa. *Journal of Physical and Chemical Reference Data*, 29(6):1361–1401, 2000.

[153] R. Span, W. Wagner, E. Lemmon, and R. Jacobsen. Multiparameter equations of state - recent trends and future challenges. *Fluid Phase Equilibria*, 183-184:1–20, 2001.

[154] S. Spekreijse. Elliptic grid generation based on laplace equations and algebraic transformations. *Journal of Computational Physics*, 118(1):38 – 61, 1995.

[155] A. Spinelli, G. Cammi, S. Gallarini, M. Zocca, F. Cozzi, P. Gaetani, V. Dossena, and A. Guardone. Experimental evidence of non-ideal compressible effects in expanding flow of a high molecular complexity vapor. *Experiments in Fluids*, 59(8), 2018.

[156] K. Suefuji, M. Shiibayashi, and K. Tojo. Performance analysis of hermetic scroll compressors. *Trace*, 10:319–326, 1992.

[157] A. Suman, S. Randi, N. Casari, M. Pinelli, and L. Nespoli. Experimental and numerical characterization of an oil-free scroll expander. *Energy Procedia*, 129:403 – 410, 2017. 4th International Seminar on ORC Power SystemsSeptember 13-15th 2017POLITECNICO DI MILANOBOVISA CAMPUSMILANO, ITALY.

[158] S. Sun, X. Wang, P. Guo, and Z. Song. Investigation on the modifications of the suction flow passage in a scroll refrigeration compressor. *Applied Thermal Engineering*, 170, 2020. cited By 4.

[159] S. Sun, K. Wu, P. Guo, and J. Yan. Analysis of the three-dimensional transient flow in a scroll refrigeration compressor. *Applied Thermal Engineering*, 127:1086 – 1094, 2017.

[160] J. P. Sung, J. H. Boo, and E. G. Jung. Transient thermodynamic modeling of a scroll compressor using r22 refrigerant. *Energies*, 13(15), 2020.

[161] D. Sánchez, R. Cabello, R. Llopis, I. Arauzo, J. Catalán-Gil, and E. Torrella. *Energy performance evaluation of R1234yf, R1234ze(E), R600a, R290 and R152a as low-GWP R134a alternatives. International Journal of Refrigeration*, 74:269 – 282, 2017.

[162] F. Tello-Oquendo, E. Navarro-Peris, and J. Gonzálvez-Maciá. Comparison of the performance of a vapor-injection scroll compressor and a two-stage scroll compressor working with high pressure ratios. *Applied Thermal Engineering*, 160, 2019. cited By 10.

[163] F. M. Tello-Oquendo, E. Navarro-Peris, F. Barceló-Ruescas, and J. Gonzálvez-Maciá. Semi-empirical model of scroll compressors and its extension to describe vapor-injection compressors. model description and experimental validation. *International Journal of Refrigeration*, 106:308–326, 2019.

[164] C. Thomas, M. Margraf, C. Stoeckel, K. Klotsche, and U. Hesse. Implementation of scroll compressors into the cordier diagram. 604:012079, sep 2019.

[165] M. Thorade and A. Saadat. Partial derivatives of thermodynamic state properties for dynamic simulation. *Environmental Earth Sciences*, 70(8):3497–3503, 2013.

[166] R. Tillner-Roth and H. D. Baehr. An international standard formulation for the thermodynamic properties of 1,1,1,2-tetrafluoroethane (hfc-134a) for temperatures from 170 k to 455 k and pressures up to 70 mpa. *Journal of Physical and Chemical Reference Data*, 23(5):657–729, 1994.

[167] J. Valderrama. The state of the cubic equations of state. *Industrial and Engineering Chemistry Research*, 42(8):1603–1618, 2003.

[168] J. O. Valderrama. The state of the cubic equations of state. *Industrial & Engineering Chemistry Research*, 42(8):1603–1618, 2003-04.

[169] W. Wagner. Fluidcal. `http://www.thermo.rub.de/de/prof-w-wagner/software/fluidcal.html`.

[170] B. Wang, X. Li, and W. Shi. A general geometrical model of scroll compressors based on discretional initial angles of involute. *International Journal of Refrigeration*, 28(6):958–966, 2005.

[171] H. Wang, R. B. Peterson, and T. Herron. Experimental performance of a compliant scroll expander for an organic rankine cycle. *Proceedings of the Institution of Mechanical Engineers, Part A: Journal of Power and Energy*, 223(7):863–872, 2009.

[172] J. Wang, Q. Liu, C. Cao, Z. Wang, Q. Li, and Y. Qu. Design methodology and geometric modeling of complete meshing profiles for scroll compressors [méthodologie de conception et modélisation géométrique des profils de maillage complets pour les compresseurs à spirale]. *International Journal of Refrigeration*, 91:199–210, 2018.

[173] J. Wang, Y. Song, Q. Li, and D. Zhang. Novel structured dynamic mesh generation for cfd analysis of scroll compressors. *Proceedings of the Institution of Mechanical Engineers, Part A: Journal of Power and Energy*, 229(8):1007–1018, 2015.

[174] H. G. Weller, G. Tabor, H. Jasak, and C. Fureby. A tensorial approach to computational continuum mechanics using object-oriented techniques. *Computers in Physics*, 12(6):620, 1998.

[175] E. Winandy and J. Lebrun. Scroll compressors using gas and liquid injection: Experimental analysis and modelling. *International Journal of Refrigeration*, 25(8):1143–1156, 2002. cited By 119.

[176] E. Winandy, C. Saavedra O, and J. Lebrun. Experimental analysis and simplified modelling of a hermetic scroll refrigeration compressor. *Applied Thermal Engineering*, 22(2):107–120, 2002. cited By 109.

[177] S. Xu, X. Fan, and G. Ma. Experimental investigation on heating performance of gas-injected scroll compressor using r32, r1234yf and their 20wt%/80wt% mixture under low ambient temperature. *International Journal of Refrigeration*, 75:286–292, 2017. cited By 23.

[178] T. Yanagisawa, M. D. Cheng, M. Fukuta, and T. Shimizu. Optimum operating pressure ratio for scroll compressor. *Transactions of the Japan Society of Mechanical Engineers. B*, 55:1318–1323, 1989.

[179] Q. Yang, L. Li, Y. Zhao, and P. Shu. Experimental measurement of axial clearance in scroll compressor using eddy current displacement sensor. *Proceedings of the Institution of Mechanical Engineers, Part C: Journal of Mechanical Engineering Science*, 222(7):1315–1320, 2008.

[180] N. Young and J. McCullough. Scroll type positive fluid displacement apparatus, 1975. US Patent no.3,884,599.

[181] X. H. Yuan, Z. Chen, and Z. Fan. Calculating model and experimental investigation of gas leakage. 1992.

[182] A. Zendehboudi, X. Li, and B. Wang. Utilization of ann and anfis models to predict variable speed scroll compressor with vapor injection [utilisation des modèles ann et anfis pour prédire un compresseur à spirale à vitesse variable avec injection de vapeur]. *International Journal of Refrigeration*, 74:473–485, 2017. cited By 25.

[183] X. Zhang, C. Qin, Y. Xu, W. Li, X. Zhou, R. Li, Y. Huang, and H. Chen. Integration of small-scale compressed air energy storage with wind generation for flexible household power supply. *Journal of Energy Storage*, 37:102430, 2021.

[184] N. Zhou, X. Wang, Z. Chen, and Z. Wang. Experimental study on organic rankine cycle for waste heat recovery from low-temperature flue gas. *Energy*, 55:216–225, 2013.

[185] D. Ziviani, I. H. Bell, X. Zhang, V. Lemort, M. D. Paepe, J. E. Braun, and E. A. Groll. Pdsim: Demonstrating the capabilities of an open-source simulation framework for positive displacement compressors and expanders. *International Journal of Refrigeration*, 110:323 – 339, 2020.

[186] D. Ziviani, R. Dickes, V. Lemort, J. Braun, and E. Groll. *Effects of the Working Fluid Charge in Organic Rankine Cycle Power Systems: Numerical and Experimental Analyses*. 11 2018.

[187] D. Ziviani, N. James, F. Accorsi, J. Braun, and E. Groll. Experimental and numerical analyses of a 5 kwe oil-free open-drive scroll expander for small-scale organic rankine cycle (orc) applications. *Applied Energy*, 230:1140–1156, 2018. cited By 33.

Appendix A

OpenFOAM basic structure

A.1 Libraries and applications

The core of the code is a large set of C++ libraries containing the main features of every *CFD* code: in addition to algorithms for the solution of differential equations, tensor operations and other basic functionalities, dynamic meshing and several physical models have been implemented. This set of libraries is the point of departure for the development of applications, broken down into two categories: solvers and utilities.

A.1.1 Solvers

The solvers carry out the actual calculations for a wide range of different applications: starting from the simple potential flow solver (**potentialFoam**), it is possible to use dynamic mesh (**icoDyMFoam**) solvers and compressible transient solvers, such as **rhoPimpleFoam**. More complex applications are conjugate heat transfer solvers, like **chtMultiRegionFoam**, and supersonic turbulent (**sonicTurbFoam**) solvers. Less common possibilities are a solver for solid stress analysis, **solidDisplacementFoam**, and even one for finance (**financialFoam**).

A.1.2 Utilities

All the other operations are performed by the utilities, which can be divided in a list of macro-categories:

- *Meshing*: it is possible to generate a structured cartesian grid with the **blockMesh** utility, and for more complex geometries **snappyHexMesh** creates an unstructured hex-dominant mesh starting from a *STereo Lithography interface format (STL)* file. The result of the meshing process can be evaluated with **checkMesh**, analyzing parameters like skewness and orthogonal quality. It is also possible to map volume fields

from one mesh to another with **mapFields**, in order to introduce some changes in a case without starting from scratch.

- *Initial conditions and boundary conditions*: boundary and initial conditions are often set manually, changing specific entries directly from the text files that define an *OpenFOAM* case. Sometimes, when several entries must be changed at the same time, the **changeDictionary** utility can be used to perform the operation more quickly.

- *Post-processing*: there are many post-processing utilities, useful to extract additional information from the results. As an example, **MachNo** allows extracting the Mach number fields after the calculation phase. Other post-processing utilities allow to perform averages on specific patches or boundaries. It is also possible to record the values of variables of interest in specific points of the domain by placing user-defined probes.

A.1.3 Third Party

In addition to the standard *OpenFOAM* capabilities, a set of additional packages (third party packages) is present. **Paraview** is fundamental for graphical post-processing, which would be very challenging to perform without an interface. **OpenMPI** allows running *OpenFOAM* in parallel on distributed processors, with many utilities associated with this functionality (**decomposePar**, **reconstructPar**, **mpirun** etc.).

A.2 OpenFOAM case structure

Every *OpenFOAM* case is based on a common structure, which can be slightly modified for specific solvers or applications. In this software, the basic files for the *Input/Output (I/O)* management are dictionaries. A dictionary contains data entries recalled by the *I/O* by using keywords, following the general format below:

<keyword> <dataEntry1> ... <dataEntryN>;

It is necessary to create a main directory whose name is representative of the case. This directory contains three fundamental sub-directories, (**system**, **constant** and at least **one time directory**) which can include dictionaries or other directories (figure A.1).

In addition to that, every dictionary has the same header, typical of *OpenFOAM* files:

```
/*--------------------------------*- C++ -*----------------------------------*\
| =========                 |                                                 |
| \\      /  F ield         | OpenFOAM: The Open Source CFD Toolbox           |
|  \\    /   O peration     | Version:  v1606+                                |
|   \\  /    A nd           | Web:      www.OpenFOAM.com                      |
|    \\/     M anipulation  |                                                 |
\*---------------------------------------------------------------------------*/
FoamFile
{
```

```
 version     2.0;
 format      ascii;
 class       dictionary;
 location    "constant";
 object      thermoPhysicalProperties;
}
// * * * * * * * * * * * * * * * * * * * * * * * * * * * * * * * * * * * *//
```

Figure A.1: OpenFOAM case directory tree.

A.2.1 System

In the system directory, there are at least three essential dictionaries for the execution of any solver: *controlDict*, *fvSchemes* and *fvSolution*. It is also possible to find parallel-run related files (e.g. *decomposeParDict*) and meshing dictionaries, such as *blockMeshDict* and *snappyHexMeshDict*.

- **controlDict**: this dictionary contains parameters associated with the run control. It is possible to control the start/end time, the temporal discretization, the modality of solutions storage and other parameters. A small section of this file is reported below:

```
application     rhoSimpleFoam;

startFrom       latestTime;

startTime       0;

stopAt          endTime;

endTime         111;

...
```

- **fvSolution**: includes the entries for the selection of solvers, algorithms and tolerances for the solution of the different equations. An example, for the pressure equation, could be:

```
    solvers
{
        "p.*"
    {
        solver                  GAMG;
        smoother                symGaussSeidel;
        nCellsInCoarestLevel    10;
        agglomerator            faceAreaPair;
        preconditioner          DIC;
        tolerance               0;
        relTol                  1e-7;
        maxIter                 150;
    }
    ...
}
```

"The pressure is solved with the Geometric Agglomerated Algebraic Multigrid solver, with the symmetric Gauss Siedel smoother. The approximate size of the mesh at the coarsest level is 10 cells and the agglomeration of cells is performed with the faceAreaPair method. Furthermore, the Simplified Diagonal-based Incomplete Cholesky preconditioner is used. A zero tolerance for the final residual and a relative tolerance between initial and final residual of 1e-7 have been selected. Finally, the maximum number of iterations is set to 150."

```
    PIMPLE
{
    nOuterCorrectors            1;
    nCorrectors                 2;
    nNonOrthogonalCorrectors    0;
    consistent                  yes;

    relaxationFactors
    {
        fields
        {
            p       1;
        }
        ...
}
```

In a similar fashion, the PIMPLE controls section include correctors and relaxation factors for all the variables.

- **fvSchemes**: contains the settings for the numerical schemes for the operators appearing in differential equations. Laplacian terms, time schemes and divergence can be treated with several types of schemes. As an example, in the following dictionary the Euler scheme is used for temporal discretization. For the velocity gradient a Gauss linear scheme has been chosen, and so on:

```
ddtSchemes
{
    default         Euler;
}

gradSchemes
{
    default         Gauss linear;
```

```
        grad(U)         Gauss  linear 1;
        grad(h)         Gauss  linear 1;
        ...
    }

    ...

    interpolationSchemes
    {
        default         linear;
    }


    // ************************************************************* //
```

A.2.2 Constant

In the constant directory there are dictionaries related to the physical properties: *thermoPhysicalProperties*, *turbulenceProperties*, *(*gravitational acceleration), etc. In addition to these, there is an important sub-directory, named **polyMesh**, which includes all the files that define the mesh. As an example, the boundary files included in the **polyMesh** directory contains the definition of all the boundaries of the domain. A boundary can be a wall, a patch, a symmetry plane etc. A partial sample of this dictionary is reported below:

```
6
(
    Inlet
    {
        type            patch;
        nFaces          30;
        startFace       18740;
    }
    Outlet
    {
        type            patch;
        nFaces          20;
        startFace       18770;
    }
    Walls
    {
        type            wall;
        nFaces          690;
        startFace       38010;
    }
)
```

The *thermophysicalProperties* dictionary comprehends the entries for the *I/O* related to the equation of state and to the thermodynamic and transport properties. This dictionary is of particular importance in this thesis because it contains the CoolFOAM wrapper, a new method to determine these properties.

```
thermoType
{
    type            hePsiThermo;
    mixture         pureMixture;
    transport       polynomial;
    thermo          hPolynomial;
    equationOfState PengRobinsonGas;
    specie          specie;
    energy          sensibleEnthalpy;
}

mixture
{
    equationOfState
    {
        Tc      374.21;
```

```
        Pc      4059280;
        Vc      0.00194;
        omega   0.32684;
    }

    ...

}
```

In the beginning, all the models are declared, then specific settings are added to characterize them. In this case, the Peng-Robinson equation needs the critical point values of thermodynamic variables and the acentric factor of the gas.

A.2.3 Time directories

The variable fileds, stored in dictionaries updated by the solvers, are stored in the time directories: these directories are named with the number of the associated time-step. Usually, the first is related to the time-step "**0**", and contains the initialization for the internal field and for the boundary conditions. For example, the velocity field could be:

```
// * * * * * * * * * * * * * * * * * * * * * * * * * * * * * * * * * * * * * * * * * //

dimensions      [0 1 -1 0 0 0 0];

internalField   uniform (10 0 0);

boundaryField
{
    Inlet
    {
        type            flowRateInletVelocity;
        massFlowRate    constant    0.1;
        rhoInlet        1;  //estimate for initial rho
    }
    Outlet
    {
        type            pressureInletOutletVelocity;
        value           uniform (10 0 0);
        inletValue      uniform (0 0 0);
    }
    Walls
    {
        type            noSlip;
    }
}
```

In this case, the flow rate is fixed at the inlet, with an outlet condition that prevents the outflow to flow back into the domain. At the walls, the velocity relative to the boundary is set to zero.

When everything is set properly, the solver can be executed simply from the terminal, making sure that the current working directory is the case directory:

```
rhoPimpleFoam > log
```

The solver will store the solutions, represented by the upgraded variable fields, in new time directories. Of course, the user has to define how often this procedure has to be performed.

Appendix B

Integration of variable thickness scroll curves.

$$\mathbf{x_0}(\phi) = (R_b, 0.0) + \rho_0(\sin\phi, -\cos\phi) + \mathbf{x_0^{Rb}}(\phi) + \mathbf{x_0^{I}}(\phi_{Ai}) + \mathbf{x_0^{II}}(\phi_{Ai}, \phi) \tag{B.1}$$

$$\mathbf{x_0^{Rb}}(\phi) = R_b(\phi\sin\phi + \cos\phi - 1, -\phi\cos\phi + \sin\phi) \tag{B.2}$$

$$\mathbf{x_0^{I}}(\phi_{Ai}) = \mathbf{x_0^{IA}}(\phi_{Ai}) + \mathbf{x_0^{IB}}(\phi_{Ai}) \tag{B.3}$$

$$\mathbf{x_0^{IA}}(\phi_{Ai}) = sum_i(i)(\sin\phi_{Ai} - \sin\phi_{Ai-1}, -\cos\phi_{Ai} + \cos\phi_{Ai-1}) \tag{B.4}$$

$$\mathbf{x_0^{IB}}(\phi_{Ai}) = \frac{h_i}{\pi}(-\phi_{Ai-1}\sin\phi_{Ai} + \phi_{Ai}\sin\phi_{Ai} + \cos\phi_{Ai} - \cos\phi_{Ai-1}, \\ \phi_{Ai-1}\cos\phi_{Ai} - \phi_{Ai}\cos\phi_{Ai} + \sin\phi_{Ai} - \sin\phi_{Ai-1}) \tag{B.5}$$

$$sum_i(i) = \sum_{j=1}^{i} \frac{h_{j-1}}{\pi}(\phi_{Aj} - \phi_{Aj-1}), sum_i(0) = 0.0 \tag{B.6}$$

$$\mathbf{x_0^{II}}(\phi_{Ai}, \phi) = \mathbf{x_0^{IIA}}(\phi_{Ai}, \phi) + \mathbf{x_0^{IIB}}(\phi_{Ai}, \phi) \tag{B.7}$$

$$\mathbf{x_0^{IIA}}(\phi_{Ai}, \phi) = sum_i(i)(\sin\phi - \sin\phi_{Ai}, -\cos\phi + \cos\phi_{Ai}) \tag{B.8}$$

$$\mathbf{x_0^{IIB}}(\phi_{Ai},\phi) = \frac{h_i}{\pi}(-\phi_{Ai}\sin\phi + \phi\sin\phi + \cos\phi - \cos\phi_{Ai},$$
$$\phi_{Ai}\cos\phi - \phi\cos\phi + \sin\phi - \sin\phi_{Ai}) \quad \text{(B.9)}$$